



---

UNIVERSITÀ DEGLI STUDI DI GENOVA  
FACOLTÀ DI SCIENZE MATEMATICHE, FISICHE E NATURALI  
SCUOLA DI DOTTORATO IN SCIENZE E TECNOLOGIE  
PER L'INFORMAZIONE E LA CONOSCENZA  
XXI CICLO, A.A. 2006 - 2009



---

A THESIS SUBMITTED FOR THE DEGREE OF  
*Dottore di Ricerca in*  
*Fisica Nucleare e Subnucleare*

SEARCH FOR DOUBLE BETA DECAY TO EXCITED  
STATES WITH CUORICINO AND DATA  
ACQUISITION SYSTEM FOR CUORE

AUTHOR  
***Sergio Di Domizio***  
*Università e sezione INFN di Genova*

SCHOOL COORDINATOR  
***Prof. Pierantonio Zanghì***  
*Università e sezione INFN di Genova*

ADVISOR  
***Prof. Marco Pallavicini***  
*Università e sezione INFN di Genova*

EXTERNAL ADVISOR  
***Prof. Fernando Ferroni***  
*Università La Sapienza e sezione INFN di Roma*

AREA 02 - SCIENZE FISICHE  
SETTORE SCIENTIFICO-DISCIPLINARE: FIS/04



# Contents

<b>Introduction</b>	<b>2</b>
<b>1 Neutrino physics and double beta decay</b>	<b>3</b>
1.1 Introduction . . . . .	3
1.2 Neutrino Oscillations . . . . .	4
1.3 Neutrino Masses . . . . .	9
1.4 Open Questions Concerning Neutrino Masses . . . . .	13
1.4.1 Neutrino mass hierarchy . . . . .	13
1.4.2 Absolute measurement of neutrino mass . . . . .	14
1.4.3 Dirac and Majorana neutrinos . . . . .	15
1.5 Double beta decay . . . . .	15
1.5.1 Nuclear matrix elements . . . . .	18
<b>2 Experimental search for double beta decay</b>	<b>21</b>
2.1 Introduction . . . . .	21
2.2 Fundamentals of $0\nu\beta\beta$ experiments . . . . .	21
2.3 Double beta decay experiments . . . . .	24
2.3.1 Past and present experiments . . . . .	25
2.3.2 Future experiments . . . . .	27
2.4 The bolometric technique . . . . .	29
2.4.1 Working Principles . . . . .	30
2.4.2 Energy Absorber . . . . .	31
2.4.2.1 Thermalization of deposited energy . . . . .	32
2.4.3 Sensor . . . . .	33
2.4.4 Detector operation . . . . .	35
<b>3 The CUORICINO experiment</b>	<b>39</b>
3.1 Introduction . . . . .	39
3.2 Experimental setup . . . . .	39
3.3 Energy absorber: the choice of $\text{TeO}_2$ . . . . .	42
3.4 The thermal sensor . . . . .	43
3.5 The single module . . . . .	45

3.6	Signal readout . . . . .	46
3.7	First level analysis . . . . .	48
3.8	CUORICINO background and $0\nu\beta\beta$ results . . . . .	49
3.8.1	Data taking and detector performance . . . . .	50
3.8.2	Background analysis . . . . .	51
3.8.3	CUORICINO $0\nu\beta\beta$ results . . . . .	56
3.9	Limits on the effective Majorana mass and test of the claim of discovery . . . . .	57
<b>4</b>	<b>Search for double beta decay to excited states with CUORICINO</b>	<b>61</b>
4.1	Introduction . . . . .	61
4.2	Double beta decay to excited states . . . . .	61
4.3	$2\nu\beta\beta$ decay of $^{130}\text{Te}$ to the excited state $0_1^+$ . . . . .	64
4.4	Analysis approach . . . . .	65
4.5	Description of the algorithms . . . . .	66
4.6	Evaluation of efficiency and live time . . . . .	68
4.7	Analysis of the CUORICINO data . . . . .	75
4.8	Results . . . . .	83
<b>5</b>	<b>The CUORE experiment</b>	<b>85</b>
5.1	Introduction . . . . .	85
5.2	Overview . . . . .	86
5.3	Shieldings and cryogenics . . . . .	88
5.4	From the single module to the CUORE array . . . . .	90
5.5	Background Reduction for Cuore . . . . .	92
5.5.1	The RAD Measurements . . . . .	93
5.5.2	Surface sensitive bolometers . . . . .	97
<b>6</b>	<b>CUORE data acquisition system</b>	<b>99</b>
6.1	Introduction . . . . .	99
6.2	DAQ system requirements . . . . .	99
6.3	Data acquisition hardware . . . . .	101
6.4	Apollo: the data acquisition software . . . . .	105
6.4.1	The trigger . . . . .	109
6.5	Upgrade of the DAQ system for the Hall C R&D apparatus . . . . .	110
6.6	Upgrade of the CUORICINO DAQ system . . . . .	112
6.6.1	The pulser control subsystem . . . . .	113
6.7	Detector characterization procedure . . . . .	117
6.7.1	Overview . . . . .	118
6.7.2	Implementation . . . . .	120
6.7.3	Tests in Hall C . . . . .	122
	<b>Conclusion</b>	<b>127</b>

## CONTENTS

---

III

List of figures

129

References

141



# Introduction

The last decade has seen unprecedented progress in neutrino physics. Neutrino oscillations, first observed in 1998 by the Super-Kamiokande experiment, are the first direct evidence of new physics beyond the Standard Model.

Thanks to many experiments we have nowadays a rather clear picture of neutrino oscillations, and we are entering the era of precision measurements. There are however several fundamental questions about neutrinos that cannot be addressed by oscillation experiments. Among them there is for example the question about the absolute scale of neutrino masses, which is considered a the key quantity in many theories beyond the Standard Model. Being only sensitive to the neutrino squared mass difference, oscillation experiments are not able to probe this parameter.

Also the mechanism that is responsible for the generation neutrino masses is still unknown. Being electrically neutral, in principle neutrinos could be identical to their own anti-particles. If this condition is verified in nature, the total lepton number is not conserved and neutrinos are said to be Majorana particles. This possibility is clearly ruled out for other fermions, since they have non vanishing electric charge. The only practical approach to disentangle between the Dirac or Majorana nature of neutrinos is to search for neutrinoless double beta decay: it is a rare nuclear process similar to single beta decay, in which only two electrons are emitted. Neutrinoless double beta decay violates the total lepton number by two units, and is allowed only if neutrinos are Majorana particles. In addition, its observation could provide informations on the absolute scale of neutrino masses.

Being a very rare process, the experimental search for neutrinoless double beta decay demands for a huge amount of source isotopes operated in a very low background detector. At present there is no experimental evidence for this decay: several half life lower limits are available, ranging from  $10^{21}$  y to  $10^{25}$  y, depending on the particular isotope. Next generation experiments will have a source mass of about one ton, and will improve the half life sensitivity by about two orders of magnitude with respect to the best limits available at present. This PhD thesis was performed within the CUORE collaboration, which foresees the construction of a ton scale bolometric experiment for the search of neutrinoless double beta decay in  $^{130}\text{Te}$ . Bolometers are calorimeters operated at about 10 mK, able to measure the temperature rise produced by the energy release of an impinging particle. Starting data taking in 2012 in the Laboratori Nazionali del Gran Sasso (LNGS), CUORE plans to reach in five years a sensitivity of the order of

$10^{26}$  y for the neutrinoless double beta decay half life of  $^{130}\text{Te}$ .

The feasibility of a ton scale bolometric detector was widely demonstrated by the pilot experiment CUORICINO, which took data at LNGS in the years 2003-2008. Besides being an invaluable tool for the understanding of the key problematics to be faced in the construction of CUORE, CUORICINO was able to set the best double beta decay half life limit for  $^{130}\text{Te}$ :  $T_{1/2}^{0\nu}(^{130}\text{Te}) > 3.0 \times 10^{24}$  y, at 90% C.L.

One of the two main tasks of this Phd thesis was an analysis of two neutrino double beta decay to the excited state  $0_1^+$  using the data collected by CUORICINO. Even if the decay to the ground state is the most sensitive process for the investigation of the Majorana nature of neutrinos, several other decay modes can be considered as well. The two neutrino decay mode, both to the ground state or to excited states, does not allow to disentangle between Dirac and Majorana neutrinos: it is allowed by the Standard Model and indeed has been observed on several nuclei. Despite being sensitive to the Majorana nature of neutrinos, neutrinoless double beta decay to excited states is not the best process to look at from an experimental perspective. The decay mode to excited states has the nice feature that one or more photons are emitted together with the two electrons. This provides a rather clear signature that allows to obtain a strong reduction of the background. In this work, using a data set collected by CUORICINO in the period between January and August 2007, a lower limit of  $1.4 \times 10^{22}$  y was set for the half life of the two neutrino double beta decay mode of  $^{130}\text{Te}$  to the excited state  $0_1^+$  of  $^{130}\text{Xe}$ .

The other task of this PhD thesis was the development and testing of the data acquisition system for CUORE. After the validation of the digitizing boards and the design and development of the software necessary to operate them, a prototype system was installed in the CUORE R&D apparatus in the Hall C at LNGS for testing purposes. The successful overcome of these tests was followed by a complete upgrade of the Hall C and CUORICINO DAQ systems, that are now regularly used for standard measurements.

This thesis is divided into six chapters. After an overview of the current status in neutrino physics, in chapter 1 the scientific motivations for the search of neutrinoless double beta decay will be introduced. The second chapter will describe the experimental approaches for the search of this process, as well as the most important experiments. In the last part the experimental approach adopted by the CUORE experiment, the bolometric technique, will be discussed. Chapter 3 is devoted to CUORICINO. The experimental apparatus, the background and the double beta decay results of CUORICINO will be presented. Chapter 4 is dedicated to an analysis of the two neutrino double beta decay to excited states with a data set collected by CUORICINO. In chapter 5 the CUORE experiment will be presented, while the last chapter will be devoted to the description of the CUORE data acquisition system and the tests on real detectors performed at LNGS.

# Chapter 1

## Neutrino physics and double beta decay

### 1.1 Introduction

The existence of an electrically neutral half-spin particle was postulated by W. Pauli in 1930, as a “*desperate remedy*” to save the principle of energy conservation in beta decay. It was E. Fermi in 1934 who named this particle the *neutrino*, within the formulation of his theory for beta decay. In 1959 neutrinos were detected for the first time by F. Reines and C. Cowan, observing the inverse beta decay produced by anti-neutrino interactions. In 1962 muon neutrinos were discovered by L.M. Lederman, M. Schwartz and collaborators at Brookhaven National Laboratories. The first direct detection of the tau neutrino was obtained by the DONUT experiment in 2000.

Being electrically neutral leptons, neutrinos only participate to weak interactions: compared to other known particles they have a much smaller probability of interacting with matter. For these reasons neutrino detection has always been a challenging task. Despite the experimental difficulties, neutrino physics has attracted a constantly growing attention, as from the study of these particles it is possible to obtain plenty of information in different research fields.

Great interest in neutrino physics was raised by the discovery of lepton flavor non-conservation. The first hints for this phenomenon date back to the late '60, when a deficit in the solar neutrino flux was observed. It took about thirty years to completely understand the problem. At present many experimental checks have led to the conclusion that this phenomenon is to be ascribed to neutrino oscillations, initially predicted by Pontecorvo in 1957.

One of the most beautiful consequences of oscillations is that neutrinos are massive particles. However there are several questions that cannot be addressed by neutrino oscillation experiments: being sensitive to the difference of the squared values of neutrino masses, oscillation experiments are not able to probe the absolute mass scale. Also the mechanism responsible for the generation of the neutrino masses cannot be

investigated using oscillation experiments. Instead of the usual Dirac field used to describe charged fermions, a neutral fermion could be described as well by a Majorana field. If this condition is verified in nature, neutrinos are indistinguishable from their own anti-particles and lepton number is not conserved.

Investigating such a fundamental property is currently one of the leading research topics in neutrino physics. Neutrinoless double beta decay is a nuclear process that is sensitive to the Majorana nature of neutrinos. This rare process, not allowed in the Standard Model, can occur if neutrinos are Majorana particles and is forbidden if neutrinos are Dirac particles.

In this chapter, after an overview of oscillation results, and a discussion on the possible mechanism for the generation of neutrino masses, the scientific motivation for the search of neutrinoless double beta decay will be presented.

## 1.2 Neutrino Oscillations

Lepton flavor non-conservation is now proved by observations coming from many different contexts and obtained with various experimental approaches. This phenomenon is best explained within the framework of oscillations of massive neutrinos.

Neutrino oscillations arise as a consequence of the fact that neutrino flavor eigenstates produced in weak interaction processes do not coincide with mass eigenstates. Flavor eigenstates  $|\nu_f\rangle$  are related to mass eigenstates  $|\nu_k\rangle$  by the Pontecorvo-Maki-Nakagawa-Sakata (PMNS) neutrino mixing matrix

$$|\nu_f\rangle = \sum_{k=1}^3 U_{fk}^* |\nu_k\rangle, \quad f = (e, \mu, \tau), \quad k = (1, 2, 3) \quad (1.1)$$

The PMNS matrix  $U_{fk}$  in eq. (1.1) can be parameterized as [1]

$$U = \begin{bmatrix} 1 & 0 & 0 \\ 0 & c_{23} & s_{23} \\ 0 & -s_{23} & c_{23} \end{bmatrix} \times \begin{bmatrix} c_{13} & 0 & s_{13}e^{-i\delta} \\ 0 & 1 & 0 \\ -s_{13}e^{i\delta} & 0 & c_{13} \end{bmatrix} \times \begin{bmatrix} c_{12} & s_{12} & 0 \\ -s_{12} & c_{12} & 0 \\ 0 & 0 & 1 \end{bmatrix} \\ \times \begin{bmatrix} e^{i\phi_1/2} & 0 & 0 \\ 0 & e^{i\phi_2/2} & 0 \\ 0 & 0 & 1 \end{bmatrix}. \quad (1.2)$$

where  $c_{ij} \equiv \cos\theta_{ij}$ ,  $s_{ij} \equiv \sin\theta_{ij}$ , and  $\delta$ ,  $\phi_{1,2}$  are the respectively the Dirac and Majorana  $CP$  phases. Since massive eigenstates  $|\nu_k\rangle$  have definite mass and energy, they evolve in time as plane waves. Therefore a neutrino produced with a well defined flavor  $f$  at the interaction point at  $t = 0$ , will be composed at the generic time  $t$  by an admixture of the three flavors:

$$|\nu_f(t)\rangle = \sum_{k=1}^3 U_{fk}^* e^{iE_k t} |\nu_k\rangle = \sum_{k=1}^3 \sum_{f'=e,\mu,\tau} U_{fk}^* U_{kf'} e^{iE_k t} |\nu_{f'}\rangle \quad (1.3)$$

It is clear from eq. (1.3) that there is a non vanishing probability of detecting a neutrino of flavor  $f'$  at time  $t$  after that a neutrino of flavor  $f$  was produced at  $t = 0$ . It reads

$$P(\nu_f \rightarrow \nu_{f'}) \equiv |\langle \nu_{f'} | \nu_f \rangle|^2 = \sum_{j=1}^3 \left| U_{fj}^* U_{f'j} e^{-i \frac{m_j^2 L}{2E}} \right|^2. \quad (1.4)$$

In the simple case with only two neutrino flavors ( $\nu_f, \nu_{f'}$ ) and two mass eigenstates ( $\nu_1, \nu_2$ ), the mixing matrix can be expressed in terms of a single mixing angle  $\theta$  and no phases are present. In this approximation the probability of detecting at a generic time  $t$  a neutrino of flavor  $f'$  after that a state with flavor  $f$  has been produced at  $t = 0$  is given by

$$P(\nu_f \rightarrow \nu_{f'}; t) = \sin^2 2\theta \sin^2 \left( \frac{\Delta m^2}{4E} L \right) \quad (1.5)$$

In eq. (1.5)  $\Delta m^2 = m_2^2 - m_1^2$ , and the energy for relativistic neutrinos have been approximated as  $E_i = \sqrt{p^2 + m_i^2} \simeq p + \frac{m_i^2}{2E}$ . Moreover the time elapsed between the production and the detection point has been replaced by the spatial distance  $L$ , as for relativistic neutrinos  $t \simeq L$ . The flavor transition probability depends therefore on several parameters: the mixing angle  $\theta$ , the neutrino energy  $E$ , the distance  $L$  between the production and the interaction point and the difference of neutrinos squared masses  $\Delta m^2$ . In particular the oscillation probability vanishes for massless neutrinos. The first term of the right hand part of eq. (1.5),  $\sin^2 2\theta$ , depends uniquely on the neutrino mixing angle: the transition probability is maximal for  $\theta = 45^\circ$  and vanishes for  $\theta = 0^\circ$ . The second term in eq. (1.5) depends also on the characteristics of the experimental apparatus that is used to detect neutrinos: its distance from the neutrino source is indeed a critical parameter for the overcome of the experiment. If the argument of the second term is small, the transition probability vanishes. If instead it is too big, uncertainties on the measurement of  $L$  and  $E$  result in this term to be averaged to  $\frac{1}{2}$ .

The two neutrino mixing is a valid approximation for practical description of oscillation experiments. This is a consequence of the experimental evidence for a hierarchical ordering of the mass splittings:

$$|\Delta m_{12}^2| \ll |\Delta m_{13}^2| \simeq |\Delta m_{23}^2| \quad (1.6)$$

In experiments sensitive to  $\Delta m_{23}^2$  the neutrino energies and the typical distances between the production and the detection point are such that the oscillations induced by  $\Delta m_{12}^2$  are negligible:

$$\frac{\Delta m_{12}^2 L}{E} \ll 1 \quad (1.7)$$

The opposite condition is verified in experiments sensitive to  $\Delta m_{12}^2$ , where

$$\frac{\Delta m_{13}^2 L}{E} \simeq \frac{\Delta m_{23}^2 L}{E} \gg 1 \quad (1.8)$$

Even in this case the two neutrinos approximation holds, as the oscillations due to  $\Delta m_{13}^2$  and  $\Delta m_{23}^2$  are very fast and lead to an average effect.

The first hints for lepton flavor non conservation came from the experimental observation that atmospheric and solar neutrino fluxes were smaller than the expected ones. However it was not straightforward to conclude that this deficit in the flux was due to neutrino oscillations, as it could be also ascribed to wrong theoretical predictions of the flux itself. Given the different energies and distances that are involved in solar and atmospheric neutrino experiments, they are sensitive to two different mass scales: solar experiments are able to study a mass splitting of the order of  $\sim 10^{-5} eV^2$  (often called solar mass splitting), while atmospheric neutrino experiments are sensitive to  $\Delta m^2$  of the order of  $\sim 10^{-3} eV^2$  (often called atmospheric mass splitting).

Evidence for atmospheric neutrino oscillations was first obtained by the Super-Kamiokande experiment, which observed an asymmetry in the rate of upward and downward going muon neutrinos [2]. Atmospheric neutrinos are produced by cosmic rays and interact in detectors that are usually located slightly below the Earth's surface. Neutrino energies range from few hundreds of MeV to few hundreds of GeV and they travel distances between few hundreds of km and  $\simeq 12000$  km. Since the flux of cosmic rays is isotropic, neutrinos are produced at the same rate all around the Earth. This implies that the number of neutrinos of a given flavor that come from a given zenith angle  $\theta$  is expected to be equal to the number of neutrinos coming from the opposite zenith angle  $\pi - \theta$ . However Super-Kamiokande data did not present the expected symmetry: the observed flux of  $\nu_\mu$  with energies  $\gtrsim 1$  GeV coming up from the zenith angle  $\pi - \theta$  was only about half of that coming from the zenith angle  $\theta$ . If interpreted in terms of neutrino oscillations, this phenomenon is easily explained. Since the upward-going neutrinos are produced in the atmosphere in the opposite side of the Earth with respect to the detector, they have much distance to travel compared to downward-going neutrinos. Thus the Up-Down asymmetry is explained by the fact that upward-going neutrinos have a bigger probability of oscillating into neutrinos of other flavors, as they travel for longer distances.

Disappearance of muon neutrinos was confirmed later by neutrino accelerator experiments such as MINOS [3] and K2K [4]. These experiments measured the  $\nu_\mu$  flux both in the vicinity of the production point, where no oscillation was expected, and far away from the source, at a distance of  $\simeq 250$  km for K2K and of  $\simeq 735$  km for MINOS. Besides observing a deficit in the number of muon neutrinos in the far detector with respect to what expected from the near-detector measurements, these experiments found

that the energy spectrum of surviving muon neutrinos was distorted in a way that was consistent with the hypothesis of neutrino oscillations.

Neutrinos from the Sun have been detected on earth by several experiments. The first measurements date back to the late '60, with R. Davis' Homestake radiochemical experiment [5]. Further measurements were performed by other radiochemical experiments (SAGE [6] and Gallex-GNO [7]), and water-Cherenkov experiments (Kamiokande and Super-Kamiokande [8]). For years, all these experiments had been finding that the solar  $\nu_e$  flux arriving at the Earth was smaller than the Bahcall-Pinsonneault Standard Solar Model predictions [9].

The conclusive solution of the so called “*solar neutrino problem*” came in 2002 thanks to the Sudbury Neutrino Observatory (SNO) [10], that confirmed that the missing  $\nu_e$  were actually converted into neutrinos of other flavors. The SNO experiment was able to detect solar neutrinos from  ${}^8\text{B}$  using charged current (CC), neutral current (NC) and elastic scattering (ES) interactions. Events from CC interactions, being produced only by  $\nu_e$ , give an estimation of  $\phi(\nu_e)$ , the flux of electron neutrinos from the Sun. NC interactions are initiated with equal cross section by neutrinos of all flavors and give therefore an estimation of  $\phi(\nu_e) + \phi(\nu_\mu + \nu_\tau)$ , the total solar neutrino flux from  ${}^8\text{B}$ . Even ES interactions are initiated by neutrinos of all flavors, but with different cross sections:  $\sigma_e^{ES} \simeq 6.5 \sigma_{\mu,\tau}^{ES}$ . Therefore the measurement of the rate of this process gives an estimation for  $\phi(\nu_e) + \phi(\nu_\mu + \nu_\tau)/6.5$ . The SNO results are summarized in fig. 1.1. The total neutrino flux estimated from NC interactions is in excellent accordance with the SSM predictions. Moreover, the presence of a zone in the plot where all the three measurements overlap, corroborates the interpretation of the results in terms of neutrino flavor conversion.

Solar neutrino data implies that a sensitive fraction of reactor  $\bar{\nu}_e$  that travel more than  $\sim 100$  km should disappear into  $\bar{\nu}$  of different flavors. The phenomenon was confirmed by KamLAND [12], a liquid scintillator experiment that studied reactor  $\bar{\nu}_e$  traveling on average  $\simeq 180$  km before reaching the detector. Besides confirming solar neutrino data, KamLAND observed in the spectrum of surviving  $\bar{\nu}_e$  the typical L/E distortion expected from the neutrino oscillation hypothesis (see fig. 1.2). Since KamLAND is surrounded by several nuclear reactors that are located at a variety of distances from the detector, the distance  $L$  traveled by a given  $\bar{\nu}_e$  is unknown. Consequently, fig. 1.2 plots the data as a function of  $L_0/E$ , where  $L_0 = 180$  km is a flux-weighted average travel distance. Nevertheless, almost two cycles of the sinusoidal structure expected from neutrino oscillations are visible.

Thanks to the data from solar, atmospheric, reactor and accelerator experiments, our understanding of neutrino oscillations has incredibly improved in the recent years. Table 1.1 reports current values for neutrino oscillation parameters extracted from a global fit on most recent experimental data. The two mass splittings, as well as two over three mixing angles have been measured with reasonable precision, while the small mixing angle  $\theta_{13}$  is constrained by an upper limit.

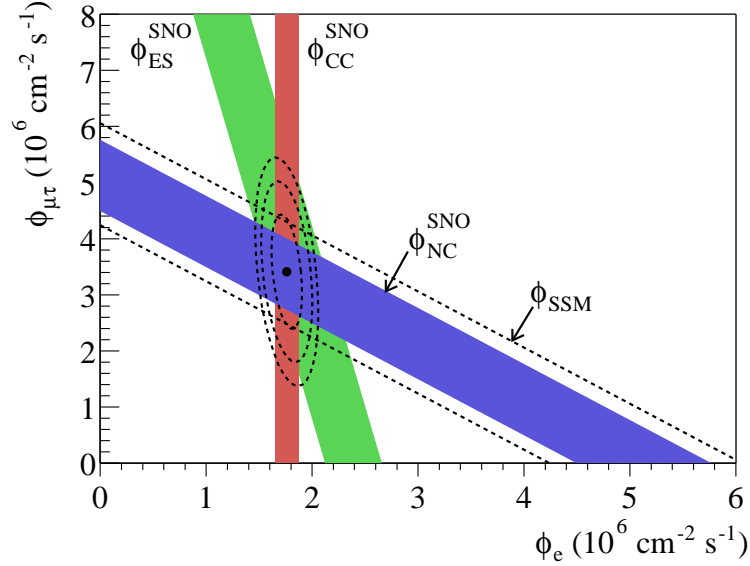


**Figure 1.1:** Fluxes of  $^8\text{B}$  solar neutrinos,  $\phi(\nu_e)$  and  $\phi(\nu_\mu + \nu_\tau)$ , deduced from the three neutrino reactions measured by the SNO experiment. The diagonal bands show the total  $^8\text{B}$  flux as predicted by the SSM (dashed lines) and that measured with the NC reaction in SNO (solid band). The bands represent  $1\sigma$  error. Picture taken from [11].

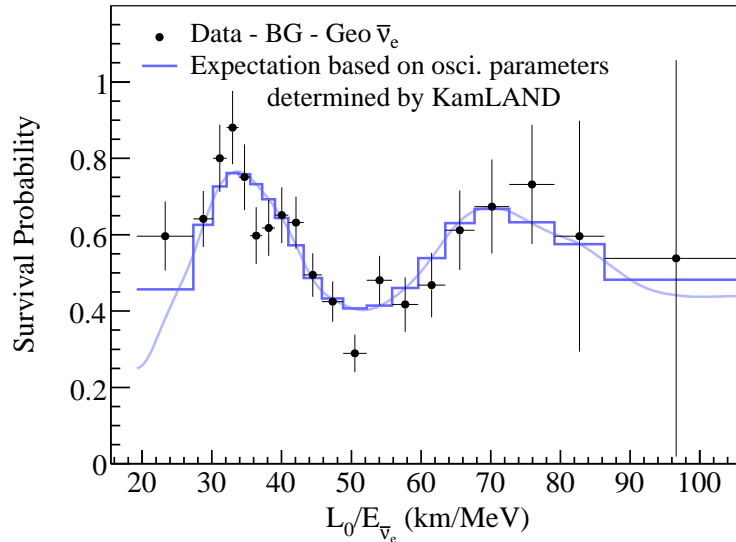


**Figure 1.2:** Electron anti-neutrino survival probability as a function of  $L_0/E$  measured by the KamLAND experiment.  $L_0$  is the effective baseline taken as a flux-weighted average ( $L_0 = 180$  km). Picture taken from [13].

Parameter	Central Value	$3\sigma$
$\Delta m_{21}^2 [10^{-5} eV^2]$	$7.65_{-0.20}^{+0.23}$	$7.05 \div 8.34$
$\Delta m_{23}^2 [10^{-3} eV^2]$	$2.40_{-0.11}^{+0.12}$	$2.07 \div 2.75$
$\sin^2 \theta_{12}$	$0.304_{-0.016}^{+0.022}$	$0.25 \div 0.37$
$\sin^2 \theta_{23}$	$0.50_{-0.06}^{+0.07}$	$0.36 \div 0.67$
$\theta_{13}$	$0.01_{-0.011}^{+0.016}$	$\leq 0.056$

**Table 1.1:** Neutrino oscillation parameters from global fit on most recent experimental data[14].

## 1.3 Neutrino Masses

The Standard Model of Particle Physics assumes that neutrinos are massless particles, as there was no evidence for neutrino masses when this theory was formulated. Oscillation experiments have now changed this scenario, calling for an extension of the theory.

The Standard Model is based on the gauge invariance of the Lagrangian under transformations of  $SU(2)_L \times U(1)_Y$  group. The fermion content of the theory can be written as

$$\begin{aligned}
 \text{quarks} : \quad q_L^f &= \begin{pmatrix} u_L^f \\ d_L^f \end{pmatrix}, & u_R^f, & d_R^f \\
 \text{leptons} : \quad l_L^f &= \begin{pmatrix} \nu_L^f \\ e_L^f \end{pmatrix}, & e_R^f
 \end{aligned}
 \tag{1.9}$$

where the index  $f$  runs over the three quark and lepton families. The fields have been split in left and right handed components using the projection operators  $P_{L,R} = \frac{1}{2}(1 \mp \gamma_5)$ . Left-handed particles are grouped in weak Isospin doublets while right-handed particles are singlets: this reflects the fact that parity violation is maximal: only left-handed fermions participate to weak interactions. Another feature arises from eq. (1.9): there are no right handed neutrinos in the Standard Model, as there is no experimental evidence for such particles.

Masses for charged fermions are generated by the spontaneous breaking of the  $SU(2) \times U(1)$  symmetry group, through the Higgs mechanism. Indeed bare mass terms cannot be introduced in the Lagrangian, as they would break the gauge invariance of the theory.

This problem is overcome by postulating the existence of the Higgs field  $\phi$ , a scalar that transforms as a doublet of the  $SU(2)$  group and has a non vanishing vacuum expectation value:

$$\phi = \frac{1}{\sqrt{2}} \begin{pmatrix} \phi^+ \\ \phi^0 \end{pmatrix}, \quad \langle 0 | \phi | 0 \rangle = \frac{1}{\sqrt{2}} \begin{pmatrix} 0 \\ v \end{pmatrix}. \quad (1.10)$$

Fermion interactions with this field give rise to the so called Yukawa couplings:

$$- \mathcal{L}_Y = \sum_{ff'} \left[ h_D^{ff'} \bar{q}_L^f \phi d_R^{f'} + h_U^{ff'} \bar{q}_L^f \epsilon \phi^* u_R^{f'} + h_E^{ff'} \bar{l}_L^f \phi e_R^{f'} \right] + h.c. \quad (1.11)$$

The  $h_{U,D,E}$  in eq. (1.11) represent the coupling constants between different fields. Substituting the Higgs field with its vacuum expectation value from eq. (1.10), one gets

$$- \mathcal{L}_{Mass} = \sum_{ff'} \left[ M_D^{ff'} \bar{d}_L^f d_R^{f'} + M_U^{ff'} \bar{u}_L^f u_R^{f'} + M_E^{ff'} \bar{e}_L^f e_R^{f'} \right] + h.c. \quad (1.12)$$

where the  $M_{U,D,E}^{ff'}$  are the fermion mass matrices and are given by

$$M_{U,D,E}^{ff'} = h_{U,D,E}^{ff'} \frac{v}{\sqrt{2}}. \quad (1.13)$$

Mass matrices can be diagonalized by mean of a bi-unitary transformation of the form

$$h^{diag} = V_L h V_R^\dagger \quad (1.14)$$

Therefore the mass terms in the Lagrangian can be made diagonal by a redefinition of the fermion fields:

$$\begin{aligned} u_L^{diag} &= V_L^U u_L, & u_R^{diag} &= V_R^U u_R, \\ d_L^{diag} &= V_L^D d_L, & d_R^{diag} &= V_R^D d_R, \\ e_L^{diag} &= V_L^E e_L, & e_R^{diag} &= V_R^E e_R \end{aligned} \quad (1.15)$$

and the diagonal version of the  $h_{U,D,E}^f$  can be related to the fermion masses:

$$m_U^f = h_U^f \frac{v}{\sqrt{2}}, \quad m_D^f = h_D^f \frac{v}{\sqrt{2}}, \quad m_E^f = h_E^f \frac{v}{\sqrt{2}} \quad (1.16)$$

When these field transformations are applied to all the terms of the Lagrangian it turns out that all but the charged current interaction terms are left unchanged. In fact there is only one term that is modified by the redefinition of the fields: the charged current interaction for the quark sector. Since this term couples up-type and down-type quarks, and since these two fields are transformed by two different matrices, flavor mixing occurs in charged current interactions:

$$\mathcal{L}_{CC} = \bar{u}_L \gamma^\mu d_L^f W_\mu^- + h.c. \rightarrow \mathcal{L}_{CC} = \bar{u}_L^{diag} \gamma^\mu V_{CKM} d_L^{diag} W_\mu^- + h.c., \quad (1.17)$$

where  $V_{CKM} \equiv V_L^{U\dagger} V_L^D$  is the Cabibbo-Kobayashi-Maskawa mixing matrix.

When the same procedure is applied to the leptonic sector a fundamental difference arises: since there is no neutrino mass term it is possible to redefine the neutrino fields using the same transformation matrix that has been used for the charged leptons:

$$\nu_L^{diag} = V_L^E \nu_L \quad (1.18)$$

Therefore the equivalent for the  $CKM$  matrix for the lepton sector is given by  $V_{CKM}^{lep} = V_L^{E\dagger} V_L^E \equiv I$ . In other words the lepton fields can be defined in such a way that there is no mixing in the lepton sector. This is a consequence of the fact that neutrinos are massless in the Standard Model and that right handed neutrinos do not exist.

The evidence for neutrino oscillations is obviously in contrast with this picture. Some new information has to be introduced in the theory so that a neutrino mass term can be built and flavor mixing arises also in the leptonic sector.

In general the Lagrangian mass term for a fermion field  $\psi$  has the form

$$- \mathcal{L}_{Mass} = m \bar{\psi} \psi = \bar{\psi}_L \psi_R + \bar{\psi}_R \psi_L, \quad (1.19)$$

Since this term couples the right handed and the left-handed part of a field, both these components must be present. Therefore, in order to build a neutrino mass term, the straightforward extension of the theory consists in the introduction of a right handed particle that is independent from the usual left handed neutrino, so that a mass term of the same form as for charged fermions can be constructed:

$$- \mathcal{L}_D = -m (\bar{\nu}_L \nu_R + \bar{\nu}_R \nu_L) \quad (1.20)$$

A mass term of this form (called Dirac mass term) would arise from Yukawa coupling in full analogy with the case of quarks and charged leptons. However generating the neutrino masses with the Higgs mechanism is somehow unnatural, since the Yukawa couplings for these particles would have to be smaller with respect to the same coupling for other particles by more than six orders of magnitude.

$$\frac{h_N}{h_E} = \frac{m_\nu}{m_e} < 10^{-6} \quad (1.21)$$

However there is for neutrinos the possibility to build another mass term. Consider the particle-antiparticle conjugation operator:

$$\mathcal{C} : \psi \rightarrow \psi^c = \gamma_0 \gamma_2 \bar{\psi}^T \quad (1.22)$$

Under the action of  $\mathcal{C}$  a left-handed field goes into a right-handed one, and viceversa. As a consequence of the fact that neutrino has no electric charge, it is possible that the right handed component of the neutrino field is simply the  $\mathcal{C}$ -conjugated of the left handed field. If this possibility is verified then neutrino is said to be a Majorana particle. In contrast with the Dirac case, where the two components of the field are completely independent, for a Majorana field they are related to each other by particle-antiparticle conjugation:

$$\begin{aligned} \text{Dirac :} \quad \psi_D &= \psi_L + \psi_R \\ \text{Majorana :} \quad \psi_M &= \psi_L + (\psi_L)^c \end{aligned} \tag{1.23}$$

It follows from eq. (1.23) that particles described by a Majorana field are purely neutral, i.e. they coincide with their own anti-particles. It is then clear that the possibility of describing a fermion by a Majorana field only arises for neutrinos, as the other fermions have electric charge. The Lagrangian mass term for a Majorana neutrino  $\nu_L$  can be written as

$$-\mathcal{L} = \frac{1}{2} m (\bar{\nu}_L^c \nu_L + \bar{\nu}_L \nu_L^c) \tag{1.24}$$

In principle neutrinos can have both Majorana and Dirac mass terms. Considering for simplicity the case of only one flavor, it reads

$$-\mathcal{L} = \frac{1}{2} (\bar{\nu}_L^c \ \bar{\nu}_R) \begin{pmatrix} 0 & m_D \\ m_D & M_R \end{pmatrix} \begin{pmatrix} \nu_L \\ \nu_R^c \end{pmatrix} + h.c. . \tag{1.25}$$

In eq. (1.25) the two independent fields  $\nu_L$  and  $\nu_R$  are present,  $m_D$  is the Dirac mass and  $M_R$  is the Majorana mass for  $\nu_R$ . Note that the coefficient  $M_L$  has been set to zero: since in the Standard Model  $\nu_L$  has weak Isospin projection  $I_3 = \frac{1}{2}$ , the corresponding Majorana mass term would be a Isospin triplet and would not be gauge invariant.

The mass matrix introduced in eq. (1.25) can be diagonalized to find the corresponding mass eigenstates:

$$\mathcal{U} \begin{pmatrix} 0 & m_D \\ m_D & M_R \end{pmatrix} \mathcal{U}^T = \begin{pmatrix} m_1 & 0 \\ 0 & m_2 \end{pmatrix}, \quad \begin{pmatrix} \nu_1 \\ \nu_2 \end{pmatrix} = \mathcal{U} \begin{pmatrix} \nu_L \\ \nu_R^c \end{pmatrix}. \tag{1.26}$$

When written in the new basis the neutrino Lagrangian mass term reads

$$-\mathcal{L} = \frac{1}{2} m_1 (\bar{\nu}_1^c \nu_1 + \bar{\nu}_1 \nu_1^c) + \frac{1}{2} m_2 (\bar{\nu}_2^c \nu_2 + \bar{\nu}_2 \nu_2^c) \tag{1.27}$$

where

$$\begin{aligned} \nu_1 &= \cos \theta \nu_L + \sin \theta \nu_R^c \\ \nu_2 &= -\sin \theta \nu_L + \cos \theta \nu_R^c \end{aligned} \quad \tan 2\theta = \frac{m_D}{M_R} \tag{1.28}$$

Few considerations arise from the previous equations. First, as can be seen from eq. (1.27), even in the general case in which also the Dirac mass term  $m_D$  is present, in the mass eigenstates basis neutrinos are described by Majorana fields. In addition, while the Dirac mass  $m_D$ , being generated by the Higgs mechanism, is expected to be more or less of the same order of magnitude of the mass of other fermions, there are no limitations for the Majorana mass  $M_R$ . In particular it can assume arbitrarily large values. If  $M_R \gg m_D$  it turns out from eq. (1.28) that

$$\begin{aligned} \nu_1 &\simeq \nu_L, & m_1 &\simeq \frac{m_D^2}{M_R} \\ \nu_2 &\simeq \nu_R^c, & m_2 &\simeq M_R \end{aligned} \tag{1.29}$$

If this condition is verified, the heavy neutrino  $\nu_2$  is predominantly  $\nu_R^c$  and the light neutrino  $\nu_1$  is essentially the observed particle  $\nu_L$ . Thus the introduction of the Majorana mass term in the Lagrangian leads to a natural explanation for the smallness of neutrino masses: the bigger the mass of the unseen particle  $\nu_R$ , the smaller the mass of  $\nu_L$ .

## 1.4 Open Questions Concerning Neutrino Masses

Being able to measure the neutrino mass-squared differences and two of the three mixing angles, oscillation experiments have greatly improved our understanding of neutrino physics. The most striking consequence of oscillations is that neutrinos have finite mass. However many questions remain unanswered. The absolute scale of neutrino mass, one of the key quantities in many theories beyond the Standard Model, is still unknown. Moreover we are still unable to determine the sign of the atmospheric mass splitting, namely whether neutrino masses are ordered according to the so called *normal* or *inverted* hierarchy. Another fundamental question is the one concerning the nature of neutrino mass, whether it is of Dirac or Majorana type.

### 1.4.1 Neutrino mass hierarchy

Neutrino oscillation data is compatible with three types of neutrino mass spectra, depending on the unknown values of the mass of the lightest neutrino and the sign of the atmospheric mass splitting  $\Delta m_{23}^2$  (see fig. 1.3):

- If  $\Delta m_{23}^2 > 0$ , neutrino mass eigenstates are arranged according to the so called *normal mass hierarchy* and the following relation holds:  $m_1 < m_2 < m_3$ .
- If instead  $\Delta m_{23}^2 < 0$ , mass eigenstates are arranged according to the *inverted mass hierarchy*. In this case the lightest neutrino is  $\nu_3$ , and the two other mass eigenstates are almost equal:  $m_3 < m_1 \simeq m_2$ .

- There is also the possibility that the absolute value of the smaller neutrino mass is much bigger than the big atmospheric mass splitting. In this case, no matter whether the normal or inverted hierarchy holds, all the three neutrino mass eigenstates are almost degenerate.

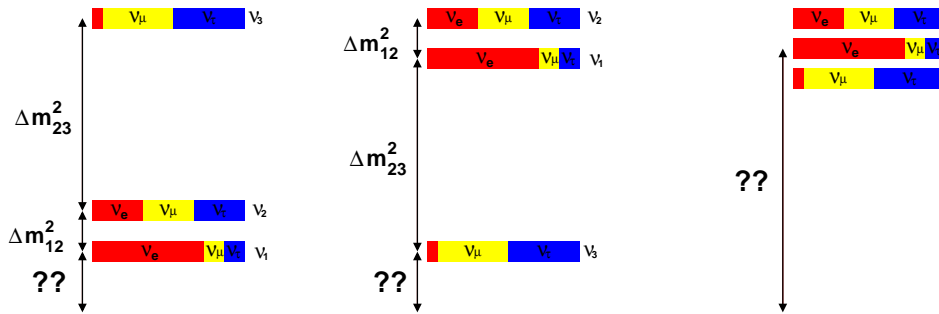


**Figure 1.3:** Pictorial representation of the three mass hierarchy schemes that are compatible with current experimental data. The left picture represents the so-called normal hierarchy. The central picture represent the so called inverted hierarchy, while the right picture represents the degenerate case, where the three neutrino masses are almost equal and are much bigger than the solar and atmospheric mass splittings. The three colors on each neutrino mass eigenstate represent the respective projection on the three flavor eigenstates.

### 1.4.2 Absolute measurement of neutrino mass

Limits on absolute neutrino masses come from cosmological constraints and from non oscillation experiments.

Non oscillation experiments are based on the study of single and double beta decay. The discussion here will be limited to single beta decay, as double beta decay will be widely discussed later.

Direct neutrino mass measurements are based on the analysis of the kinematics of charged particles emitted together with neutrinos in various weak decays. The most sensitive measurements, involving electron neutrinos, are based on the study of the shape of the  $\beta$  spectrum end-point.  $\beta$ -decay experiments are sensitive to the effective electron neutrino mass  $m_\beta$ , defined as

$$m_\beta^2 = \sum_{i=1}^3 |U_{ei}|^2 m_i^2. \quad (1.30)$$

Current best limits on  $m_\beta$  come from the Mainz [15] and Troitsk [16] tritium  $\beta$ -decay experiments:  $m_\beta \lesssim 2.1eV$ . Next generation experiments plain to further constraint  $m_\beta$  in the sub-eV range, studying  $\beta$ -decay of tritium (KATRIN [17]) and  $^{187}\text{Re}$  (MARE [18]).

Cosmological constraints on neutrino masses come from the observation of the Cosmic Microwave Background anisotropies and from the study of large scale structures. These observations are sensitive to the sum of the three neutrino masses,  $\Sigma = m_1 + m_2 + m_3$ . Limits on neutrino masses range from few eV to few hundreds of meV, depending on the data sets that are being considered. However these constraints are less trustworthy if compared to the ones obtained in laboratory experiments, as they depend on cosmological models.

### 1.4.3 Dirac and Majorana neutrinos

Oscillation experiments and direct search for neutrino mass are not affected by the nature of the neutrino mass. The physics involved in these kind of measurements is the same, regardless of whether neutrinos are Dirac or Majorana. The most promising approach to discriminate between these two possibilities is to search for neutrinoless double beta decay ( $0\nu\beta\beta$ ). It will be shown in the following section that the observation of this process would prove that neutrinos are Majorana particles. Neutrinoless double beta decay experiments are sensitive to the so called *effective Majorana mass*,  $m_{\beta\beta}$ :

$$m_{\beta\beta} = \left| \sum_{j=1}^3 U_{ej}^2 m_j \right| = \left| \sum_{j=1}^3 |U_{ej}|^2 e^{i\phi_j} m_j \right|. \quad (1.31)$$

In contrast to single beta decay, where  $m_{\beta}$  was a function of the three  $|U_{ei}|^2$ ,  $m_{\beta\beta}$  is a function of the  $U_{ei}^2$  and is therefore sensitive to the two Majorana phases. Since the  $U_{ei}$ , as well as the two squared mass differences, are known from oscillation experiments,  $m_{\beta\beta}$  can be written in terms of only three unknown parameters: the mass of the lightest neutrino and the two Majorana CP phases. The result is shown in fig. 1.4, where the allowed values for  $m_{\beta\beta}$  are plotted as a function of the lightest neutrino mass.

The green band represents the allowed parameter space in the case of inverted mass hierarchy, while the red band corresponds to the case of normal mass hierarchy. The two bands overlap in the zone of degenerate mass hierarchy (where the mass of the lightest neutrino is  $\gtrsim 10^{-2}eV$ ). Double beta decay experiments with better sensitivity are able to probe smaller values of  $m_{\beta\beta}$ . As can be seen from fig. 1.4, observation of double beta decay would not only imply that neutrinos are Majorana particles: it would also provide information on the neutrino mass hierarchy and on the absolute scale of neutrino mass. If instead this process is not observed, it cannot be concluded that neutrinos are Dirac particles: the presence of the vertical dip in the normal hierarchy band (which correspond to a particular combination of the two Majorana phases) represent the fact that  $m_{\beta\beta}$  could vanish, even if neutrinos are Majorana particles.

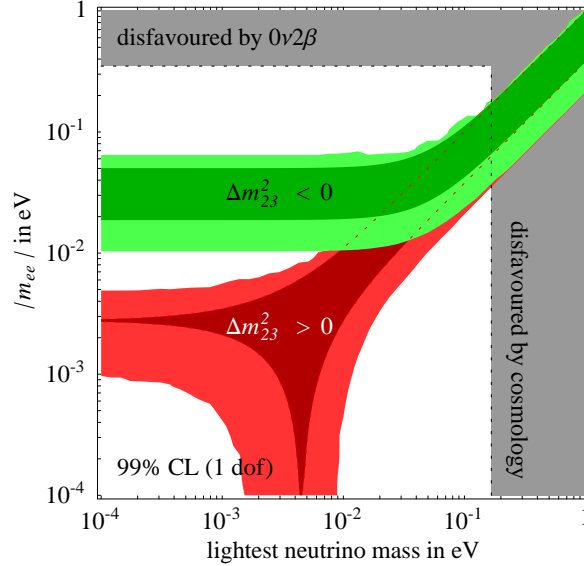


**Figure 1.4:** Allowed values for the effective Majorana mass as a function of the mass of the lightest neutrino. The green band represents the allowed value in the case of inverted neutrino mass hierarchy, while the red band is for the normal hierarchy case. The darker bands represent the allowed regions that would be obtained if the parameters from oscillation experiments were measured with infinite precision. The gray regions represent the parameter space that is excluded by double current double beta decay experiments and by cosmological observations. Picture taken from [19].

## 1.5 Double beta decay

Double beta decay is a rare spontaneous process in which a nucleus changes its atomic number by two units:

$$(A, Z) \rightarrow (A, Z \pm 2). \quad (1.32)$$

Its existence was first proposed in 1935 by M. Goeppert-Mayer [20]: using the the new Fermi theory for  $\beta$ -decay, she estimated that the half-life for this process had to be bigger than  $10^{17}$  years.

Being a second order process, double beta decay has a very slow rate and can occur only in nuclei where single  $\beta$ -decay is forbidden. The parent nucleus  $(A, Z)$  must be less bound than the final one  $(A, Z \pm 2)$  but more bound than the intermediate nucleus  $(A, Z \pm 1)$ . This condition is verified in nature for several nuclei with an even number of protons and neutrons (see fig. 1.5), as a consequence of the “pairing term” in the nuclear binding energy [21], that favors energetically the even-even nuclei with respect to the odd-odd ones.

If accompanied by the emission of two neutrinos (see fig. 1.6(a)), double beta decay is a second order process allowed in the Standard Model ( $2\nu\beta\beta$ ). Indeed, it was detected for the first time in  $^{82}\text{Se}$  in 1987 [22] and is now observed on several other nuclei

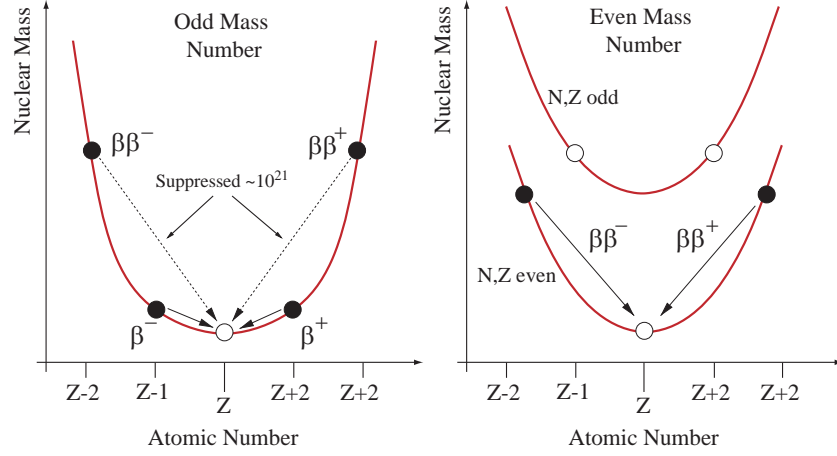


**Figure 1.5:** Atomic mass as a function of the atomic number  $Z$  in the case of a isobar multiplet with  $A$  even (left) and  $A$  odd (right).

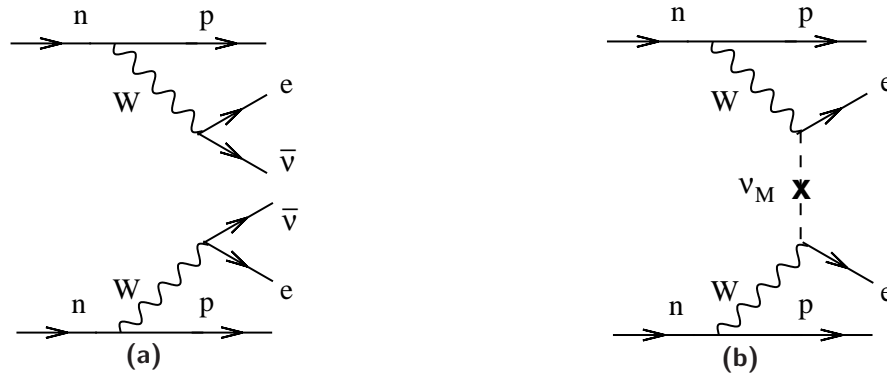


**Figure 1.6:** Double beta decay diagrams for the  $2\nu\beta\beta$  mode (left) and the  $0\nu\beta\beta$  mode (right). The  $0\nu\beta\beta$  diagram assumes that the process is mediated by the exchange of a Majorana neutrino (see the text).

(half-lives range from  $\sim 10^{18}$  to  $\sim 10^{22}$  years).

This decay conserves lepton number, cannot discriminate between Dirac and Majorana neutrinos and does not depend significantly on neutrino masses.

There is also the possibility for double beta decay to occur without emission of neutrinos. This decay mode is forbidden in the Standard Model, as it violates the lepton number by two units. Neutrinoless double beta decay can proceed through many different mechanisms: almost any physics that violates the total lepton number can generate it [23]. However, no matter which particular mechanism holds, this decay would imply the existence of a Majorana neutrino mass term [24]. This is shown in fig. 1.7: the  $0\nu\beta\beta$  decay can be inverted to produce a  $\bar{\nu}_e$  going into a  $\nu_e$  or, in other words, a Majorana mass term.

The simplest way to obtain neutrinoless double beta decay is by the exchange of a massive Majorana neutrino (see fig. 1.6(b)). The rate of this process can be written

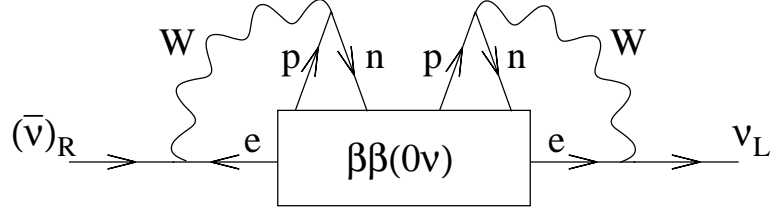


**Figure 1.7:** Conversion from  $\bar{\nu}_e$  to  $\nu_e$  by a  $0\nu\beta\beta$  interaction. This diagram proves that the existence of  $0\nu\beta\beta$ -decay would imply a Majorana mass for neutrino, no matter what is the mechanism that gives rise to the transition.

as [25]

$$[T_{1/2}^{0\nu}]^{-1} = G_{0\nu} |M_{0\nu}|^2 \langle m_{\beta\beta} \rangle^2 \quad (1.33)$$

where  $G_{0\nu}$  and  $M_{0\nu}$  are respectively the phase space factor and the nuclear matrix element for the  $0\nu\beta\beta$  transition, and  $m_{\beta\beta}$  is the effective Majorana mass already discussed in sec. 1.4.3.

Apart for a controversial claim (which will be discussed later), neutrinoless double beta decay has never been observed. The experimental lower limits for the half-lives are reported for a set of commonly studied isotopes in tab. 1.2.

Parent Isotope	$T_{1/2}^{0\nu}(y)$	Reference
$^{48}\text{Ca}$	$> 1.4 \times 10^{22}$	[26]
$^{76}\text{Ge}$	$> 1.9 \times 10^{25}$	[27]
$^{76}\text{Ge}$	$1.19 \times 10^{25}$	[28]
$^{82}\text{Se}$	$> 1 \times 10^{23}$	[29]
$^{96}\text{Zr}$	$> 1.0 \times 10^{21}$	[30]
$^{100}\text{Mo}$	$> 4.6 \times 10^{23}$	[29]
$^{116}\text{Cd}$	$> 1.7 \times 10^{23}$	[31]
$^{130}\text{Te}$	$> 3.0 \times 10^{24}$	[32]
$^{136}\text{Xe}$	$> 1.2 \times 10^{24}$	[33]
$^{150}\text{Nd}$	$> 1.8 \times 10^{22}$	[34]

**Table 1.2:** Commonly studied double beta decay isotopes and best lower limits for the  $0\nu\beta\beta$  half lives. The claim of observation in  $^{76}\text{Ge}$  will be discussed later.

### 1.5.1 Nuclear matrix elements

It has been discussed in sec. 1.5 that without making any assumption on the mechanism that generates neutrinoless double beta decay, the existence of this process implies that neutrinos are Majorana particles. However, in order to extract informations on the neutrino mass hierarchy and the absolute mass scale, some assumptions must be made

on the mechanism that is responsible for this process. The simplest possibility is to assume that the  $0\nu\beta\beta$ -decay occurs by the exchange of a light Majorana neutrino. It is clear from eq. (1.33) that, even under this assumption, the phase space factor  $G_{0\nu}$  and the nuclear matrix element (NME)  $M_{0\nu}$  must be known in order to extract the value of  $m_{\beta\beta}$ . Moreover, a strong evidence of neutrinoless double beta decay can be obtained only if a positive signal is seen in several isotopes. This condition is necessary to rule out the possibility that the observed signal is produced by some other unknown rare process able to mimic the  $0\nu\beta\beta$  experimental signature. However, since different isotopes have different values for  $G_{0\nu}$  and  $M_{0\nu}$ , these quantities must be known in order to compare experiments. While the phase space factor can be evaluated exactly, NME represents the biggest source of theoretical uncertainty in the evaluation of  $m_{\beta\beta}$ .

Nuclear matrix elements depend on the structure of the parent and daughter nuclei, as well as the intermediate one. Since a many bodies problem must be solved, the calculation cannot be carried out analytically, but requires numerical computations in which several approximations are introduced. There are two basic approaches for the evaluation of nuclear matrix elements, the quasi-particle random phase approximation (QRPA) and the nuclear shell model (NSM).

In NSM interactions are described by an effective Hamiltonian which is diagonalized over all configurations of a chosen subset of valence single-particle states. In principle NSM calculations are more reliable, as they require few approximations. However such calculations are computationally intensive, which places a practical limit on the number of single-particle valence states that can be considered. For this reason the QRPA approach is usually preferred. QRPA calculations use a larger valence space with respect to NSM, but the interaction strengths are parameterized, and only a subset of the possible configurations are taken into account. In QRPA particle-particle interactions are fixed by a parameter,  $g_{pp}$ , which is derived in various ways by different authors and lead in the past to a significant spread in the results.

Recently, thanks to improvements in the treatment of short-range correlations in the nucleon-nucleon interactions, and to the use of  $2\nu\beta\beta$  NME to constraint some parameters in the  $0\nu\beta\beta$  NME calculations, the spread in the results of different research groups was significantly reduced, and now the NSM and the various QRPA calculations lie within a factor of two to each other. Figure 1.8 shows the nuclear matrix element calculations for various  $0\nu\beta\beta$  isotopes using the QRPA and the NSM approach.

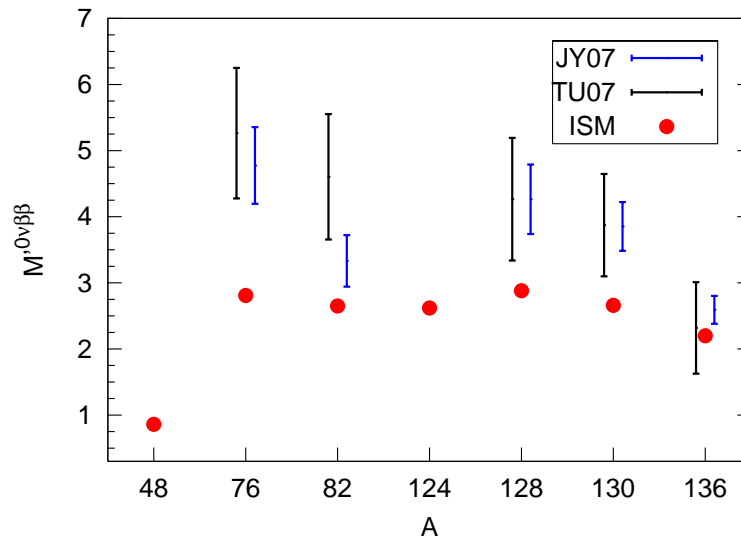


**Figure 1.8:** Nuclear matrix element calculations for several  $0\nu\beta\beta$  isotopes using QRPA (black and blue bars) and NSM (red dots). The bars represent the spread introduced in QRPA calculations by the different choices for the coupling constant  $g_A$ . Picture taken from [35].

# Chapter 2

## Experimental search for double beta decay

### 2.1 Introduction

Being a very rare process, observation of double beta decay is a challenging task from an experimental perspective. By all means the main problem to be faced is the reduction of the background, even if double beta decay experiments need also huge masses and excellent energy resolutions.

In this chapter the experimental approaches to the search of double beta decay will be discussed. After an overview of the fundamental features common to all double beta decay experiments, the main experimental techniques are reviewed and the most important past, present and future experiments are presented. In the last part of this chapter the experimental approach used in the CUORE experiment, the bolometric technique, is presented.

### 2.2 Fundamentals of $0\nu\beta\beta$ experiments

The amount of energy released in double beta decay, usually called  $Q$ -value, is given by the mass difference between the parent and the daughter nucleus, subtracted by the masses of the two emitted electrons:

$$Q_{\beta\beta} = M_p - M_d - 2m_e . \quad (2.1)$$

In the  $2\nu\beta\beta$  decay mode the two neutrinos carry away part of the energy, giving rise to a continuous spectrum for the sum energy of the two electrons that extends up to the  $Q$ -value of the decay. In the  $0\nu\beta\beta$  decay mode, since no neutrinos are emitted, the sum energy of the two electrons is fixed, and is equal to the  $Q$ -value of the decay. Therefore, at least in principle, the signature of neutrinoless double beta decay is very

clear: a sharp peak is produced in the energy spectrum, and the two emitted electrons point to the same interaction vertex.

In spite of such characteristic imprint, the rate of double beta decay is so slow that its identification is made very difficult. The signal must be disentangled from the background produced by natural and cosmogenic-induced activity, which can deposit energy in the detector in the same region of the spectrum where the double beta decay signal is expected. In order to maximize the signal to background ratio, two complementary approaches are adopted in double beta decay experiments: on one side much effort is spent in the understanding and the reduction of background, while on the other side the amount of the isotope that is put under observation is made as big as possible, so that the chance for the decay to occur is maximized.

Energy resolution is another important feature in double beta decay experiments: since background events usually produce a continuum in the energy spectrum, the possibility to shrink the energy window in which the  $0\nu\beta\beta$  signal is expected leads to an increase of the signal to background ratio. Concerning this point, it is worth noticing that even in the best condition of a “zero background” experiment, there is an irreducible source of background that comes from the tail of the  $2\nu\beta\beta$  decay channel. As depicted in fig. 2.1, which shows the sum energy spectrum for the two emitted electrons, an experiment with poor energy resolution would not be able to disentangle the end point of the  $2\nu\beta\beta$  decay mode from the monochromatic line produced by the  $0\nu\beta\beta$  decay mode.

The sensitivity of an experiment is defined as the half life corresponding to the minimum number of signal events observable above background at a given confidence level. For experiments in which the number of background counts scales as the total mass of the detector, it can be expressed as [25]

$$S^{0\nu}(n_\sigma) = \frac{\ln 2}{n_\sigma} \epsilon N_a \frac{\eta}{A} \sqrt{\frac{M \cdot t}{b \cdot \Delta E}}. \quad (2.2)$$

Equation (2.2) can be easily obtained in the assumption of Poisson statistics, starting from the consideration that a positive signal is found if the number of observed events in the region of the  $0\nu\beta\beta$  peak differs by more than  $n_\sigma$  standard deviations from the number of background events in the same region. In eq. (2.2)  $\epsilon$  is the detection efficiency,  $N_a$  is the Avogadro number,  $\eta$  is the isotopic abundance of the studied nucleus,  $A$  is its atomic mass number,  $M$  is the total detector mass,  $t$  is the live time of the experiment,  $\Delta E$  is the energy resolution and  $b$  is the background, expressed in terms of counts/(keV · kg · years).

The detector sensitivity assumes a different form if no background is present (or at least the number of background counts is negligible over the life of an experiment):

$$S^{0\nu} \sim \epsilon \cdot \eta \cdot M \cdot t. \quad (2.3)$$

Thus, in contrast to the previous case, in which the sensitivity scales as the squared

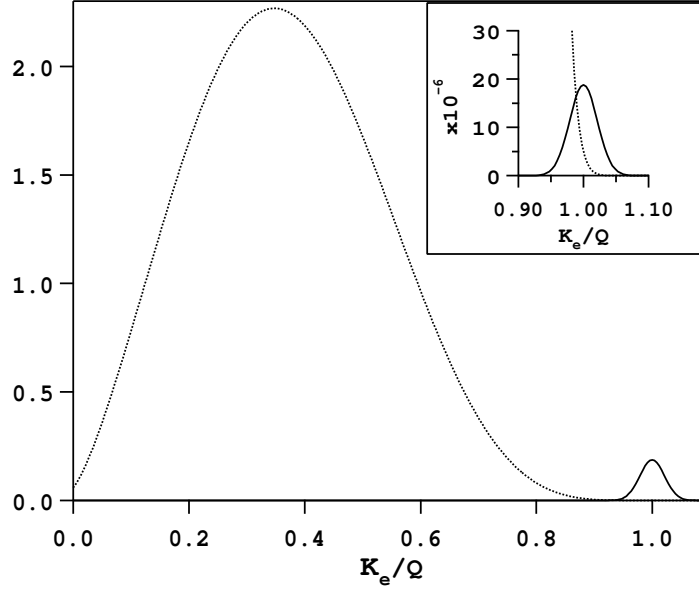


**Figure 2.1:** Illustration of the spectra of the sum of the electron kinetic energies  $K_e$  ( $Q$  is the endpoint) for the  $2\nu\beta\beta$  (dotted curve) and  $0\nu\beta\beta$  decays (solid curve). The spectra are convolved with an energy resolution of 5%. The small insert shows how a poor energy resolution can lead to the confusion of the  $0\nu\beta\beta$  peak with the tail of the  $2\nu\beta\beta$  spectrum.

root of the mass  $M$  and of the measurement time  $t$ , in a "zero background" experiment the dependence on these two parameters is linear.

In the previous chapter the expression for neutrinoless double beta decay was discussed. Equation (1.33) can be inverted to find the effective Majorana mass  $m_{\beta\beta}$  corresponding to certain values for the phase space factor  $G_{0\nu}$ , the nuclear matrix element  $M_{0\nu}$  and the half life  $T_{1/2}^{0\nu}$ :

$$\langle m_{\beta\beta} \rangle = \frac{1}{\sqrt{T_{1/2}^{0\nu} G_{0\nu} |M_{0\nu}|^2}} \quad (2.4)$$

By replacing the half life with the experimental sensitivity in eq. (2.4), it can be seen that the sensitivity on  $m_{\beta\beta}$  scales as the fourth root of  $(M \cdot t)/(b \cdot \Delta E)$  in an experiment with non negligible background and it scales as the squared root of  $(M \cdot t)$  in a "zero background" experiment. In other words, if all other parameters remain fixed, improving the sensitivity on  $m_{\beta\beta}$  by an order of magnitude requires a mass increase by a factor of  $10^4$  in the first case, and by a factor of 100 in the second case.

In order to compare the sensitivity of experiments that search for double beta decay using different isotopes, it is possible to define the nuclear factor of merit  $F_N$ :

$$F_N = m_e^2 G_{0\nu} |M_{0\nu}|^2, \quad (2.5)$$

where  $m_e$  is the electron mass and  $F_N$  has dimensions of  $time^{-1}$ . Using the nuclear factor of merit, eq. (2.4) becomes

$$\langle m_{\beta\beta} \rangle = \frac{m_e}{\sqrt{S^{0\nu} \cdot F_N}}. \quad (2.6)$$

Thus different experiments can be compared using the quantity  $S^{0\nu} \cdot F_N$ , where the former factor accounts for the experimental features, while the latter describes the  $0\nu\beta\beta$  isotope candidate.

Table 2.1 reports the nuclear factor of merit, the isotopic abundance and the  $Q$ -value for several commonly used double beta decay isotopes. It is clear from eq. (2.2) that high isotopic abundances are preferable, as they correspond to an increase of the number of  $0\nu\beta\beta$  nuclei that are put under observation. Despite being rather expensive, isotopic enrichment is often a forced choice for those candidate nuclei that have low natural abundances.

Parent Isotope	$F_N$ [ $y^{-1}$ ]	$Q_{\beta\beta}$ [keV]	$\eta$ [%]
$^{48}\text{Ca}$	$0.54 \cdot 10^{-13}$	4271	0.19
$^{76}\text{Ge}$	$0.73 \cdot 10^{-13}$	2039	7.4
$^{82}\text{Se}$	$1.7 \cdot 10^{-13}$	2995	8.7
$^{100}\text{Mo}$	$5.0 \cdot 10^{-13}$	3034	9.6
$^{116}\text{Cd}$	$1.3 \cdot 10^{-13}$	2902	7.5
$^{130}\text{Te}$	$4.2 \cdot 10^{-13}$	2530	34.
$^{136}\text{Xe}$	$0.28 \cdot 10^{-13}$	2479	8.9
$^{150}\text{Nd}$	$57. \cdot 10^{-13}$	3367	5.6

**Table 2.1:** Nuclear factor of merit,  $Q$ -value and natural abundance ( $\eta$ ) for several double beta decay isotopes. The values of  $F_N$  are from [36].

Isotopes with high  $Q$ -value are also a better choice, for several reasons. First, the background from natural radioactivity decreases with increasing  $Q$ . A marking point is represented by the 2615 keV line from  $^{208}\text{Tl}$ , the highest energy  $\gamma$ -line from natural radioactivity. Isotopes with  $Q$ -values above this energy benefit from a much lower background level. Other reasons to prefer big  $Q$ -values are represented by the fact that the phase space factor that appears in the formula for the decay rate scales as  $G_{0\nu} \sim Q^5$  [23], and that the fraction  $F$  of the  $2\nu\beta\beta$  counts in the region of the  $0\nu\beta\beta$  peak scales as  $F \sim 1/Q^5$  [37].

## 2.3 Double beta decay experiments

Early double beta decay experiments used an indirect approach, based on the identification of an excess of concentration of the daughter nuclei in a sample containing the parent isotope. Now that two neutrino double beta decay has been measured for

several isotopes, the indirect approach is no longer of great interest, as it is not able to distinguish between the  $2\nu\beta\beta$  and the  $0\nu\beta\beta$  decay modes. Current experiments exploit instead a direct approach, based on the detection of the two electrons emitted in the decay.

Experiments using the direct approach can be divided in two groups: those in which the isotope under study is contained within the active mass of the detector, and those in which the detector and the decaying nucleus are separated. The most representative detectors of the two groups are respectively calorimeters and tracking devices. The two approaches have different advantages.

Calorimeters have usually excellent energy resolution and almost 100% efficiency. Moreover the experimental sensitivity can be improved rather easily by increasing the detector mass. The disadvantage of this kind of devices is that they are not able to identify the two electrons, as they can only measure the total released energy.

Tracking detectors, which instead have the possibility to identify separately the two electrons, can reach very low background levels. The main drawback of this kind of detectors is an intrinsically poor energy resolution. In order for the two electron to be detected, they must escape from the material where they are produced. In doing so, a small part of their energy is released within the passive material containing the  $0\nu\beta\beta$  isotopes, thus producing a degradation of the resolution. This problem is usually overcome by using source materials in the form of thin foils, but this introduces non trivial problems when increasing the mass of the  $0\nu\beta\beta$  source.

### 2.3.1 Past and present experiments

Past and running double beta decay experiments have typical sensitivities that allow to span the effective Majorana mass corresponding to the degenerate neutrino mass hierarchy pattern (see fig. 1.4).

The best half life limit for  $0\nu\beta\beta$  decay (a complete list is in tab. 1.2) has been obtained so far in  $^{76}\text{Ge}$  by the Heidelberg-Moscow collaboration, using semiconductor detectors. Similar results were also achieved in the IGEX experiment [38]. The big advantage of semiconductor detectors is their excellent energy resolution (about 4 keV at 2 MeV). Even if these devices can only measure the sum energy of the two electrons emitted in  $0\nu\beta\beta$  decay, some background reduction can be obtained by exploiting pulse shape analysis. High purity Germanium detectors (HPGe) are a typical example of the *source = detector* approach: the investigated nucleus is  $^{76}\text{Ge}$ , having a Q-value of 2039 keV. The Heidelberg-Moscow experiment took data in the period 1999-2003 in the Laboratori Nazionali del Gran Sasso (LNGS) using five HPGe detectors. The total detector mass was 11 kg, enriched to about 86% in  $^{76}\text{Ge}$ . A background of 0.12 counts/(keV · kg · y) was obtained around the Q-value of the decay. With a statistics of 35.5 kg · y in  $^{76}\text{Ge}$  the half life limit obtained by the Heidelberg-Moscow collaboration is  $T_{1/2}^{0\nu} > 1.9 \times 10^{25} \text{y}$  at 90% C.L. [27]. Using NME calculations from [39] this corresponds to a limit for the effective Majorana mass of  $m_{\beta\beta} < 0.35 \text{ eV}$ . In 2001 a

subgroup of the collaboration found a small peak at the expected position [40, 28] (see fig. 2.2) and reported an evidence for neutrinoless double beta decay in  $^{76}\text{Ge}$  with an half life in the range  $0.7 \div 4.2 \times 10^{25}\text{y}$  ( $3\sigma$ ). Using NME from [39], this result would convert into a value for  $m_{\beta\beta}$  in the range  $0.2 \div 0.6\text{ eV}$ . However, the discussion concerning the possible evidence is quite controversial, mainly because the understanding of the background in the region of the peak is not so clear. Further discussion on this point is reported in chapter 3, where the results of the CUORICINO experiment are presented.

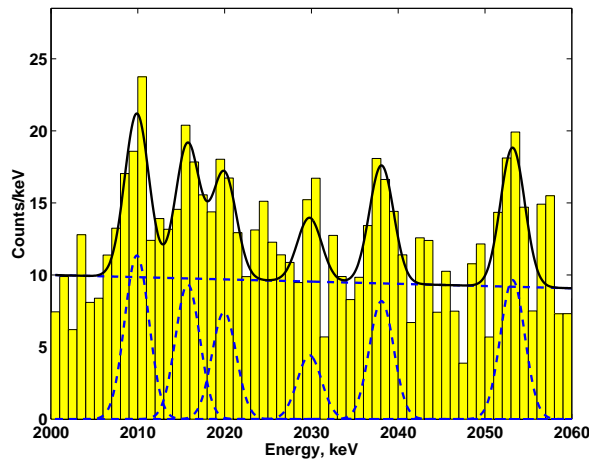


**Figure 2.2:** Energy spectrum measured by the Heidelberg-Moscow experiment around the  $Q$ -value of  $^{76}\text{Ge}$  (2039 keV). Picture taken from [28].

The CUORICINO experiment [32] will be widely discussed in the following chapters. It uses  $\text{TeO}_2$  bolometers operating at  $\sim 10\text{ mK}$  to search for neutrinoless double beta decay in  $^{130}\text{Te}$ . The detector is located at LNGS, under a 3400 m w.e. rock shield. With a background level in the region of the  $0\nu\beta\beta$  peak of  $0.2\text{ counts}/(\text{keV} \cdot \text{kg} \cdot \text{y})$ , an energy resolution of  $\sim 7\text{ keV}$  at 2.6 MeV and a statistics of  $11.83\text{ kg} \cdot \text{y}$ , CUORICINO obtained a limit on the  $^{130}\text{Te}$   $0\nu\beta\beta$  half life of  $T_{1/2}^{0\nu} > 3.0 \times 10^{24}\text{y}$ . Using NME from [41] this translates into a limit on the effective Majorana mass of  $m_{\beta\beta} < 0.2 \div 0.68\text{ eV}$ .

Other competitive limits on neutrinoless double beta decay come from the Neutrino Ettore Majorana Observatory (NEMO 3 [42]). Being a tracking experiment, NEMO 3 is not only able to measure the total released energy, but also the energy of the single electrons, their angular distribution and the position where they are produced. NEMO 3 is located in the Frejus Underground Laboratory (France) under a 4800 m w.e. rock shield. The detector has a cylindrical structure composed by 20 identical sectors. In each sector a thin foil  $0\nu\beta\beta$  source ( $30\text{-}60\text{ g}/\text{cm}^2$ ) is surrounded by a He-filled tracking detector consisting in drift cells operating in Geiger mode. A magnetic field facilitates identification of the background produced by electron-positron pairs. The tracking chambers are surrounded by plastic scintillators to measure the energy of the two electrons. Thanks to the easy way in which the source foils can be

replaced in the detector, NEMO 3 can be used to study any kind of  $0\nu\beta\beta$  isotope. Its great background rejection capabilities make this detector an ideal tool to study the two neutrino double beta decay mode. At present seven isotopes have been investigated,  $^{100}\text{Mo}$ ,  $^{82}\text{Se}$ ,  $^{116}\text{Cd}$ ,  $^{150}\text{Nd}$ ,  $^{96}\text{Zr}$ ,  $^{130}\text{Te}$  and  $^{48}\text{Ca}$ , but the source mass (about 10 kg) is fairly dominated by  $^{100}\text{Mo}$  (about 7 kg) and  $^{82}\text{Se}$  (about 1 kg). Figure 2.3 gives an idea of the background rejection capabilities of this experiment. It represents the measured  $2\nu\beta\beta$  spectra for  $^{100}\text{Mo}$  and  $^{82}\text{Se}$ . The corresponding values for the  $2\nu\beta\beta$  half lives are  $T_{1/2}^{2\nu} = [7.11 \pm 0.02(\text{stat}) \pm 0.54(\text{syst})] \times 10^{18} \text{ y}$  for  $^{100}\text{Mo}$  and  $[9.6 \pm 0.3(\text{stat}) \pm 1.0(\text{syst})] \times 10^{19} \text{ y}$  for  $^{82}\text{Se}$ . Limits on the  $0\nu\beta\beta$  decay channel have also been obtained by NEMO 3:  $T_{1/2}^{0\nu} > 4.6 \times 10^{23} \text{ y}$  ( $^{100}\text{Mo}$ ) and  $T_{1/2}^{0\nu} > 1.0 \times 10^{23} \text{ y}$  ( $^{82}\text{Se}$ ). The corresponding upper limits for the effective Majorana mass range from 0.7 to 2.8 eV for  $^{100}\text{Mo}$  and from 1.7 to 4.9 eV for  $^{82}\text{Se}$  (see references in [29] for the NME used to obtain these limits).

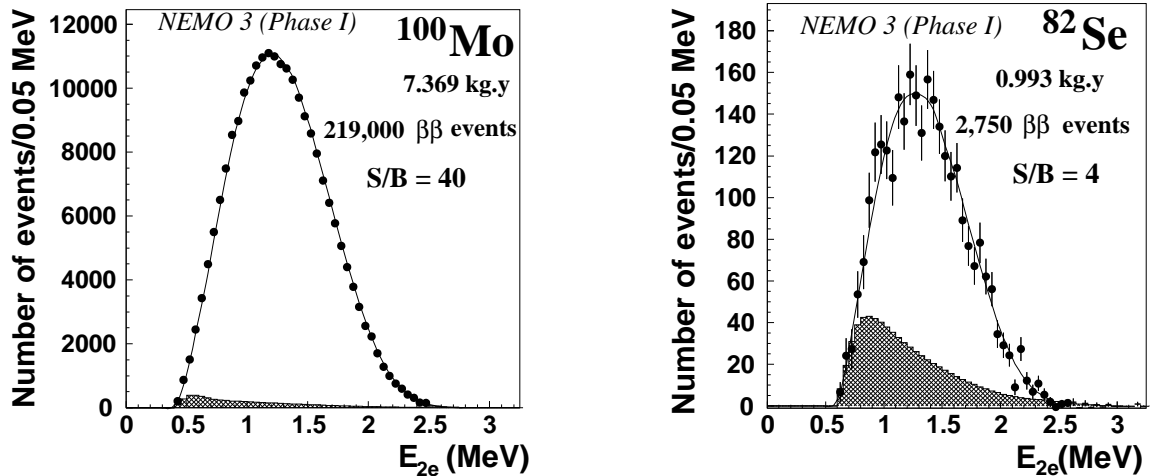


**Figure 2.3:** Two neutrino double beta decay spectra after background subtraction for  $^{100}\text{Mo}$  (left) and  $^{82}\text{Se}$  (right) measured by NEMO 3. The black dots represent the data, the solid line is the  $2\nu\beta\beta$  spectrum expected from simulations and the shaded histogram is the subtracted background. Picture taken from [29].

### 2.3.2 Future experiments

In this section a brief description of the experiments that will start in the next years is presented (see tab. 2.2). Next generation experiments aim at the investigation of the effective neutrino Majorana mass in the range corresponding to the inverted mass hierarchy region. Given the present limits, this corresponds to an increase of about one order of magnitude in the  $m_{\beta\beta}$  sensitivity. The projected sensitivity will be achieved mainly by an increase of the detector mass and by a strong reduction of the background.

Gerda [43] (GERmanium Detector Array) is one of the two planned experiments devoted to the study of  $0\nu\beta\beta$  decay of  $^{76}\text{Ge}$ . The detector, which will be operated at

Experiment	Technique	Isotope	Mass [kg]	$T_{1/2}^{0\nu}$ [y]	$m_{\beta\beta}$ [eV]	Status
Gerda	HPGe	$^{76}\text{Ge}$	40	$2 \cdot 10^{26}$	$0.07 \div 0.3$	in progress
Gerda			1000	$6 \cdot 10^{27}$	$0.01 \div 0.04$	R&D
Majorana	HPGe	$^{76}\text{Ge}$	40	$2 \cdot 10^{26}$	$0.07 \div 0.3$	R&D
Majorana			1000	$6 \cdot 10^{27}$	$0.01 \div 0.04$	R&D
CUORE	bolometers	$^{130}\text{Te}$	200	$2 \cdot 10^{26}$	$0.02 \div 0.09$	in progress
EXO	TPC	$^{136}\text{Xe}$	200	$6 \cdot 10^{25}$	$0.1 \div 0.2$	in progress
EXO			1000	$2 \cdot 10^{27}$	$0.02 \div 0.03$	R&D
Super-NEMO	tracking	$^{82}\text{Se}$	200	$2 \cdot 10^{26}$	$0.05 \div 0.1$	R&D

**Table 2.2:** Experimental technique, isotope under investigation, source mass, expected half life sensitivity,  $m_{\beta\beta}$  sensitivity and current status are reported for the most sensitive next generation  $0\nu\beta\beta$  experiments. Expected sensitivities are those predicted by the authors (see references in the text).

LNGS, will be composed by bare HPGe semiconductor detectors immersed in liquid Argon. This cryogenic liquid will serve both as cooling medium for detector operation and as passive and active shield. The liquid Argon cryostat and its content will be protected from environmental radioactivity by a 3 m thick layer of highly purified water. Thanks to these shielding and to pulse shape analysis, the Gerda collaboration plan to reach a background as low as  $10^{-4}$  counts/(keV · kg · y) in the  $0\nu\beta\beta$  region. The experiment will be divided in two phases of increasing mass. In the first phase, which will start data taking in 2009, the detectors previously operated by the IGEX and Heidelberg-Moscow experiments will be redeployed. With a total detector mass of  $\sim 18$  kg enriched in  $^{76}\text{Ge}$  at 86%, the first phase of Gerda is foreseen to reach a sensitivity of  $3 \times 10^{25}$  y after one year of data taking, thus being able to confirm or reject the claim of observation in  $^{76}\text{Ge}$ . In the second phase, when the total detector mass will be of the order of 40 kg, a sensitivity of  $2 \times 10^{26}$  y (corresponding to  $m_{\beta\beta}$  in the range  $0.07 \div 0.3$  eV) will be reached in three years of data taking. Depending on the results that will be achieved in the first two phases, a third phase with a mass of the order of one ton could be supported.

MAJORANA [44, 45] will search for neutrinoless double beta decay of  $^{76}\text{Ge}$  using semiconductor detectors. The ultimate goal of this experiment is to deploy an array of segmented HPGe detectors enriched at 86% in  $^{76}\text{Ge}$  for a total mass of the order of one ton. The detectors will be installed in several separate cryostats that will be hosted in the Deep Underground Science and Engineering Laboratories (DUSEL, 4200 m w.e.) in South Dakota. The MAJORANA collaboration plan to reach background level smaller than  $10^{-3}$  counts/(keV · kg · y) in the  $0\nu\beta\beta$  region. The expected sensitivity after ten years of data taking is  $6 \times 10^{27}$  y ( $m_{\beta\beta} < 0.01 \div 0.04$  eV). A demonstrator experiment with a total mass of 60 kg will be operated in three cryostats starting from 2010. About 50% of the detectors will be enriched at 86% in  $Ge$  while the remaining part will have natural abundance and will be used for background studies. Despite its main purpose is the R&D for the ton scale detector, with a sensitivity of  $\sim 10^{26}$  y the

MAJORANA demonstrator will be able in three years to confirm or reject the  $^{76}\text{Ge}$  claim of observation.

With the same technique used in CUORICINO, the CUORE experiment [46, 47] will operate an array of 988  $\text{TeO}_2$  bolometers with a total mass of 760 kg (204 kg in  $^{130}\text{Te}$ ). In the assumption of a background level of  $10^{-2}$  counts/(keV · kg · y) a sensitivity of  $2 \times 10^{26}$  y in five years of data taking is expected ( $m_{\beta\beta} < 0.02 \div 0.1$  eV). CUORE is expected to start data taking in 2012.

SuperNEMO [48] is a proposed upgrade of NEMO 3. It is currently in the R&D phase. Main efforts are being spent to achieve a source mass of  $\sim 100$  kg of  $^{82}\text{Se}$ , but an equivalent mass of other isotopes, such as  $^{150}\text{Nd}$ , could be investigated as well. The projected sensitivity for the half life is of  $\sim 2 \times 10^{26}$  y, corresponding to an upper limit on the effective Majorana mass in the range  $0.05 \div 0.1$  eV. Compared to other experiments, SuperNEMO has the unique capability to accommodate several different  $0\nu\beta\beta$  isotopes in the detector and to change the source foils rather easily. This feature could be of great importance to check for a possible positive signal seen by other experiments.

EXO [49] (Enriched Xenon Observatory) will search for double beta decay in  $^{136}\text{Xe}$  using an approach that is rather different from other experiments [50]. The detector will consist of a time projection chamber filled with liquid Xe enriched at 80% in  $^{136}\text{Xe}$ , able to detect both ionization and scintillation light produced by the two electrons emitted in double beta decay. In addition to energy measurement and position reconstruction the EXO collaboration plan to identify the daughter ion produced in the decay ( $^{136}\text{Ba}^{++}$ ), which would reduce the background to a negligible level. Once a  $0\nu\beta\beta$  candidate event is identified, the ion is extracted from the detector and is put into a trap where it is identified by laser spectroscopy. In the first phase of the experiment a 200 kg detector prototype will be operated without ion tagging (EXO-200). The expected sensitivity in this phase will be of  $\sim 6 \times 10^{25}$  y ( $m_{\beta\beta} < 0.1 \div 0.2$  eV). With a total mass of 1 ton, the final EXO detector will reach a sensitivity of  $2 \times 10^{27}$  y ( $m_{\beta\beta} < 0.02 \div 0.03$  eV).

## 2.4 The bolometric technique

Bolometers are calorimeters operating at low temperature, in which the energy deposited by a particle is converted into phonons and is detected as a temperature variation.

Usually particle detectors are sensitive to a single energy release mechanism. For example scintillators can measure the light emitted by atomic deexcitations, while ionization detectors are sensitive to the electron-ion pairs that are produced in them. In any case the main consequence is that only a small fraction of the total released energy can be detected in these devices. Due to statistical fluctuations, this results in an intrinsic limit in the energy resolution. In contrast bolometric detectors have a much smaller intrinsic energy resolution, as almost all the released energy is eventually

converted into heat, which is the physical quantity that these devices can measure.

The first proposal to use bolometers as particle detectors dates back to more than 70 years ago [51]. Since then these devices have been used in many research fields (X-ray spectroscopy, material contamination analysis, dark matter search and others). Use of big mass bolometers for rare events physics was proposed by Fiorini and Niinikoski in 1983 [52]. Nowadays the bolometric technique represents one of the most promising approaches to the search of neutrinoless double beta decay. In the following the basic operation principles of bolometers and a description of the various components of these detectors are presented.

### 2.4.1 Working Principles

A bolometer can be essentially sketched as a two components object (see fig. 2.4): an energy absorber and a sensor that converts thermal excitations into a readable signal. The absorber must be coupled to a constant temperature bath by a weak thermal conductance, which serves as heat discharger.

Denoting by  $C$  the heat capacity of the bolometer, the temperature variation induced by an energy release  $E$  can be written as

$$\Delta T = \frac{E}{C}. \quad (2.7)$$

The accumulated heat flows then to the heat sink through the thermal link and the absorber returns to the base temperature with a time constant  $\tau = C/G$ , where  $G$  is the thermal conductance of the link:

$$\Delta T(t) = \frac{\Delta E}{C} \exp\left(-\frac{t}{\tau}\right). \quad (2.8)$$

In order to obtain a measurable temperature rise the heat capacity of the absorber must be very small: this is the main reason why bolometers need to be operated at cryogenic temperatures (of the order of  $10 \div 100$  mK).

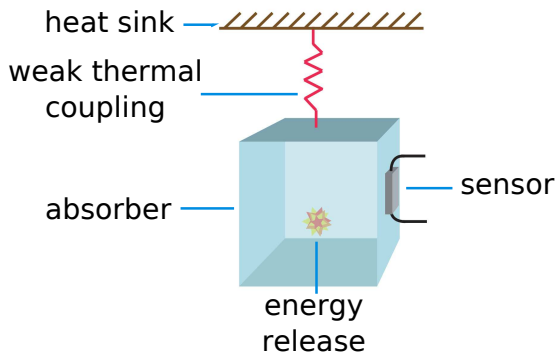


**Figure 2.4:** Schematic representation of a bolometric detector: an absorber is connected to a heat sink through a weak thermal coupling; a sensor for signal readout is attached to the absorber.

Thermal sensors used for signal readout are usually resistive elements with a steep dependence of the resistance on the temperature. Two common choices are semiconductor thermistors and superconducting films kept at the transition edge, named usually transition edge sensors (TES). TES have a rather fast time response ( $\sim \mu s$ ) but can be operated in a very narrow range of temperatures. In contrast semiconductor thermistors have a much slower time response ( $\sim ms$ ) but guarantee an adequate sensitivity in a wider range of temperatures.

### 2.4.2 Energy Absorber

The specific heat of a material at low temperature is given by the sum of two contributions, one coming from the thermal excitation of the lattice and the other related to the conduction electrons:

$$c(T) = c_r(T) + c_e(T), \quad c_r \sim T^3, \quad c_e \sim T \quad (2.9)$$

where  $c_e$  and  $c_r$  are respectively the electronic and lattice contributions. Due to the different temperature dependence, the electronic specific heat is the dominant contribution at sufficiently low temperatures. Therefore, to achieve a sufficiently low heat capacity, the energy absorber of a bolometer is usually built of dielectric and diamagnetic materials, in which the electronic contribution is not present. However this is not a severe restriction, as it is satisfied by a wide range of materials.

The lattice specific heat can be written as [53]

$$c_r(T) = \frac{12\pi^4}{5} N_a k_B \left( \frac{T}{\Theta_D} \right)^3 \quad (2.10)$$

where  $N_a$ ,  $k_B$  and  $\Theta_D$  are respectively the Avogadro number, the Boltzmann constant and the Debye temperature. Thus another parameter that can influence the choice of the material to build the energy absorber is the Debye temperature, as a bigger value of  $\Theta_D$  results in a smaller specific heat.

In a very simplified model in which all primary phonons undergo the thermalization process, an evaluation of the energy resolution can be obtained. Under this assumption the energy resolution of the detector is only limited by the thermodynamic fluctuations in the number of thermal phonons exchanged with the heat sink, which produces random fluctuations in the energy content of the absorber. The internal energy  $E$  of the absorber can be written as

$$E = C(T) \cdot T \quad (2.11)$$

or, in terms of number of phonons

$$E = N \cdot \epsilon, \quad (2.12)$$

where  $N$  is the number of phonons and  $\epsilon = k_B \cdot T$  is the average phonon energy. Assuming that the number of phonons obeys to Poisson statistics the corresponding energy fluctuations can be derived from the previous two equations:

$$\Delta E = \Delta N \cdot \epsilon = \sqrt{k_B C(T) T^2} \quad (2.13)$$

In practice a dimensionless factor  $\xi$  must be introduced in eq. (2.13) to account for the details of the experimental configuration, but this factor can be made of the order of unity with proper optimizations. It should be stressed however that at least in the case of the CUORE bolometers, thermodynamic fluctuations give a negligible contribution to the overall energy resolution. It is easy to evaluate from eq. (2.13) that for the typical values of CUORE ( $C \simeq 10^{-9} J/K$  and  $T \simeq 10 mK$ ) the thermodynamic fluctuations would result in an energy resolution of  $\sim 10 eV$ , which is well below the actual resolution of CUORE (few keV).

#### 2.4.2.1 Thermalization of deposited energy

Upon the arrival of a particle, the energy release process that eventually lead to detectable thermal phonons can occur through interactions with the lattice (nuclear channel) or with the electrons in the absorber material (electronic channel) [54].

The nuclear channel is relevant for  $\alpha$  and  $\beta$  particles, but not for electromagnetic radiation. When the thermalization process occurs via this channel there is the possibility that a fraction of the released energy remains trapped in structural defects of the absorber, thus causing a degradation in the energy resolution. The fraction of lost energy depends on the incident particle: it is negligible for electron and photons, but it can worsen the resolution to few hundreds eV for an  $\alpha$  particle with an energy of some MeV.

In the case of electronic channel the interacting particle produces electron-hole pairs in the absorber material. These charge carriers, initially produced in the vicinity of the interaction point, spread very quickly in the detector and interact to each other until a quasi-equilibrium condition is reached. Afterwards they undergo interactions with the lattice sites. In this step a large fraction of the initial energy is transferred to the lattice as vibrational excitations (phonons), but it is possible for part of the energy to leave the crystal or to be stored in stable or meta-stable states. Radiative recombinations of electron-hole pairs with the escape of the emitted photon, non radiative recombinations that take too much time compared to signal development, trapping of electrons and holes in impurity sites or lattice defects can cause a worsening of the energy resolution.

Electron-hole pairs recombinations and scattering on lattice impurities produce high energy and low momentum phonons in the optical branch, which in turn decay in a very short time (of the order of 100 ps) in longitudinal acoustic branch (LA) phonons (see fig. 2.5).

As the decay obeys to energy and momentum conservation, each phonon from the optical branch typically produces two LA phonons with opposite momentum and energy

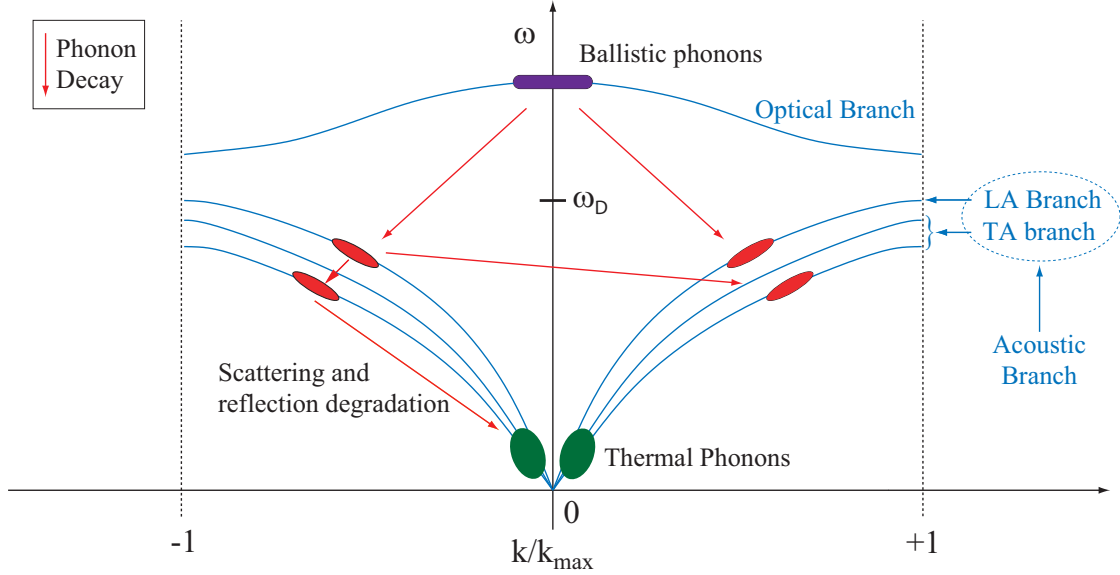


**Figure 2.5:** Mono-dimensional representation of the phonon dispersion curve.

of the order of  $k_B\Theta_D$ . However this energy is still much higher than the average phonon energy in thermal equilibrium. The thermalization proceeds then through phonon-phonon interactions, scattering on impurities and on crystal surfaces. The first mechanism is possible thanks to the anharmonicity of the lattice potential, and leads to the production of phonons in the transverse acoustic branch. Since energy degradation through phonon-phonon interactions becomes less effective as long as the phonon energy is approaching the equilibrium temperature, in the last stage of thermalization the dominant process becomes scattering on impurities and crystal surfaces.

### 2.4.3 Sensor

The phonon sensor is basically a device able to convert thermal excitations into an electrical signal. Two kind of sensors are commonly used: semiconductor thermistors (ST) and transition edge sensors (TES). In both cases the working principle is based on the steep dependence of their resistivity on the temperature, even if the physical origin for this behavior is rather different in the two devices.

Thermal sensors are characterized by their logarithmic sensitivity, given by the expression

$$A = \left| \frac{d \log R(T)}{d \log T} \right|. \quad (2.14)$$

It follows from the previous definition that

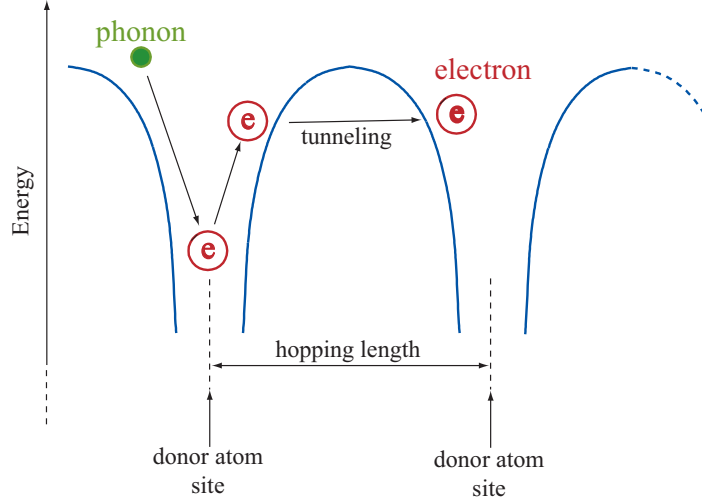


**Figure 2.6:** Representation of the hopping conduction mechanism

$$\frac{dR}{R} = A \frac{dT}{T} . \quad (2.15)$$

Typical values of  $A$  are of the order of 10 for ST and roughly 100 for TES. TES are made of semiconducting films operating close to the critical temperature. Besides having a much higher sensitivity compared to ST, these devices are intrinsically fast, and are able to detect athermal phonons. However given the physical principle on which TES are based, their sensitivity is limited to a sharp temperature range.

In the following the attention will be focused on semiconductor thermistors, as CUORICINO and CUORE use this kind of devices. ST are semiconductors containing a doping concentration slightly below the metal-insulator transition (MIT) [55].

In a doped semiconductor the conduction is dominated at sufficiently low temperature ( $\sim 10K$ ) by the migration of charge carriers between impurity sites. If the doping concentration is high enough, the wave functions of the external electrons of neighbor impurity sites overlap. In this situation the electrons are not localized and the conduction occurs without using the conduction band (hopping mechanism). As schematically depicted in fig. 2.6, this effect is due to quantum-mechanical tunneling through the potential barrier that separates the two dopant sites and is activated by phonons.

At even lower temperature, the energy of the phonons that are responsible for the conduction mechanism is low, and charge carriers migrate also on spatially far impurity sites with free energy levels that are close to the Fermi energy. In this conduction regime, called variable range hopping [56] (VRH), the concentration of minority charge carriers plays a crucial role, as it determines the density of the states in the vicinity of the Fermi level. In the VRH conduction regime the resistivity of the sensor has a steep dependence on the temperature:

$$\rho(T) = \rho_0 \exp\left(\frac{T_0}{T}\right)^\gamma, \quad (2.16)$$

where  $\rho_0$ ,  $T_0$  and  $\gamma$  are parameters that depend on the doping level. From eq. (2.16) the logarithmic sensitivity for semiconductor thermistors can be easily derived:

$$A = \gamma \left(\frac{T_0}{T}\right)^\gamma. \quad (2.17)$$

By replacing in the previous expression the typical values for  $\gamma$  and  $T_0$  (1/2 and few K respectively) it can be seen that for a sensor operating at 10 mK the logarithmic sensitivity is roughly 10.

#### 2.4.4 Detector operation

In order to convert the resistance variation into a readable voltage signal, the sensor is polarized by the simple circuit shown in fig. 2.7(a). A bias current  $I_B$  is produced by a voltage generator closed on a load resistance that is put in series with the thermistor. The load resistance  $R_L$  is set much bigger than the sensor resistance  $R(T)$ , so that the bias current can be assumed to be constant. In these conditions a voltage drop  $V(T) = I \cdot R(T)$  appears across the thermistor, causing on it a power dissipation  $P = I \cdot V$ . This in turn produces an increase of the sensor temperature and therefore its resistance is decreased. There is therefore an equilibrium condition when the power dissipated on the sensor equals the heat dissipation versus the thermal bath. Denoting by  $T_0$  the detector base temperature and by  $G$  the thermal conductance versus the bath, the equilibrium temperature of the sensor is given by the expression

$$T_{bol} = T_0 + \frac{P}{G}. \quad (2.18)$$

The dependence of the sensor resistance on the dissipated power is depicted in fig. 2.7(b).

Because of the dependence of the resistance on the bias current, the characteristic  $I - V$  curve of the detectors deviates from linearity, giving rise to the non-ohmic behavior represented in fig. 2.8(a). For small values of the bias current the temperature rise produced by power dissipation can be neglected and the  $I - V$  curve is almost linear. For bigger values of  $I_B$  the slope of the  $I - V$  curve starts to increase, until an inversion point is reached, where a further increase of the bias current causes a decrease of the sensor voltage. As represented in fig. 2.8(a) the working point of the detector can be found by the intersection of the load curve with the load line imposed by the bias circuit:  $I_B = (V_B + V_{bol})/R_L$ , where  $V_B$  is the bias voltage. It is chosen to maximize the signal amplitude or more precisely the signal to noise ratio. As represented in fig. 2.8(b) this usually correspond to a bias current at halfway between the end linear range and the inversion point.

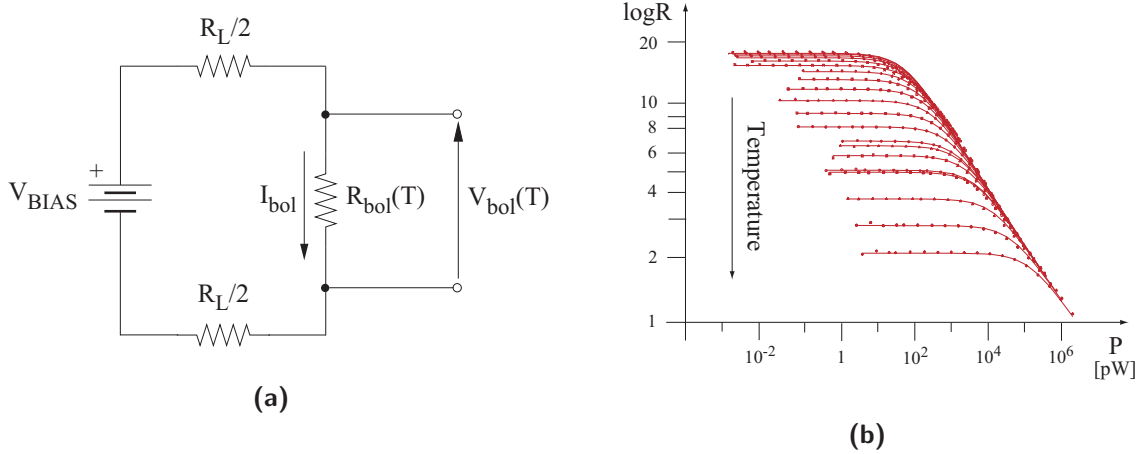


**Figure 2.7:** The left picture shows the electric scheme of the bias circuit used for thermistor readout. The right picture shows the dependence of the resistance on the power dissipation for various values of the base temperature. Curves with lower resistance at  $P=0$  correspond to higher base temperatures.

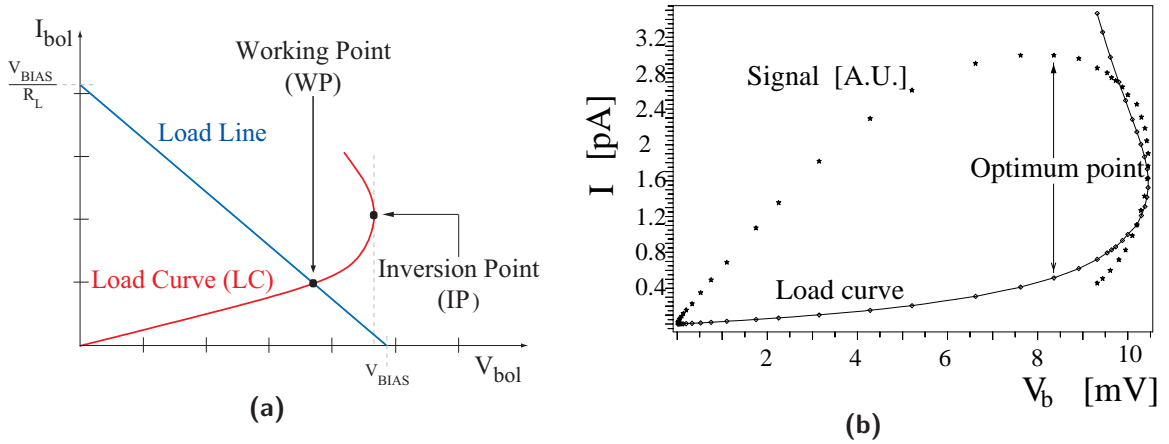


**Figure 2.8:** Load curves for semiconductor thermistors. On the left picture the working point is determined by intersection of the sensor characteristic curve with the bias circuit load line. On the right the load curve is shown together with the corresponding signal amplitude.

The signal amplitude produced by an energy release  $E$  can be estimated as follows. In static conditions the voltage over the sensor is given by

$$V_{bol} = V_B \frac{R_{bol}}{R_L + R_{bol}}, \quad (2.19)$$

where  $V_B$  is the bias voltage of the polarization circuit. The voltage pulse produced by an energy release can be written as

$$\Delta V_{bol} = V_B \frac{R_L}{(R_L + R_{bol})^2} \simeq \frac{E}{C T_{bol}} A \sqrt{P R_{bol}}, \quad (2.20)$$

where eq. (2.7) and eq. (2.14) have been used. The signal amplitude in eq. (2.20) vanishes for both  $P \rightarrow 0$  and  $P \rightarrow \infty$ , as for big power dissipation the logarithmic sensitivity and sensor resistance approach rapidly to small values.

A typical pulse produced by a particle interacting in a bolometers is represented in fig. 2.9. Using some numbers relative to the CUORE bolometers it is possible to have an idea of the magnitude of the produced signal. A typical value for the absorber heat capacity is  $C \simeq 10^{-9} J/K$  at 10 mK, thus an energy release of 1 MeV would result in a temperature rise of  $\sim 0.1 mK$ . Since the typical voltage drop across the sensor is of few mV in static conditions, the pulse height produced by the energy release of 1 MeV is given by  $\Delta V/V \sim \Delta R/R \sim A \Delta T/T \sim 100 \mu V$ .

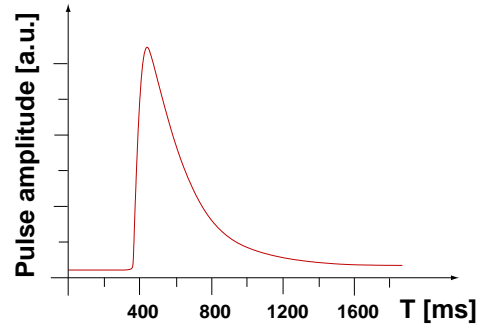


**Figure 2.9:** Typical pulse shape produced by a particle interacting in a bolometric detector.



# Chapter 3

## The CUORICINO experiment

### 3.1 Introduction

The use of bolometric detectors for the search of neutrinoless double beta decay was proposed by Fiorini in 1984 [52]. Since more than twenty years his research group has been developing cryogenic detectors of increasing mass. The successful operation of a 340 g Tellurium dioxide crystal [57] was followed by the construction of a detector array composed by 20 crystals, for a total mass of 6.8 kg of TeO<sub>2</sub> (MiDBD [58]).

A further mass increase was obtained with the recently completed CUORICINO experiment [32, 59, 60]. Operated in the Laboratori Nazionali del Gran Sasso in the years 2003-2008, CUORICINO was composed by a tower of 62 TeO<sub>2</sub> bolometers, with a total mass of  $\sim 41$  kg. The experiment was able to set a lower limit of  $3.0 \times 10^{24}$  y for the  $0\nu\beta\beta$  half life of <sup>130</sup>Te ( $m_{\beta\beta} < 0.2 \div 0.68$  eV). At present the CUORICINO results represent one of the most competitive limits for the effective Majorana mass, comparable with the ones obtained with Germanium detectors [27, 38]. Furthermore, it has been a unique test bench for the next generation CUORE experiment, which is currently in the construction phase. The excellent performance obtained with CUORICINO demonstrates the feasibility of a ton scale bolometric experiment aiming at the investigation of  $m_{\beta\beta}$  in the inverted mass hierarchy range.

In this chapter the experimental set-up, the analysis procedures, the detector performance and the physics results obtained by CUORICINO will be presented.

### 3.2 Experimental setup

CUORICINO is an array of 62 TeO<sub>2</sub> bolometers arranged in a tower of 13 floors (fig. 3.1(a)). Eleven floors are made of four  $5 \times 5 \times 5$  cm<sup>3</sup> crystals each (fig. 3.1(b)), while the two remaining floors are composed by nine  $3 \times 3 \times 6$  cm<sup>3</sup> crystals each (fig. 3.1(c)). All crystals have natural abundance of <sup>130</sup>Te (34%), apart for four  $3 \times 3 \times 6$  cm<sup>3</sup> crystals: two of them are enriched in <sup>130</sup>Te (82%) and the other two are enriched in <sup>128</sup>Te (75%).

The mass of the big crystals is of about 790 g, while the mass of the small crystals is 330 g. The total detector mass is 40.8 kg (11.8 kg in  $^{130}\text{Te}$ ).

The experiment is located in the Hall A of the Laboratori Nazionali del Gran Sasso, under a mountain that provides a  $\sim 3400$  m w.e. shield against cosmic rays. In the underground laboratories the muon flux is reduced to  $\sim 3 \times 10^{-8} \mu\text{cm}^{-2}\text{s}^{-1}$  [61] and the neutron flux to  $\sim 10^{-6} \text{n cm}^{-2} \text{s}^{-1}$  [62]. The mechanical structure of the tower is made of OFHC Copper, and the crystals are fixed to it by mean of Teflon supports. The thermal pulses are read by neutron transmutation doped (NTD) thermistors (see sec. 3.4), thermally coupled to each energy absorber. Since thermal drifts would induce variations in the response of the detectors, the tower is maintained at a constant temperature by a feedback stabilization circuit, fed by the signal of a thermometer that is attached on the mechanical structure of the detector [63]. Fine gain drift corrections are applied offline by exploiting the fixed energy thermal pulses that are injected every few minutes in the crystals [64]. These stabilization signals are generated by dissipating an electrical pulse of fixed energy on a Si resistor attached to each energy absorber. They have a time duration much shorter than the typical thermal response of the detector, and the produced signals have a shape that is almost indistinguishable from the ones produced by particle interactions. These signals, usually called heater pulses, are flagged by the data acquisition system and are used offline to correct gain fluctuations induced by temperature drifts.

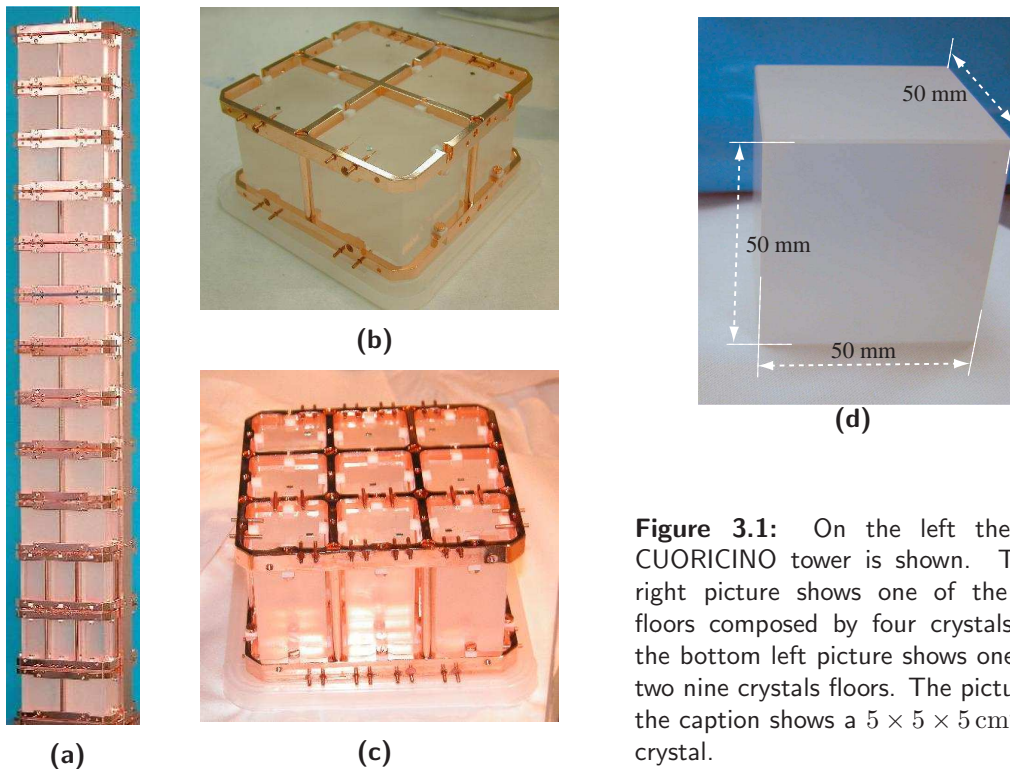


**Figure 3.1:** On the left the entire CUORICINO tower is shown. The top right picture shows one of the eleven floors composed by four crystals, while the bottom left picture shows one of the two nine crystals floors. The picture over the caption shows a  $5 \times 5 \times 5 \text{ cm}^3$   $\text{TeO}_2$  crystal.

About once per month a few days energy calibration is performed by inserting  $^{232}\text{Th}$  sources between the cryostat and the external lead shields. Typical energy spectra obtained in calibration measurements are reported in fig. 3.2.

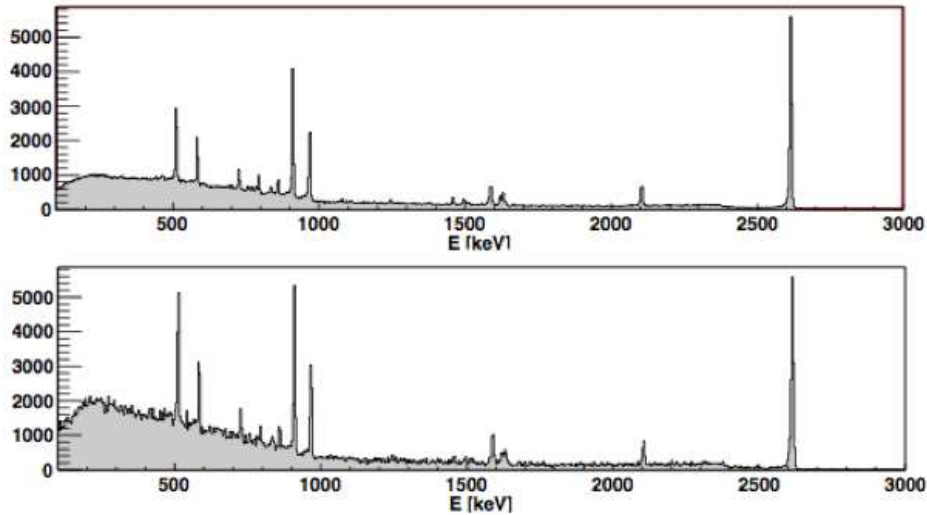


**Figure 3.2:** Typical energy spectra obtained in a few days calibration in CUORICINO. The top figure represents the spectrum for the  $5 \times 5 \times 5 \text{ cm}^3$  crystals while the bottom one is for the  $3 \times 3 \times 6 \text{ cm}^3$  crystals.

All the materials used to construct the CUORICINO tower were selected after rigorous radioactivity checks and dedicated procedures were developed to clean them. The crystals were grown using previously tested low radioactivity powders by the Shanghai Institute of Ceramics (SICCAS) and were shipped to Italy by boat and stored underground to minimize activation by cosmic ray interactions. The cleaning procedures, as well as the detector assembly, were performed in a  $N_2$  atmosphere using glove boxes to minimize surface recontaminations.

The CUORICINO tower is hosted in a dilution refrigerator that allows to operate the detectors at a temperature of  $\sim 8 \text{ mK}$  (see fig. 3.3). To avoid heating due to vibrations the tower is mechanically decoupled from the cryogenic apparatus using a stainless steel spring.

Several shields are used to minimize the background. The tower is surrounded by a 1.2 cm low activity Roman lead layer ( $^{210}\text{Pb}$  activity  $< 4 \text{ mBq/Kg}$  [65]) maintained at 600 mK to avoid the radioactive background coming from the cryostat radiation shields. The thickness of the Roman lead layer is increased to 10 cm on top of the detector in order to protect it from contaminations in the dilution unit. The cryostat is surrounded externally by two 10 cm thick lead shields. The internal one has an activity of  $16 \pm 4 \text{ Bq/kg}$  in  $^{210}\text{Pb}$  while the external one is made of standard commercial lead. The background due to environmental neutrons is reduced by a 10 cm thick borated polyethylene shield. The cryostat is also surrounded by a box continuously flushed

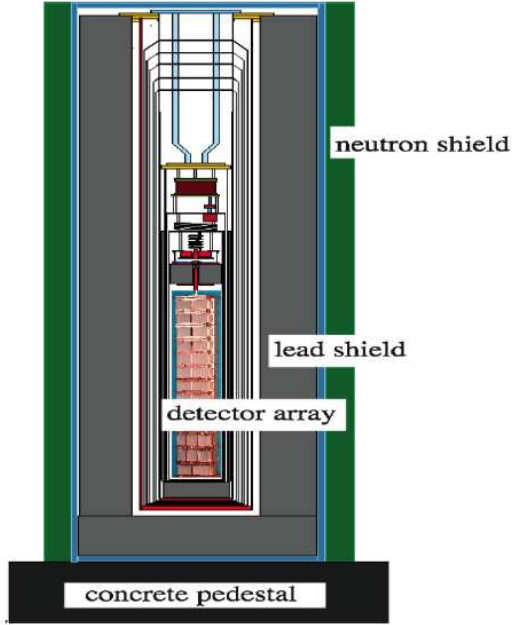
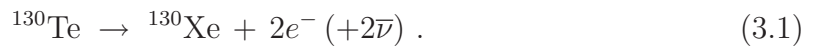


**Figure 3.3:** Sketch of the CUORICINO apparatus showing the tower hanging from the mixing chamber of the dilution refrigerator and the detector shieldings.

with clean  $N_2$  to reduce Radon contaminations, and it is enclosed in a Faraday cage to avoid electromagnetic interference.

### 3.3 Energy absorber: the choice of $\text{TeO}_2$

The use of  $\text{TeO}_2$  crystals as absorbers for the bolometric search of neutrinoless double beta decay has undergone exhaustive and convincing validations in CUORICINO and its predecessor experiments. It is motivated by various reasons, some of them related to the  $0\nu\beta\beta$  candidate isotope ( $^{130}\text{Te}$ ) and others related to the cryogenic properties of this material. Double beta decay of  $^{130}\text{Te}$  occurs through the transition



The most striking feature of  $^{130}\text{Te}$  compared to other  $0\nu\beta\beta$  isotopes is the high natural abundance (see fig. 3.4). In contrast to other materials, which usually need to be enriched to obtain a sufficient sensitivity in a reasonable detector mass, the abundance of  $^{130}\text{Te}$  allows to build an experiment with natural Tellurium. This is a big advantage both in terms of costs and material cleanliness, as enrichment procedures often introduce radioactive contaminations.

In addition  $^{130}\text{Te}$  has a reasonably high transition energy ( $Q_{\beta\beta} = 2530.3 \pm 2.0 \text{ keV}$  [66]). This corresponds to an high phase space factor ( $G_{0\nu} \sim Q^5$ ) and a low contribution to the background from  $2\nu\beta\beta$  decay (the fraction of  $2\nu\beta\beta$  counts in the region of the  $0\nu\beta\beta$  peak scales as  $1/Q^5$ ). It has been discussed in sec. 2.2 that experiments using isotopes with Q-values above 2615 keV are affected by a much lower radioactivity background.

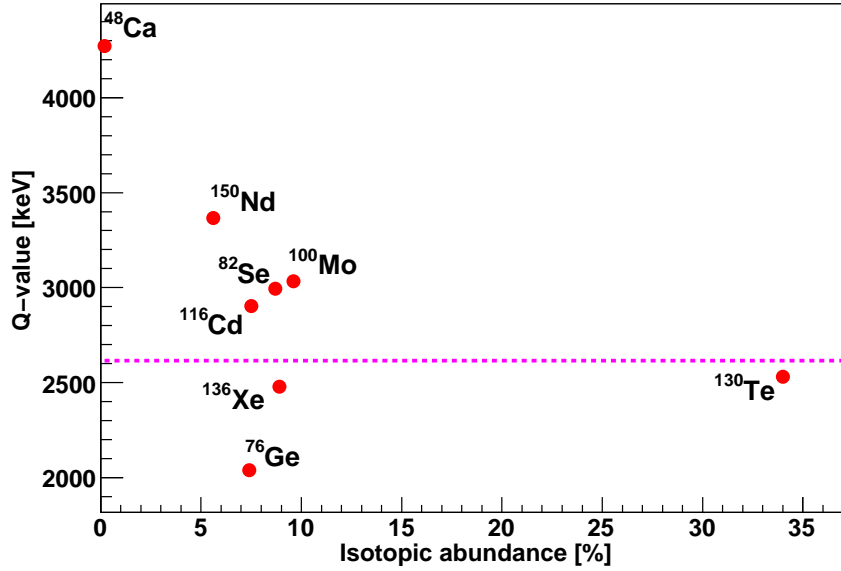


**Figure 3.4:** Graphical representation of natural abundances and Q-values for several commonly used  $0\nu\beta\beta$  isotopes. The dashed line at 2615 keV represents the highest energy natural radioactivity  $\gamma$ . Isotopes with Q-values above this energy benefit of a much lower background.

Even if  $^{130}\text{Te}$  does not satisfy this condition, its Q-value is in a quite favorable position, as it lies between the Compton edge and the photoelectric peak from  $^{208}\text{Tl}$ , in an energy window characterized by low natural radioactivity.

The possibility to use pure Te crystals as bolometer absorbers was taken into account, but it was ruled out mainly because of the poor mechanical properties of this material at low temperature. Stress caused by the differential thermal contractions occurring between the various materials constituting the detector, as well as the effect of repeated thermal cycles revealed to produce excessive damage on pure Te crystals. However this does not have a great impact in terms of detector sensitivity, as the Tellurium mass content of  $\text{TeO}_2$  is still quite high (80%). Moreover  $\text{TeO}_2$  has a higher Debye temperature compared to pure Te: this implies lower specific heat and thus higher thermal pulses.

### 3.4 The thermal sensor

In CUORICINO the thermal pulses produced in the absorber are converted into electrical signals by mean of neutron transmutation doped (NTD) Germanium thermistors operating in the VRH regime. As already explained in sec. 2.4.3 the resistance of these devices has a strong dependence on the temperature:

$$R(T) = R_0 \exp\left(\frac{T_0}{T}\right)^\gamma. \quad (3.2)$$

Typical values for  $R_0$  and  $T_0$  are  $2\ \Omega$  and  $3\ K$  respectively, while  $\gamma = 1/2$ . In order to obtain uniform values for the working resistance and for the logarithmic sensitivity a great control is needed on the uniformity and the concentrations of the dopants. This is obtained by exposing Ge wafers to a neutron flux from a nuclear reactor, where the following reactions occur:

$$\begin{cases} {}^{70}\text{Ge}(a.i. = 21\%) + n \rightarrow {}^{71}\text{Ge} + \gamma & (\sigma_T = 3.43 \pm 0.17b, \sigma_R = 1.5b) \\ {}^{71}\text{Ge} + e^- \rightarrow {}^{71}\text{Ga} + \nu_e & (\tau_{1/2} = 11.4d) \end{cases}$$

$$\begin{cases} {}^{74}\text{Ge}(a.i. = 36\%) + n \rightarrow {}^{75}\text{Ge} + \gamma & (\sigma_T = 0.51 \pm 0.08b, \sigma_R = 1 \pm 0.2b) \\ {}^{75}\text{Ge} \rightarrow {}^{75}\text{As} + e^- + \bar{\nu}_e & (\tau_{1/2} = 83min) \end{cases}$$

$$\begin{cases} {}^{76}\text{Ge}(a.i. = 7.4\%) + n \rightarrow {}^{77}\text{Ge} + \gamma & (\sigma = 0.160 \pm 0.0014b, \sigma_R = 2.0 \pm 0.35b) \\ {}^{77}\text{Ge} \rightarrow {}^{77}\text{As} + e^- + \bar{\nu}_e & (\tau_{1/2} = 11.3h) \\ {}^{77}\text{As} \rightarrow {}^{77}\text{Se} + e^- + \bar{\nu}_e & (\tau_{1/2} = 38.8h) \end{cases} \quad (3.3)$$

In eq. (3.3)  $\sigma_T$  and  $\sigma_R$  refer to the thermal and resonance neutron capture cross sections respectively. The first reaction produces an acceptor ( ${}^{71}\text{Ga}$ ), the second one produces a donor ( ${}^{75}\text{As}$ ) while the last one produces a double donor ( ${}^{77}\text{Se}$ ). Natural abundances of Germanium are such that this doping technique allows to obtain the right net dopant concentration (given by the difference between the acceptor and donor concentrations), which is a key quantity in the determination of the sensor performances.

To obtain the correct doping concentrations it is important to have a stable neutron flux and the neutrons energy distribution must be kept under control: an excess of fast neutrons ( $E > 5\ \text{MeV}$ ) would produce radioactive contaminants such as  ${}^3\text{H}$ ,  ${}^{65}\text{Zn}$  or  ${}^{68}\text{Ge}$  that would result in an increase of the background.

In order to measure the performance of the doped thermistors it is necessary to wait for the decay of the activation product  ${}^{71}\text{Ge}$  ( $\tau = 11.4d$ ). Given the high neutron flux to which the Germanium wafers are exposed it is necessary to wait at least few months before the sensor can undergo a thermal performance test. Therefore, to have at least a rapid indication of the doping concentrations, Germanium wafers are exposed to the neutron flux together with several metal foils. By measuring the concentration of the long lived isotopes produced in these metal foils after the neutron irradiation it is possible to extract the neutron fluxes and thus the corresponding doping levels in the Ge wafers.

After the decay of  ${}^{71}\text{Ge}$  the wafers are treated with heat to repair the crystal structure and are cut in  $3 \times 3 \times 1\ \text{mm}^3$  strips. The characteristic parameters of each thermistor are then measured at cryogenic temperatures as described in [67].

### 3.5 The single module

The CUORICINO detector has a modular structure, where the basic element is represented by a single floor (see fig. 3.1). The design of the single module must satisfy stringent requirements concerning mechanical properties, thermal performances and radioactivity constraints. Thermal coupling between the crystals and the heat sink, as well as the ones with the NTD sensors, must guarantee a good performance of the detector. At the same time the geometry of the various parts of the single module must be properly designed, preventing the differential thermal contractions from breaking the crystals or leaving them too loose. All these requirements have to be met by using only those materials that were measured to have low enough radioactive contaminations.

A detail of the CUORICINO single module is shown in fig. 3.5. It is composed by four  $5 \times 5 \times 5 \text{ cm}^3$  (or nine  $3 \times 3 \times 6 \text{ cm}^3$ ) crystals enclosed in a pair of OFHC copper frames which serve both as mechanical supports and thermal bath for the detectors. The two frames are connected to each other by four small columns, also made of copper.

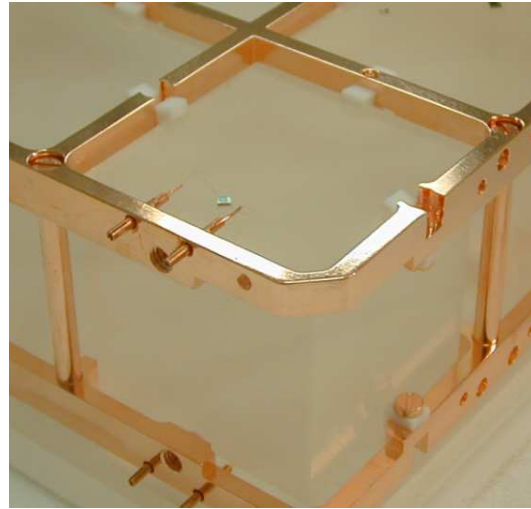


**Figure 3.5:** Detail of the CUORICINO single module. The crystal is held by OFHC copper frames which also represent the thermal bath for the detectors. In the picture the Teflon holders and the NTD sensor are also visible.

The crystals are connected to the copper frames by small Teflon supports that represent the weak thermal conductance versus the heat sink and compensate the different thermal contractions of  $\text{TeO}_2$  and copper.

The NTD sensors are attached to the crystals using Araldit Rapid, Ciba Geigy epoxy glue. Since a flat glue deposition would cause the sensor to detach from the crystal surface because of differential thermal contractions, the glue is deposited in nine separate spots, with a diameter of 0.7 mm each. The thermal conductance of the glue spots was measured experimentally and the phenomenological relation revealed to be  $G \simeq 2.6 \times 10^{-4} T^3 \text{ [W/K/spot]}$  [68], where T is in K. The same gluing technique is used to apply on each detector the Si resistor used to feed the crystal with heater pulses. Electrical connections for both the NTD sensor and the Si resistor are made with two  $50 \mu\text{m}$  diameter gold wires, bonded to metalized surface of the two chips.

The wires are crimped on the opposite side into copper pins that pass through the mechanical structure of the single module (see fig. 3.5).

### 3.6 Signal readout

The electrical connection of the bolometric signals from 10 mK to room temperature is divided in two parts. After coming out from the single module, the signal runs along the CUORICINO tower over a twisted pair of low radioactivity Constantan wires, until it reaches the mixing chamber. From this point on, the signal is delivered over a pair of twisted coaxial cables made of a core of superconductive NbTi alloy surrounded by a CuNi low resistance alloy. Passing through several thermalization stages these wires reach the front end electronics boards that are located at room temperature.

The CUORICINO readout chain is designed keeping in mind the characteristics of the signals to be recorded. First of all it should give a negligible noise contribution in the frequency band of the detector signal ( $\sim 1$  Hz to few tens of Hz); this is true mainly for the first part of the readout chain (biasing circuit and preamplifier), as the signals to be read have small amplitudes at this stage (typical voltage signals across the thermistors have an amplitude of  $\sim 100 \mu\text{V}$ ). In addition It should be able to account for the wide spread in the dynamic response of different detectors; compared to other kind of detectors bolometers are particularly demanding in this regard. Signals must be acquired in DC, as the amplitude of thermal pulses depends not only on the amount of released energy, but also on the base temperature of the detectors; as a consequence the voltage drift introduced by the readout system must be negligible over long time measurements. Moreover, since bolometers are much sensitive to vibrational noise, the design of the readout system should provide remote programmability to avoid mechanical interventions in the vicinity of the bolometers during data taking.

The analog part of the readout system performs mainly three operations: thermistor biasing, signal amplification and signal filtering. All the programmable parameters for the front end electronics and for the biasing circuit can be selected remotely using a I2C bus, allowing a channel by channel detector optimization.

The basic concepts of the biasing circuit are explained in sec. 2.4.4. Thermistor biasing is accomplished by applying a programmable voltage across a series combination of the thermistor and two load resistors, as shown in fig. 3.6. The load resistors must be big compared to the sensor resistance, so that the bias current can be assumed to be constant even in presence of signals. Since the typical sensor resistance is of the order of 100 M $\Omega$  at 10 mK, the load resistor are chosen to be 27 G $\Omega$  each.

In order to account for the spread in the static resistance of different detectors a programmable offset voltage is added to the thermistor signals before the amplification stage. This offset allows to obtain a signal, at the end of the readout chain, that is suitable for the range of the ADC boards (0÷10V).

The amplification stage consist of a first low noise differential voltage sensitive

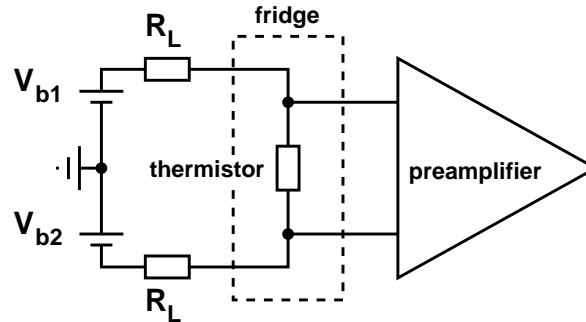


**Figure 3.6:** Schematic of the thermistor biasing system. The dashed box represent the part of the detector that is located at low temperature.

preamplifier with fixed gain ( $G=218$ ) followed by a second programmable gain amplifier [69]. The total gain of the readout chain can be set to values in the range  $448 \div 10000$  V/V. The differential configuration has been adopted to minimize cross talk and microphonic noise coming from the wires inside the cryostat, where the signal amplitude is still of the order of  $\sim 100 \mu\text{V}$ . In order to investigate the contribution of these noise sources to the overall energy resolution, for several readout channels the preamplifier stage, as well as the load resistors, were housed inside the cryostat, at a temperature of  $\sim 110$  K. For channels using this configuration the length of the wires running from the NTD sensors to the preamplifier was reduced from 5 m to 1 m.

The noise reduction provided by cold electronics does not improve the detector sensitivity for double beta decay search, since other factors dominate the resolution at high energy. The noise coming from readout chain over the signal bandwidth is dominated by the Johnson noise of the load resistors and from the preamplifier stage. The total contribution is of  $\sim 90$  nV<sub>FWHM</sub>, which is negligible compared to the  $\sim 1$   $\mu\text{V}_{FWHM}$  observed on the best performing bolometers at 2.5 MeV. However a noise reduction could be important for the study low energy part of the spectrum, where a better energy resolution is achieved. This could be useful for example for dark matter search.

After the amplification stage the signal goes through an anti aliasing 6 poles Bessel low-pass filter with an attenuation of 120 dB/decade and programmable cutoff frequency (in the range 8-20 Hz). Signals are then acquired by commercial 16 bit digitizing boards operating in the range  $0 \div 10$  V. Given the low event rate and the small bandwidth of the signals it was possible to implement a software trigger algorithm. Signals are shaped by a digital filter to remove the DC component and are saved if their amplitude exceeds the threshold for a given amount of time. Trigger parameters can be set independently for different channels. When a trigger is found, the signal is recorded in a window of  $\sim 4$  s, with a sampling period of 8 ms (125 Hz). In order to have an estimate of the detector temperature at the time of the pulse, about one second of detector baseline preceding the trigger is recorded too. Selected events are then written to disk for offline processing.

### 3.7 First level analysis

The CUORICINO data analysis proceeds through two steps. First level analysis aims at determining the energy and several pulse shape parameters associated to each raw pulse waveform recorded by the data acquisition system. Starting from these quantities, second level analysis allows to extract the physical informations that are relevant for the scientific goals of the CUORICINO experiment. In this section the first level analysis procedures will be discussed.

The first operation to be performed in offline analysis is the association of an amplitude to each recorded waveform. Since thermal pulses are superimposed to stochastic noise, a simple maximum-minimum algorithm would not give optimal results. Instead the optimum filter (OF) technique is used. Based on the approach described in [70], this algorithm has proven to provide the best estimate of the pulse amplitude and, as a consequence, the best energy resolution. The basic concept is to build a filter that, when applied to the raw waveform, produces a pulse as output with the best signal to noise ratio. The filtered pulse is then used to evaluate signal amplitude. It can be proven that in the frequency domain the OF transfer function  $\mathcal{H}(\omega)$  is given by

$$\mathcal{H}(\omega) = K \frac{\mathcal{S}^*(\omega)}{\mathcal{N}(\omega)} e^{-j\omega t_M}, \quad (3.4)$$

where  $\mathcal{S}(\omega)$  is the Fourier transform of the ideal thermal signal (without noise),  $\mathcal{N}(\omega)$  is the noise power spectrum,  $t_M$  is the arrival time of the pulse and  $K$  is an arbitrary constant that is fixed when the pulse amplitudes are converted into the corresponding energy values. The role of the optimum filter is to weight the frequency components of the signal in order to suppress those frequencies that are more affected by noise. It can be seen from eq. (3.4) that, in order to build the filter, the ideal shape of the pulse and the noise power spectrum must be known for each bolometer. The ideal detector response is usually estimated by averaging a large number of recorded raw pulses, so that the noise associated to each of them averages to zero.  $\mathcal{N}(\omega)$  is obtained by acquiring many detector baselines in absence of thermal pulses and averaging the corresponding noise power spectra. In addition to the best estimate of the pulse amplitude, several pulse shape parameters can be obtained from the comparison of the real and ideal filtered pulses. These parameters are used to reject spurious signals produced by microphonic and electronic noise.

After that the pulse amplitude has been evaluated using the OF technique, gain instability corrections are applied to data. It has been previously discussed that because of the dependence of the detector response on the working temperature, the same amount of released energy can produce thermal pulses of different amplitudes. Gain instabilities are corrected exploiting the fixed energy reference thermal pulses produced every few minutes on each bolometer by mean of the Si heater resistor attached on them (see sec. 3.2). A typical trend for the reference pulse amplitude as a function of the detector baseline (which is in turn a function of the detector base temperature) before

and after gain instability corrections is shown in fig. 3.7.

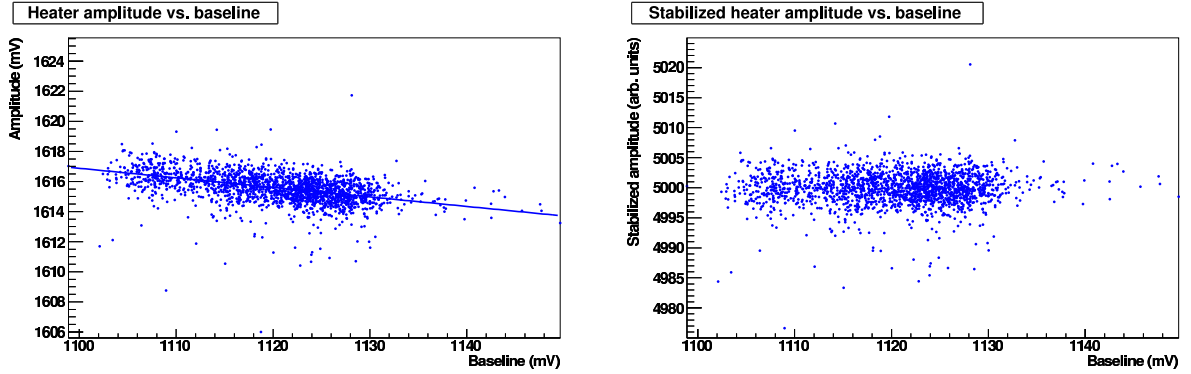


**Figure 3.7:** Heater pulse amplitude as a function of the detector baseline before (left) and after (right) gain instability corrections. Stabilized heater amplitudes are usually reported to the nominal amplitude of 5000. This arbitrary scaling factor is eliminated when pulse amplitudes are converted into energy values.

The relation  $\Delta V(V_B)$  between the heater pulse amplitude and the baseline value is found by a fit on the left plot in fig. 3.7. The gain correction factor is then obtained as

$$\alpha(V_B) = \frac{\Delta V^{ref}}{\Delta V(V_B)} \quad (3.5)$$

where  $\Delta V^{ref} \equiv \Delta V(V_B^{ref})$  and  $V_B^{ref}$  can be arbitrarily chosen. Assuming that the gain correction factor  $\alpha(V_B)$  is the same for all energies, it can be used to adjust the amplitudes of all pulses. The effect of gain instability corrections is visible in fig. 3.8.

The final step of first level analysis is the conversion of the stabilized OF amplitudes into the corresponding energy values. As explained in sec. 3.2 detector energy calibration is performed about once per month by inserting a  $^{232}\text{Th}$  source in the vicinity of the detector. Pulse amplitude spectra from calibration measurements show several  $\gamma$  peaks that are not visible in standard background measurements, because of the low radioactivity content of the detector materials. A polynomial fit is applied to these peaks to obtain a  $E(\Delta V)$  conversion curve that is then applied to background measurements to obtain the corresponding energy spectra. Background measurements between two consecutive calibrations are usually grouped into a data set. A check is performed to ensure that the energy conversion curves  $E(\Delta V)$  obtained from the two calibrations performed before and after each data set are compatible with each other.

### 3.8 CUORICINO background and $0\nu\beta\beta$ results

Second level analysis can proceed through different steps, depending on the physics goal of the analysis being performed. One could search for events contained in a single crystal, using all other detectors as active veto, or could search for coincident events in

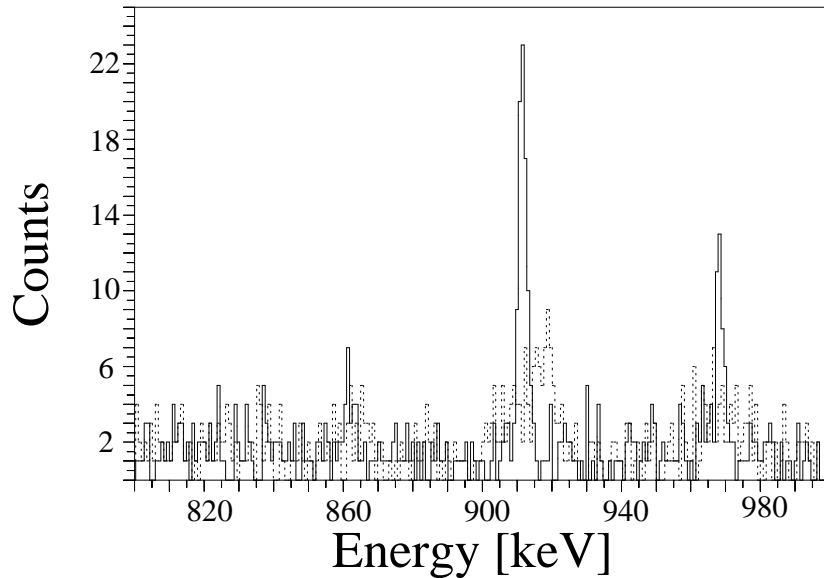


**Figure 3.8:** Comparison between energy spectra before (dashed line) and after (continuous line) gain instability corrections. The two visible lines in the stabilized spectrum are due to  $\gamma$ s from the  $^{232}\text{Th}$  calibration source.

neighbor crystals; relative intensities of different  $\gamma$  peaks, or continuum counting rate in a given energy window can be studied to characterize different background sources. Here the attention will be focused on the search of neutrinoless double beta decay and the study of the background in the energy range where the signal is expected.

### 3.8.1 Data taking and detector performance

CUORICINO data taking started in march 2003. Several wiring connection broke during the detector cool down procedure, so that only signals from 32 over 44  $5 \times 5 \times 5 \text{ cm}^3$  crystals and 17 over 18  $3 \times 3 \times 6 \text{ cm}^3$  crystals could be acquired. Since the active mass was anyway quite large ( $\sim 30 \text{ kg}$  of  $\text{TeO}_2$ ) and the detector performance was satisfactory, data taking continued for few months. In November 2003 the tower was warmed up at room temperature to perform maintenance operations and to recover lost connections. Data taking restarted in may 2004 with the full operation of all detectors. This interruption set a marking point dividing the data taking in Run1 (prior to November 2003) and Run2 (from April 2004 to June 2008).

The performance of the detectors in the two runs was excellent. The average energy resolution was 7 keV for the big crystals and 9 keV for the small ones. The best detectors had a resolution of 5 keV. Energy resolution was evaluated as the FWHM of the 2615 keV  $^{208}\text{Tl}$  gamma peak observed in calibration measurements. Similar energy resolution was obtained from the  $^{208}\text{Tl}$  line that was visible also in background measurements summed over long time periods. Excluding the interruptions for the

maintenance of the cryogenic apparatus, the live time of the experiment was evaluated to be  $\sim 70\%$ .

### 3.8.2 Background analysis

The background observed by CUORICINO can be grouped in two categories, depending on whether it comes from outside the detector (external background) or from the detector itself and the passive materials that surround it (internal background).

External background is produced by neutrons, muons, and natural radioactivity in the underground laboratories. It can be reduced to a negligible level by proper detector shielding, as already discussed in sec. 3.2.

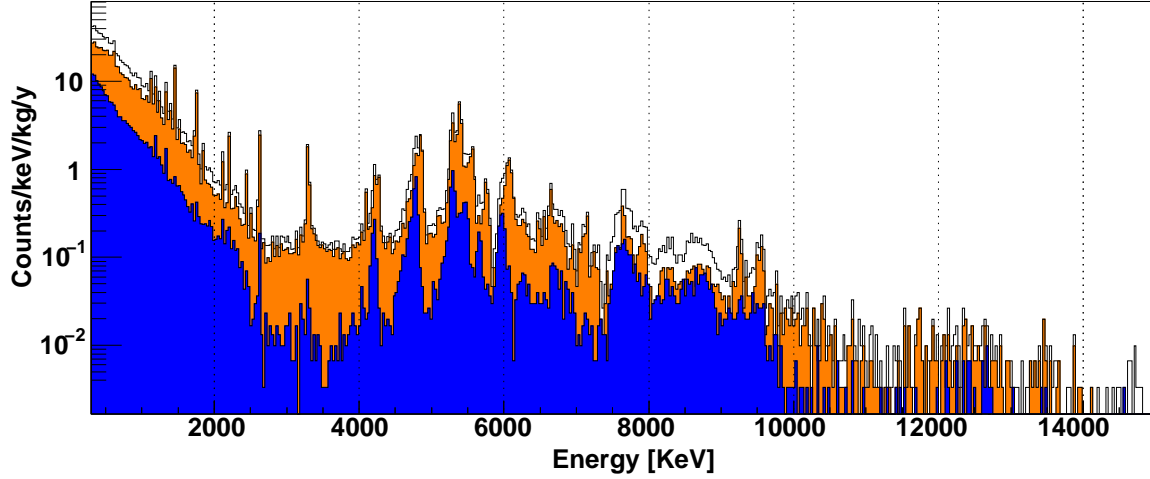
Internal background comes from the radioactive contaminations in the cryostat radiation shields, the mechanical structure of the tower and the crystals themselves. Apart for the most external cryostat radiation shields, from which the crystals are protected by a low radioactivity Roman lead layer (see sec. 3.2), there is no way to protect the detector from the internal background sources. The only available solution is to eliminate them by proper material selection and cleaning. As will be discussed in chapter 5, this is one of the guidelines of the R&D activity for the CUORE experiment.

Figure 3.9 shows the background measured by the  $5 \times 5 \times 5 \text{ cm}^3$  crystals in CUORICINO. It was obtained by summing the single crystal energy spectra over the whole data taking of the experiment. The three histograms represent the single hit, double hit and total energy spectra. Single hit spectrum was obtained using the detector array as a veto, thus selecting events in which only one crystal was hit within a coincidence time window of  $\sim 100 \text{ ms}$ . Double hit spectrum was obtained from the requirement that two crystals were hit in the same coincidence time window.

The  $0\nu\beta\beta$  detection efficiency has been evaluated using Monte Carlo simulations: in 86% of the cases the two emitted electrons are fully contained in the crystal where the decay occur. Therefore the  $0\nu\beta\beta$  signal should appear as a peak at  $\sim 2530 \text{ keV}$  in the single hit spectrum. Thus, the capability of operating the detectors in anti-coincidence allows to reduce the background. Due to the way in which the crystals are arranged, this reduction is not much effective for CUORICINO, but it will play a fundamental role in the tight-packed structure of CUORE. Even in CUORICINO, by studying the differences between coincidence and anti-coincidence spectra it is possible to extract important informations concerning the nature and the location of background sources.

Source	$^{208}\text{Tl}$	$0\nu\beta\beta$	3-4 MeV
$\text{TeO}_2$ $^{238}\text{U}$ and $^{232}\text{Th}$ surf. cont.	-	$10 \pm 5\%$	$20 \pm 10\%$
$\text{Cu}$ $^{238}\text{U}$ and $^{232}\text{Th}$ surf. cont.	15%	$50 \pm 20\%$	$80 \pm 10\%$
$^{232}\text{Th}$ cont. in cryostat Cu shields	85%	$30 \pm 10\%$	-

**Table 3.1:** Main contributions to the CUORICINO background. The values refer to the background in the  $0\nu\beta\beta$  region, in the  $^{208}\text{Tl}$  peak and in the region between 3 and 4 MeV.



**Figure 3.9:** CUORICINO background. The black histogram represents the total energy spectrum; the orange filled histogram is the anti-coincidence spectrum (a single hit in a coincidence window of  $\sim 100$  ms) and the blue filled histogram is the double hit spectrum (two events occurred in the same  $\sim 100$  ms time window).

CUORICINO has a background of 0.18 counts/(keV·kg·y) in the  $0\nu\beta\beta$  region, the main contributions coming from the sources reported in tab. 3.1. As shown in fig. 3.10 the background differs by about 30% on the two side of the 2615 keV  $^{208}\text{Tl}$  line. This line, from the  $^{232}\text{Th}$  decay chain, is the highest  $\gamma$  line produced by environmental contaminations and is the only possible  $\gamma$  contribution (through Compton events) to the  $0\nu\beta\beta$  background. The other two peaks appearing in the spectrum shown in fig. 3.10 are the 2448 keV line from  $^{214}\text{Bi}$ , and the 2505 keV sum line produced by the interaction in the same crystal of the two  $\gamma$ s emitted in  $^{60}\text{Co}$   $\beta$  decay. Given the good energy resolution, events from these two peaks produce a negligible contribution to the  $0\nu\beta\beta$  background.

By comparing the intensities of the  $^{208}\text{Tl}$  gamma line with other lower energy  $\gamma$ s from the  $^{232}\text{Th}$  chain it is possible to evince that the contamination is located relatively far from the detector, probably in some external cryostat thermal shield. Based on this guess on the source position, the contribution from the  $^{208}\text{Tl}$  line to the  $0\nu\beta\beta$  background reported in tab. 3.1 was extrapolated using Monte Carlo simulations.

The background counts measured by CUORICINO on the right hand side of the  $^{208}\text{Tl}$  peak are produced mainly by degraded  $\alpha$  particles from U and Th contaminations that are presumably located on the crystals and on the passive materials surrounding them. They produce a continuum in the energy spectrum that extends below the  $^{208}\text{Tl}$  peak and thus contributes to the background in the  $0\nu\beta\beta$  region. As shown in fig. 3.11,  $\alpha$  peaks can be easily identified in the CUORICINO energy spectrum. From the study of their position and shape it is possible to extract informations on the location of the radioactive contaminants (see fig. 3.12).

If the source is located within the crystals, both the  $\alpha$  particle and the associated

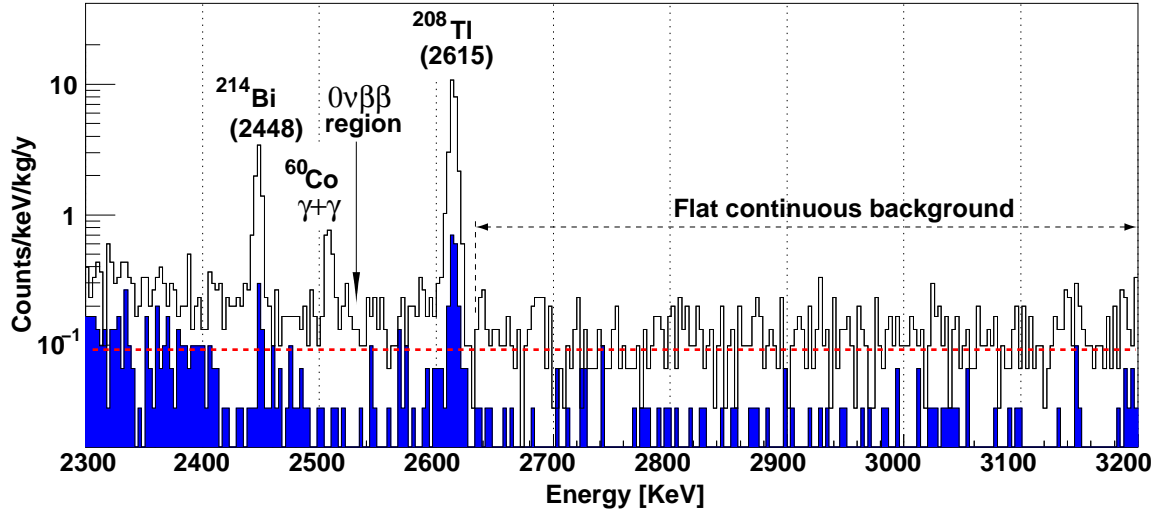


**Figure 3.10:** CUORICINO background in the  $0\nu\beta\beta$  region. The black histogram is the single hit spectrum, while the blue filled histogram is the double hit spectrum. The  $0\nu\beta\beta$  signal should appear as a peak at 2530 keV.

nuclear recoil release their energy inside the crystal and a sharp Gaussian peak is produced in the spectrum. In case the contamination is located on a very thin layer in the vicinity of the surface of the crystals or the passive materials, the  $\alpha$  particle can escape retaining almost all its energy and can hit another crystal. Even in this case a Gaussian peak is produced, whose position is given by the energy of the  $\alpha$  particle only (no recoil). If instead the surface contaminations are deep enough, even a part of the  $\alpha$  energy is released in the material where the radioactive decay occurs. In case it is a crystal, a peak with an asymmetric long energy tail is produced. If instead the decay occurs on a passive material, only a flat continuum will appear in the energy spectrum. Besides the analysis of spectral shapes, further informations on the location of the contaminants can be extracted from the study of coincident events. In case they are located on crystal surfaces, there is a non negligible probability that the escaped  $\alpha$  particle is detected by a neighbor crystal. This would result in two detectors recording a signal at the same time and whose sum energy is equal to the total transition energy of the decay ( $\alpha + \text{recoil}$ ). Obviously this feature is not present if the contaminant is located in the passive materials, as the fraction of energy that has been released in them cannot be detected. Examples of the characteristic features resulting from the different location of the contamination are shown in fig. 3.12.

In CUORICINO most of the  $\alpha$  peaks in the region above 4 MeV are produced by U and Th surface contamination of the crystals: these peaks are visible in both single and double hit spectra, and they have a large low energy tail that excludes the possibility of internal contaminations. There are however few exceptions:

- the  $\alpha$  peak at 3200 keV is produced by an internal  $^{190}\text{Pt}$  contamination of the

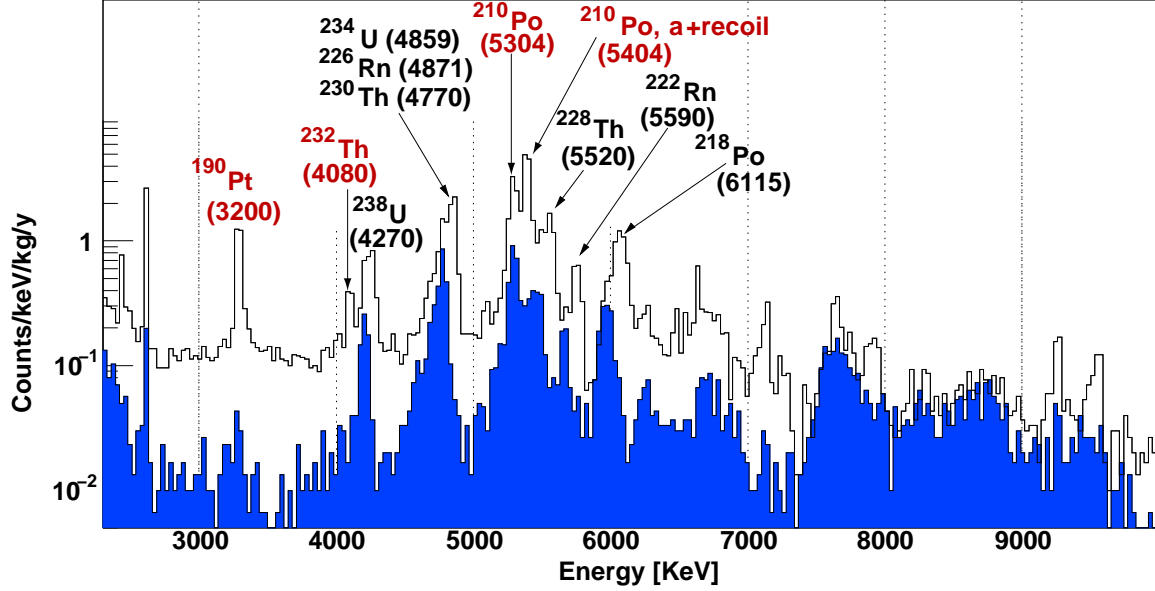


**Figure 3.11:** CUORICINO background in the  $\alpha$  region: single hit (black) and double hit spectrum (blue filled).

crystals: the shape of the peak is Gaussian and no peak appears in the coincidence spectrum. The contamination is probably due to inclusions of fragments of the Pt crucible used in the crystal growth procedure;

- the  $\alpha$  peak at 4080 keV, growing on the low energy tail of the 4270 peak, is attributed to a bulk contamination in Th, as was demonstrated by dedicated tests aiming at the reduction of the crystal surface contaminations;
- the  $\alpha$  peak at 5300 keV could be produced either by a contamination in  $^{210}\text{Pb}$  or  $^{210}\text{Po}$ . While  $^{210}\text{Po}$  has a rather short half life ( $\tau \simeq 138$  days), the half life of  $^{210}\text{Pb}$  is much longer ( $\tau \simeq 22$  years). Therefore, since a decrease of the peak intensity was not observed in few years, this peak was attributed to  $^{210}\text{Pb}$ . The position of the peak (it is centered at the energy of the  $\alpha$ , and not  $\alpha$ +recoil) indicates that the contamination has to be on a very thin layer either on the crystal surface or on the passive materials surface. From the coincidence spectra and scatter plots it is then possible to conclude that at least part of the peak is produced by a contamination of the crystal surfaces.
- the  $\alpha$  peak at 5400 keV was observed to decrease with time, in agreement with  $^{210}\text{Po}$  half-life. Usually observed in recently grown  $\text{TeO}_2$  crystals, this peak is produced by bulk contaminations, as it produces no events in the double hit spectrum. However part of the peak is a consequence of the U and  $^{210}\text{Pb}$  surface contamination discussed above: when CUORICINO was started this peak was by

far dominated by the bulk  $^{210}\text{Po}$  contaminations, while now the peak has a much reduced intensity and the surface contamination seems to dominate.

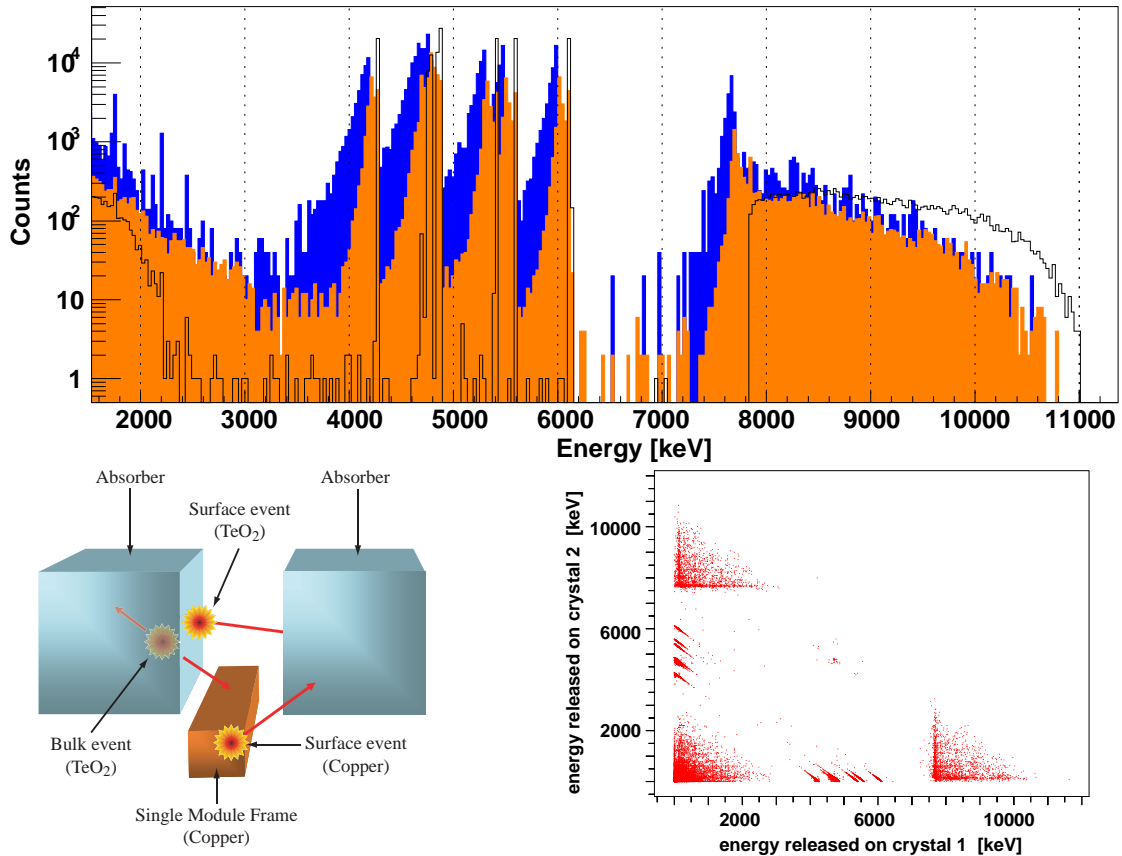


**Figure 3.12:** Alpha contaminations in CUORICINO. The top picture shows the Monte Carlo simulation of the single hit spectrum produced in CUORICINO by  $^{238}\text{U}$  contaminations in the crystal bulk (black line), crystal surfaces (orange filled) and copper mounting surfaces (blue filled). Surface contaminations have been simulated with an exponentially decaying density profile and  $1\mu\text{m}$  thickness. The bottom left picture shows the possible  $\alpha$  patterns in CUORICINO. The bottom right picture shows a scatter plot of coincident events for the crystal surface contaminations.

While the origin of the  $\alpha$  peaks is rather understood, it is quite a complex task to characterize the continuous background that extends down to the  $0\nu\beta\beta$  region. It is difficult to associate it to a particular  $\alpha$  peak and to identify the corresponding contaminant. Based on measurements made before the construction of CUORICINO, and on several dedicated tests performed on the R&D apparatus, major contributions from neutrons and from the small parts of the detector can be excluded (see sec. 5.5). Therefore most of the flat background measured by CUORICINO between 3 and 4 MeV should come from crystal and copper surfaces contaminations. Given the amount of events in the double hit spectrum in the 3-4 MeV range, it is possible to conclude that a non negligible fraction of the flat continuum has its source outside the crystals.

### 3.8.3 CUORICINO $0\nu\beta\beta$ results

The single hit energy spectrum collected by CUORICINO in the  $0\nu\beta\beta$  region is shown in fig. 3.13. It was obtained by summing the spectra from all detectors during the whole data taking period and corresponds to a total statistics of 11.83 kg · y in  $^{130}\text{Te}$ .

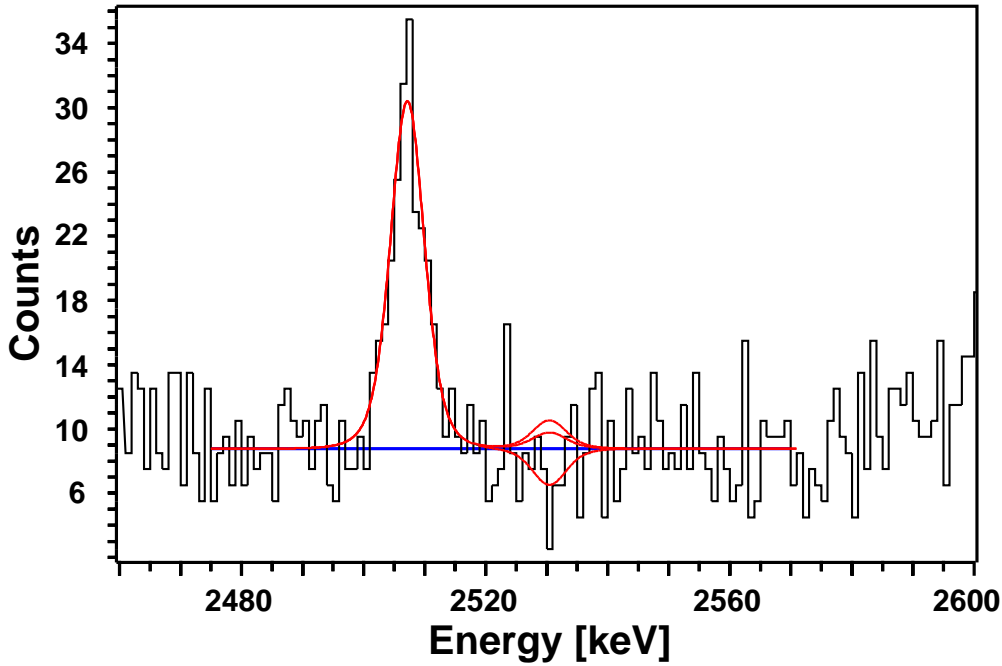


**Figure 3.13:** Single hit background spectrum summed over all detectors. The peak at 2505 keV is produced by the two  $\gamma$ s emitted in the  $\beta$  decay of  $^{60}\text{Co}$ . It is about  $7\sigma$  away from the position where the  $0\nu\beta\beta$  peak is expected and its contribution to the background is negligible. The red lines represent best fit, 68% and 90% C.L. on the number of events under the  $0\nu\beta\beta$  peak.

In order to evaluate the half-life limit, the peaks and the continuum in the  $0\nu\beta\beta$  region were analyzed using a maximum likelihood method [71, 72]. The six spectra from the two runs and from the three different kind of crystals ( $5 \times 5 \times 5 \text{ cm}^3$ ,  $3 \times 3 \times 6 \text{ cm}^3$  natural and  $3 \times 3 \times 6 \text{ cm}^3$  enriched) were combined allowing a different background level, and a different intensity of the 2505 keV  $^{60}\text{Co}$  peak. Other free parameters are the position of the  $^{60}\text{Co}$  peak and the number of counts under the  $0\nu\beta\beta$  peak. The response function for each spectrum was assumed to be a sum of symmetric Gaussian functions, each having the typical energy resolution of one of the detectors summed in that spectrum. Assuming a flat background, the fit in the region between 2575 and 2665 keV yields a negative number of counts under the  $0\nu\beta\beta$  peak ( $-13.9 \pm 8.7$ ). The resulting upper bound for the number of candidate events under the peak is  $n = 10.7$  at 90% C.L. This limit is then assumed to come from the sum spectrum of the entire statistical data set in which each of the six spectra is weighted based on the corresponding live time  $t$ , geometric efficiency  $\epsilon$ , and number of  $^{130}\text{Te}$  nuclei ( $N$ ). In

terms of these parameters the number of expected counts can be written as

$$n = \ln 2 \frac{1}{T_{1/2}^{0\nu}} \sum_{j=1}^6 N_j \epsilon_j t_j \quad (3.6)$$

The resulting lower limit on the half-life of  $^{130}\text{Te}$  is:

$$T_{1/2}^{0\nu} (^{130}\text{Te}) \geq 3.0 \times 10^{24} \text{y} \text{ (90\%CL)} \quad (3.7)$$

Systematic uncertainties in the evaluation of the half life limit come from the live time,  $Q$ -value, and background spectral shape. For example, changing from 0 to 2 the degree of the polynomial curve used to describe the background, or the energy window used in the fit, the bound varies in the range  $2.5 \div 3.3 \times 10^{24}$  y.

### 3.9 Limits on the effective Majorana mass and test of the claim of discovery

Extracting the effective Majorana mass of the electron neutrino from the half-life requires the calculation of the nuclear matrix elements. As already discussed in chapter 1 this is a quite complex task, as  $0\nu\beta\beta$  isotopes are usually heavy nuclei and many nucleons are involved in the calculations. Since a reliable calculation using the shell model approach would require too much computational power, it is often preferred to use QRPA models. However, since these calculations depend on the selection of a number of parameters, the results from different authors give a significant spread, even for the same nucleus.

Table 3.2 shows several values of  $m_{\beta\beta}$  corresponding to  $T_{1/2}^{0\nu} (^{130}\text{Te}) = 3.0 \times 10^{24}$  y evaluated from the theoretical calculations of different authors. Apart for the value from ref. [73], which has been obtained from NSM calculations, all other values are based on QRPA. The different results lie within a factor of 3 to each other.

Ref.	$m_{\beta\beta}$ [eV]	Ref.	$m_{\beta\beta}$ [eV]	Ref.	$m_{\beta\beta}$ [eV]
[41]	0.46	[74]	0.42	[75]	0.60
[76]	0.19	[77]	0.33	[78]	0.55
[79]	0.52	[80]	0.68	[81]	0.29
[82]	0.47	[83]	0.64	[84]	0.41
[85]	0.42	[86]	0.39	[73]	0.58

**Table 3.2:** Various values of  $m_{\beta\beta}$  corresponding to  $T_{1/2}^{0\nu} (^{130}\text{Te}) = 3.0 \times 10^{24}$  y obtained by different theoretical calculations of the nuclear matrix elements. All calculations are based on QRPA approach, apart for the last one [73], which is based on Nuclear Shell Model.

Using the best and the worst case, the CUORICINO lower limit on the  $0\nu\beta\beta$  half life of  $^{130}\text{Te}$  corresponds to

$$m_{\beta\beta} < 0.19 \div 0.68 \text{ eV}. \quad (3.8)$$

At present CUORICINO is the only  $0\nu\beta\beta$ -decay experiment with a sufficient sensitivity to probe the range of effective Majorana mass implied by the claim of observation in  $^{76}\text{Ge}$  [40, 28]. It is easy to see from eq. (2.6) that the  $0\nu\beta\beta$  half life for  $^{130}\text{Te}$  can be written in terms of the half life of  $^{76}\text{Ge}$  as

$$T_{1/2}^{0\nu} (^{130}\text{Te}) = T_{1/2}^{0\nu} (^{76}\text{Ge}) \frac{F_N (^{76}\text{Ge})}{F_N (^{130}\text{Te})}, \quad (3.9)$$

where  $F_N \equiv G_{0\nu} \cdot |M_{0\nu}|^2$  is the nuclear factor of merit discussed in chapter 2. The  $3\sigma$  range for the  $0\nu\beta\beta$  half life of  $^{76}\text{Ge}$  quoted in [28] is

$$T_{1/2}^{0\nu} (^{76}\text{Ge}) = (0.69 \div 4.18) \times 10^{25} \text{ y } (3\sigma) \quad (3.10)$$

In order to find the the corresponding half life for  $^{130}\text{Te}$  and compare it with the CUORICINO limit, some nuclear factor of merit must be chosen. Using for this scope the values of  $F_N$  obtained from recent QRPA ([41, 85]) and shell model ([73]) calculations, it is possible to obtain the results shown in fig. 3.14. The corresponding numerical values are reported in tab. 3.3. Figure 3.14 shows that CUORICINO has explored part of the range of  $m_{\beta\beta}$  allowed by the claim of discovery in  $^{76}\text{Ge}$ , but does not have enough sensitivity to refute it.

Ref.	$F_N (^{76}\text{Ge})$ [ $10^{-13} \text{ y}^{-1}$ ]	$F_N (^{130}\text{Te})$ [ $10^{-13} \text{ y}^{-1}$ ]	$T_{1/2}^{0\nu} (^{130}\text{Te})$ [ $10^{24} \text{ y}$ ]
[41]	1.22	4.84	$1.7 \div 10.5$
[85]	0.70	5.13	$0.9 \div 5.7$
[73]	0.43	2.57	$1.2 \div 7.0$

**Table 3.3:**  $0\nu\beta\beta$  half life of  $^{130}\text{Te}$  extrapolated from the claim of observation in  $^{76}\text{Ge}$  using nuclear matrix element calculations from three different authors.

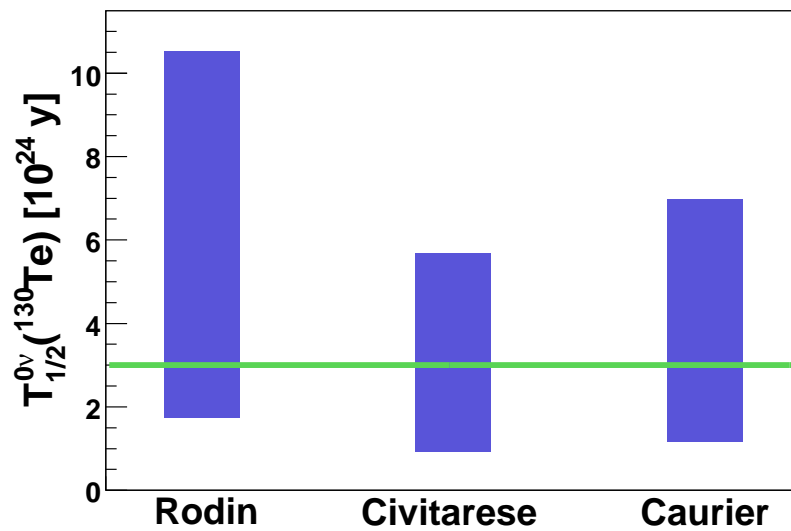


**Figure 3.14:** CUORICINO  $0\nu\beta\beta$  limit (horizontal green line) compared with the claim of observation. The blue bars represent the  $3\sigma$  range in which a signal should be seen in  $^{130}\text{Te}$  experiments. The left, center and right bars are obtained using the NME calculations from [41], [85] and [73] respectively.



# Chapter 4

## Search for double beta decay to excited states with CUORICINO

### 4.1 Introduction

Even if the main scientific goal of CUORE and CUORICINO is the search for neutrinoless double beta decay of  $^{130}\text{Te}$ , there are several other studies that can be carried out with these low background detectors. These include for example the search of dark matter, rare nuclear processes or double beta decay modes other than  $0\nu\beta\beta$  to the ground state.

In this chapter an analysis of  $^{130}\text{Te}$  double beta decay to excited states carried out on a data set acquired by CUORICINO will be presented. In particular the attention was focused on the  $2\nu\beta\beta$  decay mode of  $^{130}\text{Te}$  to the excited state  $0_1^+$  of the daughter nucleus  $^{130}\text{Xe}$ .

Because of the lower available phase space, neutrinoless double beta decay to excited states is not the best process for the investigation of the Majorana nature of neutrinos. As discussed in chapter 2, a smaller phase space corresponds to a lower decay probability and to a higher background level. However, since the decay to excited states is accompanied by the simultaneous emission of one or more photons, their detection could lead to a clear signature and to a strong reduction of the background.

Moreover in the nuclear matrix elements calculations based on QRPA, the dependence on the parameter  $g_{pp}$  is completely different for transitions to the ground and to excited states [87, 88]. Therefore the investigation of double beta decay to excited states could provide useful constraints for these calculations.

### 4.2 Double beta decay to excited states

The first investigation of double beta decay to excited states was performed by E. Fiorini in 1977 [89] as a side study in an experiment whose main purpose was the search

of  $0\nu\beta\beta$  decay to the ground state in  $^{76}\text{Ge}$ . The first dedicated search was done in 1982 [90], while the first positive signal was obtained in 1995 for the  $2\nu\beta\beta$  decay mode of  $^{100}\text{Mo}$  to the excited state  $0^+$  of  $^{100}\text{Ru}$  [91].

Besides the decay to the ground state of the daughter nucleus, both  $0\nu\beta\beta$  and  $2\nu\beta\beta$  decays can occur through the  $0^+$  and the  $2^+$  excited states:

- **$2\nu\beta\beta$  decay to excited state  $2^+$ :** present experimental limits and theoretical predictions for the half life of this decay mode are reported in tab. 4.1. It is strongly suppressed and practically inaccessible to detection. There are however encouraging theoretical predictions for several nuclei ( $^{96}\text{Zr}$ ,  $^{100}\text{Mo}$ ,  $^{130}\text{Te}$ ) that open the possibility to search for this decay mode in next generation experiments.
- **$2\nu\beta\beta$  decay to excited state  $0^+$ :** this is the most promising decay mode from an experimental perspective and indeed it has been observed in  $^{100}\text{Mo}$  and  $^{150}\text{Nd}$ . The measured half lives for  $^{100}\text{Mo}$  and  $^{150}\text{Nd}$  and lower limits for other isotopes are reported in tab. 4.2.
- **$0\nu\beta\beta$  decay to excited state  $2^+$ :** this decay mode is considered to be possible because of the contribution of right handed currents. However it is strongly suppressed and is not much sensitive to the neutrino mass contribution. The best experimental limits are reported in tab. 4.3.
- **$0\nu\beta\beta$  decay to excited state  $0^+$ :** this decay mode provides a clear signature, as two photons are emitted together with the two electrons whose sum energy is fixed. In an experiment with high geometric efficiency this signature would allow to reduce the background level to nearly zero. The best experimental limits are reported in tab. 4.4.

Isotope	$Q_{\beta\beta}$ [keV]	$T_{1/2}$ exp. [y]	$T_{1/2}$ theor. [92] [y]	$T_{1/2}$ theor. [93, 88] [y]
$^{48}\text{Ca}$	3288.5	$> 1.8 \times 10^{20}$ [94]	$1.7 \times 10^{24}$	-
$^{76}\text{Ge}$	1480	$> 1.1 \times 10^{21}$ [95]	$5.8 \times 10^{28}$	$7.8 \div 10 \times 10^{25}$
$^{82}\text{Se}$	2218.5	$> 1.4 \times 10^{21}$ [96]	-	$2.8 \times 10^{23} \div 3.3 \times 10^{26}$
$^{96}\text{Zr}$	2572.2	$> 7.9 \times 10^{19}$ [97]	$2.3 \times 10^{25}$	$3.8 \div 4.8 \times 10^{21}$
$^{100}\text{Mo}$	2494.5	$> 1.6 \times 10^{21}$ [91]	$1.2 \times 10^{25}$	$3.4 \times 10^{22}$
$^{116}\text{Cd}$	1511.5	$> 2.3 \times 10^{21}$ [98]	$3.4 \times 10^{26}$	$1.1 \times 10^{24}$
$^{130}\text{Te}$	1992.7	$> 2.8 \times 10^{21}$ [99]	$6.9 \times 10^{26}$	$3.0 \div 27 \times 10^{22}$
$^{150}\text{Nd}$	3033.6	$> 9.1 \times 10^{19}$ [100]	-	-

**Table 4.1:** Experimental limits and theoretical evaluations for the half life of  $2\nu\beta\beta$  decay to the excited state  $2^+$ . Experimental limits are at 90% C.L.

Isotope	$Q_{\beta\beta}$ [keV]	$T_{1/2}$ exp. [y]	$T_{1/2}$ theor. [93, 88] [y]	$T_{1/2}$ theor. [101] [y]
$^{48}\text{Ca}$	1274.8	$> 1.5 \times 10^{20}$ [94]	-	-
$^{76}\text{Ge}$	916.7	$> 6.2 \times 10^{21}$ [102]	$7.5 \div 310 \times 10^{21}$	$4.5 \times 10^{21}$
$^{82}\text{Se}$	1507.5	$> 3.0 \times 10^{21}$ [96]	$1.5 \div 3.3 \times 10^{21}$	-
$^{96}\text{Zr}$	2202.5	$> 6.8 \times 10^{19}$ [97]	$2.4 \div 2.7 \times 10^{21}$	$3.8 \times 10^{21}$
$^{100}\text{Mo}$	1903.7	$= 6.2^{+0.9}_{-0.7} \times 10^{20}$ [103, 104]	$1.6 \times 10^{21}$	$2.1 \times 10^{21}$
$^{116}\text{Cd}$	1048.2	$> 2.0 \times 10^{21}$ [98]	$1.1 \times 10^{22}$	$1.1 \times 10^{21}$
$^{130}\text{Te}$	735.3	$> 2.3 \times 10^{21}$ [105]	$5.1 \div 14 \times 10^{22}$	-
$^{150}\text{Nd}$	2627.1	$= 1.4^{+0.5}_{-0.4} \times 10^{20}$ [106]	-	-

**Table 4.2:** Experimental measurements and theoretical evaluations for the half life of  $2\nu\beta\beta$  decay to the excited state  $0_1^+$ . Experimental limits are at 90% C.L.

Isotope	$Q_{\beta\beta}$ [keV]	$T_{1/2}$ exp. [y]	$T_{1/2}$ theor. [107] [y]
$^{76}\text{Ge}$	1480	$> 8.2 \times 10^{23}$ [108]	$8.2 \times 10^{31}$
$^{82}\text{Se}$	2218.5	$> 2.8 \times 10^{21}$ [109]	-
$^{100}\text{Mo}$	2494.5	$> 1.6 \times 10^{23}$ [110]	$6.8 \times 10^{30}$
$^{116}\text{Cd}$	1511.5	$> 2.9 \times 10^{22}$ [31]	-
$^{130}\text{Te}$	1992.7	$> 1.4 \times 10^{23}$ [58]	-
$^{136}\text{Xe}$	1649.4	$> 6.5 \times 10^{21}$ [111]	-

**Table 4.3:** Experimental measurements and theoretical predictions (for  $m_{\beta\beta} = 1$  eV) for the half life of  $0\nu\beta\beta$  decay to the excited state  $2_1^+$ . Experimental limits are at 90% C.L.

Isotope	$Q_{\beta\beta}$ [keV]	$T_{1/2}$ exp. [y]	$T_{1/2}$ theor. [112, 113, 114, 115] [y]	$T_{1/2}$ theor. [116] [y]
$^{76}\text{Ge}$	916.7	$> 1.3 \times 10^{22}$ [117]	$4.9 \times 10^{26}$	$2.4 \times 10^{26}$
$^{48}\text{Ca}$	1274.8	$> 1.5 \times 10^{20}$ [94]	-	-
$^{82}\text{Se}$	1507.5	$> 3.0 \times 10^{21}$ [96]	$9.5 \times 10^{26}$	$4.5 \times 10^{25}$
$^{96}\text{Zr}$	2202.5	$> 6.8 \times 10^{19}$ [97]	$2.4 \times 10^{24}$	-
$^{100}\text{Mo}$	1903.7	$> 8.9 \times 10^{22}$ [110]	$2.6 \times 10^{26}$	$1.5 \times 10^{25}$
$^{116}\text{Cd}$	1048.2	$> 1.4 \times 10^{22}$ [31]	$1.5 \times 10^{27}$	-
$^{130}\text{Te}$	735.3	$> 3.1 \times 10^{22}$ [58]	$7.5 \times 10^{25}$	-
$^{150}\text{Nd}$	2627.1	$> 1.0 \times 10^{20}$ [100]	-	-

**Table 4.4:** Experimental measurements and theoretical predictions (for  $m_{\beta\beta} = 1$  eV) for the half life of  $0\nu\beta\beta$  decay to the excited state  $0_1^+$ . Experimental limits are at 90% C.L.

### 4.3 $2\nu\beta\beta$ decay of $^{130}\text{Te}$ to the excited state $0_1^+$

The analysis presented in this chapter was focused on the search of the two neutrino double beta decay of  $^{130}\text{Te}$  into the excited state  $0_1^+$  of  $^{130}\text{Xe}$ . The excitation levels of  $^{130}\text{Xe}$  accessible in double beta decay of  $^{130}\text{Te}$  are shown in fig. 4.1. These levels are valid for both the  $0\nu\beta\beta$  and the  $2\nu\beta\beta$  decay modes.

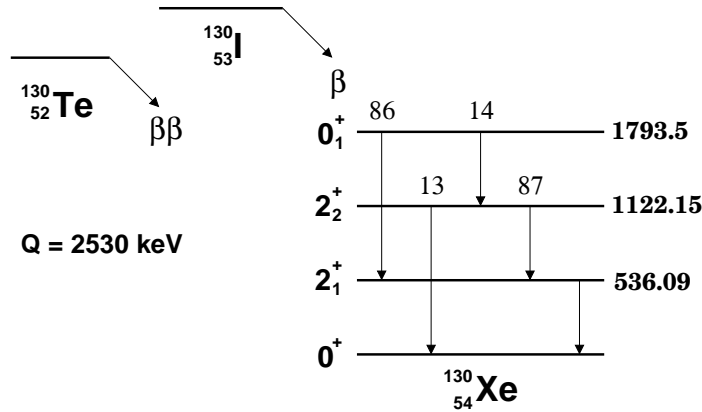


Figure 4.1: Nuclear levels of the  $^{130}\text{Te}$ - $^{130}\text{I}$ - $^{130}\text{Xe}$  triplet.

In the case of  $2\nu\beta\beta$  decay to the excited level  $0_1^+$  the sum energy of the two emitted electrons produces a continuous spectrum ranging from 0 to 736.5 keV, the upper limit arising from the energy difference between the Q-value of  $^{130}\text{Te}$   $\beta\beta$ -decay (2530 keV) and the excitation energy of the  $0_1^+$  level of  $^{130}\text{Xe}$  (1793.5 keV). Three possible decay schemes are allowed for the deexcitation of  $^{130}\text{Xe}$ :

- 1) in most cases (86%) the emission of the two electrons is accompanied by the emission of a 1257 keV and a 536 keV photon;
- 2) there is also the possibility that three photons are emitted (the relative intensity of this pattern is  $\sim 12\%$ ): a 671 keV, a 586 keV and a 536 keV photon;
- 3) finally there is less than 2% probability that a 671 keV and a 1122 keV photon are emitted.

Even if in principle any of these three patterns could be investigated, the attention was concentrated in this analysis to the first one, in which the 536 keV and the 1257 keV photons are emitted. Besides being the most probable one, this pattern allows to search for a  $\gamma$  peak at higher energy, where the background is lower. Further background reduction can be achieved by searching for events in which more than one crystal is hit: for this kind of analysis the first of the three patterns results in an higher detection efficiency, as  $\gamma$ s with higher energy are more likely to escape from the crystal where the decay occurs.

## 4.4 Analysis approach

The data set used in this analysis corresponds to the CUORICINO data acquired in the period between January and August 2007, resulting into a statistics of about 2.38 kg·y in  $^{130}\text{Te}$ . The general approach was to search for the peak produced by the 1257 keV photon emitted in the deexcitation of  $^{130}\text{Xe}$ , looking at the energy spectrum obtained by selecting those events in which two crystals were hit.

In general the expected number of counts  $c$  produced in a detector by a physical process with half life  $T_{1/2}$  can be expressed as

$$c = \frac{\ln 2}{T_{1/2}} \cdot N \cdot t \cdot \epsilon, \quad (4.1)$$

where  $N$  is the number of decaying isotopes put under observation,  $t$  is the duration of the observation and  $\epsilon$  is the detection efficiency for a given decay pattern. Therefore the half life corresponding to a certain number of observed counts is given by

$$T_{1/2} = \frac{\ln 2 \cdot N \cdot t \cdot \epsilon}{c}. \quad (4.2)$$

However, in order to claim for a positive signal, the number of counts produced by the studied physical process must be significantly higher than the possible fluctuations in the number of background events. Assuming Poisson statistics, the previous statement traduces in the requirement that  $c > n_\sigma \sqrt{b}$ , where  $b$  is the number of background counts and  $n_\sigma$  is the number of standard deviations, which expresses the statistical significance of the result. Therefore the half life sensitivity  $S_{1/2}$  for a given physical process can be written as

$$S_{1/2} = \frac{\ln 2 \cdot N \cdot t \cdot \epsilon}{n_\sigma \sqrt{b}}. \quad (4.3)$$

Even if expressed in terms of other parameters, eq. (4.3) is the equivalent of eq. (2.2) discussed in chapter 2.

Since in the present analysis all other parameters were fixed, the best sensitivity could be obtained by maximizing the ratio  $\epsilon/\sqrt{b}$ . While this was the basic reason that lead to the choice of searching for the 1257 keV peak in the double hit energy spectrum, several other criteria in the event selection could be considered to achieve an even better sensitivity. For example it is possible to require that the sum energy of the two hits in an event has to be lower than a certain threshold. This would allow to reduce the background by rejecting all those events whose sum energy is higher than the total energy available in the decay ( $Q_{\beta\beta} = 2530$  keV), without affecting the detection efficiency.

Several other selection criteria have been investigated in this analysis, which will be discussed in the following sections. However the general approach was to study, for each set of event selection cuts, the resulting detection efficiency and the corresponding

number of counts observed in the region of the energy spectrum where the 1257 keV peak is expected.

In order to evaluate the detection efficiency a Monte Carlo simulation was used to generate about 120000 events for the decay being investigated. With the program Tower-4.8.2, based on GEANT4, the simultaneous emission of the two  $\beta\beta$  electrons (sum energy between 0 and 736 keV) and two photons ( $E_{\gamma_1} = 536.09$  keV,  $E_{\gamma_2} = 1257.41$  keV) was simulated within the crystals of the CUORICINO tower, with an energy resolution of 5 keV (FWHM). The obtained energy spectrum, summed over all the detectors, is shown in fig. 4.2. The  $\gamma$  peak at 536 keV, the one at 1257 keV, as well as the sum peak at 1793 keV are clearly visible.

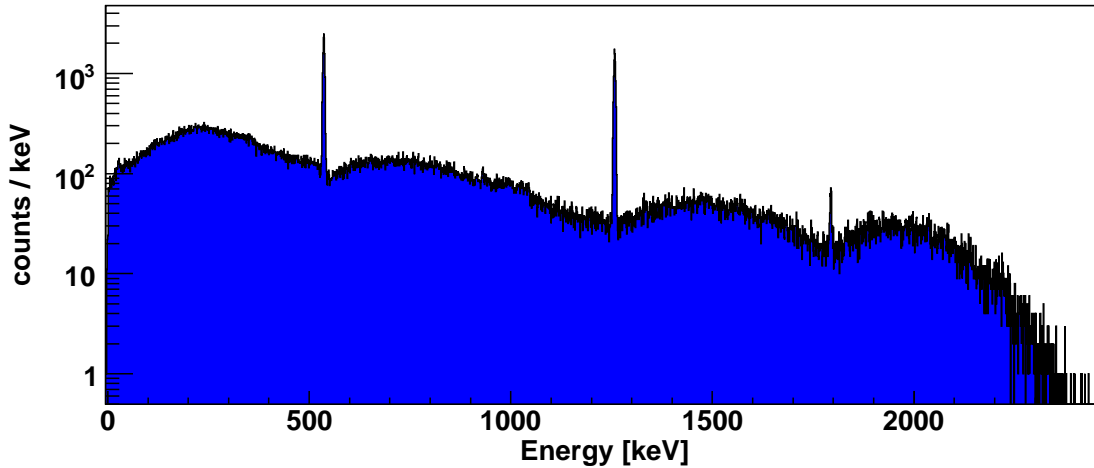


**Figure 4.2:** Energy spectrum obtained from the Monte Carlo simulation of 120000 events of the  $2\nu\beta\beta$  decay to the excited state  $0_1^+$ . The spectrum is the sum over all the CUORICINO detectors.

## 4.5 Description of the algorithms

The analysis presented in this chapter has been performed using Diana, the offline data analysis framework developed for CUORE. Despite Diana allows to perform a complete study of the data, starting from the raw pulses up to the final energy spectra, in this analysis a data set was considered where the energy calibration had already been applied, as well as all the quality cuts based on the single pulses used to remove spurious events induced by instabilities in the cryogenic apparatus or other kind of noise. Therefore the starting point was a set of events, each of them being characterized by the following quantities:

- energy
- crystal where the energy release occurred

- run number
- arrival time of the event referred to the beginning of the run

In order to deal with coincident events occurring at the same time on different crystals a new package was developed within the Diana framework. After building groups of events occurring within a given time window with respect to each other, this package allows to restrict the analysis to a subset of such groups based on one or more selection criteria. The following data filters were developed for the specific purpose of this analysis:

- **Multiplicity:** this filter allows to select events based on the number of energy releases in different detectors.
- **Total energy:** the purpose of this filter is to select events whose sum energy over all the hits is contained within a certain range.
- **Energy of single hit:** this filter allows to select groups of coincident events based on the energy of the single hits.
- **Spatial distance:** this filter allows to select coincident events occurring in two or more crystals that are within a certain spatial distance to each others.

Since bolometers are intrinsically slow, energy deposits in different crystals that are caused by the same physical process are expected to occur within a time window that is much smaller than the typical response time of the thermal signals. However, due to the spread in the pulse shape, the trigger algorithm introduces a non negligible jitter in the time associated to the events belonging to different detectors. As a consequence, the time window used in the definition of coincident events must account for this jitter, that causes a spread in the arrival time associated to different energy releases.

In order to find the best window length for the definition of coincidences, the same data set was processed using different values for this parameter. Figure 4.3 shows the number of events with multiplicity 1 and 2 obtained for several durations of the coincidence time window between 15 and 350 ms: in both the plots there is a clear change in the slope at about 80 ms, separating the two regions dominated by physical and accidental coincidences. After this check a 100 ms coincidence time window was chosen for the analysis, slightly above the change in the trend of the two curves reported in fig. 4.3. The choice of the coincidence time window obviously does not affect the simulated data, as in that case coincident events occur by construction exactly at the same time.

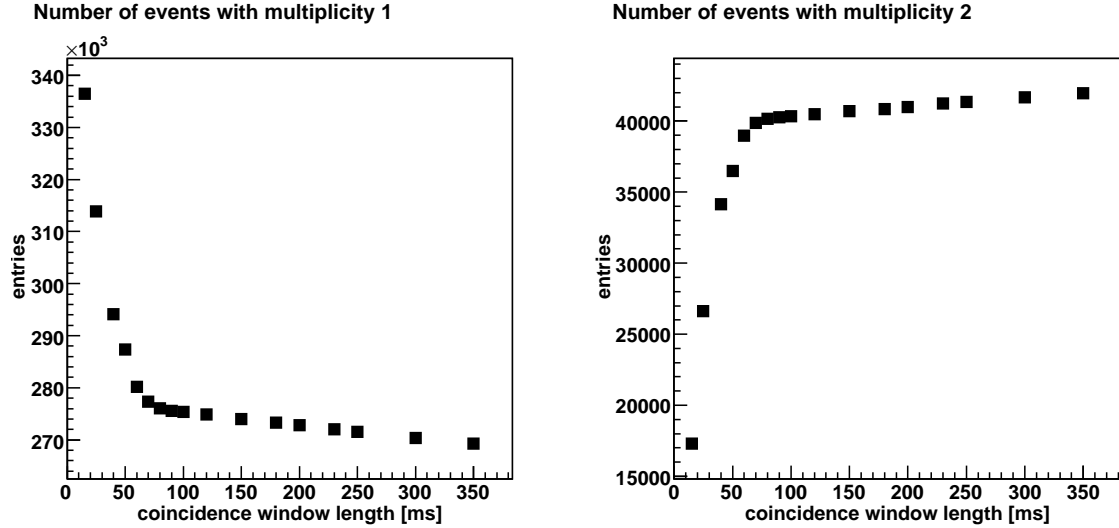


**Figure 4.3:** Evaluation of the optimal time window for the definition of coincident events. The two plots show number the of events with multiplicity 1 (left) and 2 (right) versus the length of time window used to build the coincidences. The change in the slope at about 80 ms separates the two regions dominated by physical and accidental coincidences.

## 4.6 Evaluation of efficiency and live time

The evaluation of the live time and the detection efficiency were corrected to account for possible time periods in which one or more detectors were not operative. For this purpose the data acquired in the time period considered in this analysis was checked for the presence of *time holes*, which are caused by noise in the cryogenic apparatus, or any other kind problems in the readout chain. The procedure used to apply the time holes to simulated data is shown in fig. 4.4. After discarding the time intervals in which all the detectors were inactive (for example during the run stops due to cryogenics maintenance), the length of each time hole was multiplied by a scale factor to account for the different duration of the real and simulated measurements. The obtained “*mask*” was then applied to simulated data to discard events occurring during time holes.

Time holes were defined as time intervals containing no events and whose duration was longer than a certain threshold. This threshold was determined based on the event rate of each channel, using the requirement that the probability of having no events in a given time window had to be smaller than a certain level  $k$ . In this way it was possible to take into account the different event rates of different detectors. Assuming Poisson statistics for the event rate, the probability distribution for the time distance  $t$  between two consecutive events is given by [118]

$$P(t) = re^{-rt}, \quad (4.4)$$

where  $r$  is the event rate for a given detector. Thus the threshold  $t_0$  for the time

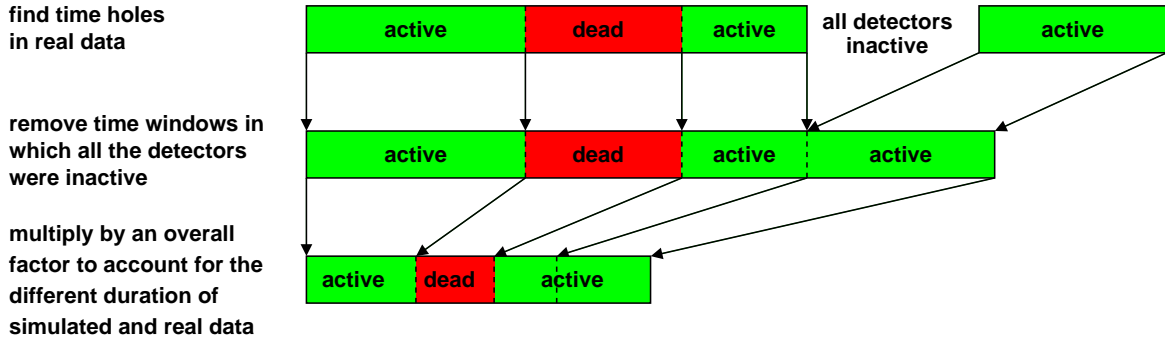


**Figure 4.4:** Procedure used for the evaluation of the detection inefficiency produced by the presence of some inactive detectors during data taking. For each detector, possible periods of inactivity were checked in the real data. These inactivity periods were then reported to simulated data after proper time rescaling to account for the different duration of the real and simulated measurements.

holes was obtained from the requirement

$$P(t > t_0) = \int_{t_0}^{\infty} P(t)dt = e^{-rt_0} < k, \rightarrow t_0 > -\log(k)/r \quad (4.5)$$

The event rates for different detectors, reported in fig. 4.5, were evaluated as the number of counts divided by the total duration of the considered measurements. Using eq. (4.5) the minimum duration for time holes was evaluated for several values of the threshold probability  $k$ . The results are shown in fig. 4.6, while the corresponding dead times obtained using such time hole thresholds on the real data are reported in fig. 4.7.

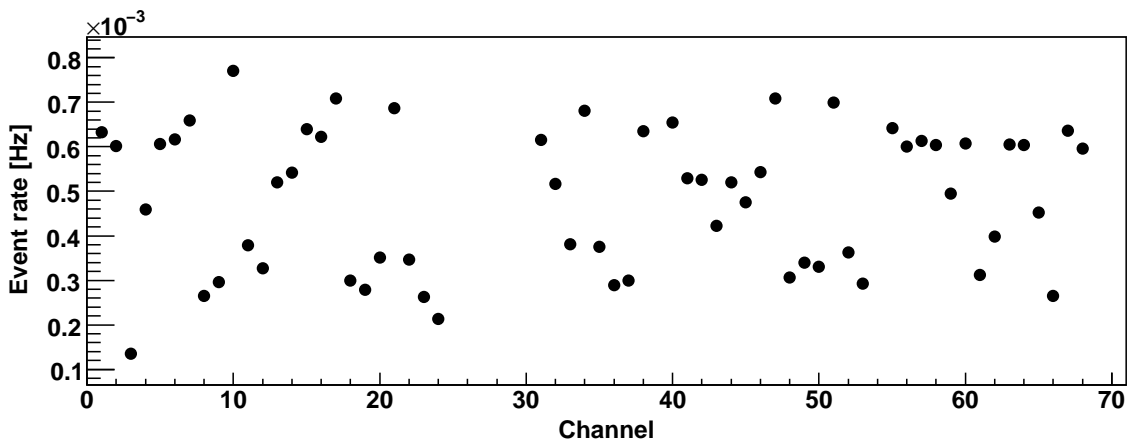


**Figure 4.5:** Average event rate for different channel in the time period considered in this analysis. The event rate was evaluated as the total number of events divided by the duration of the measurement.

The study of time holes was also used for the evaluation of the correct value for the accumulated statistics. This quantity was evaluated as:

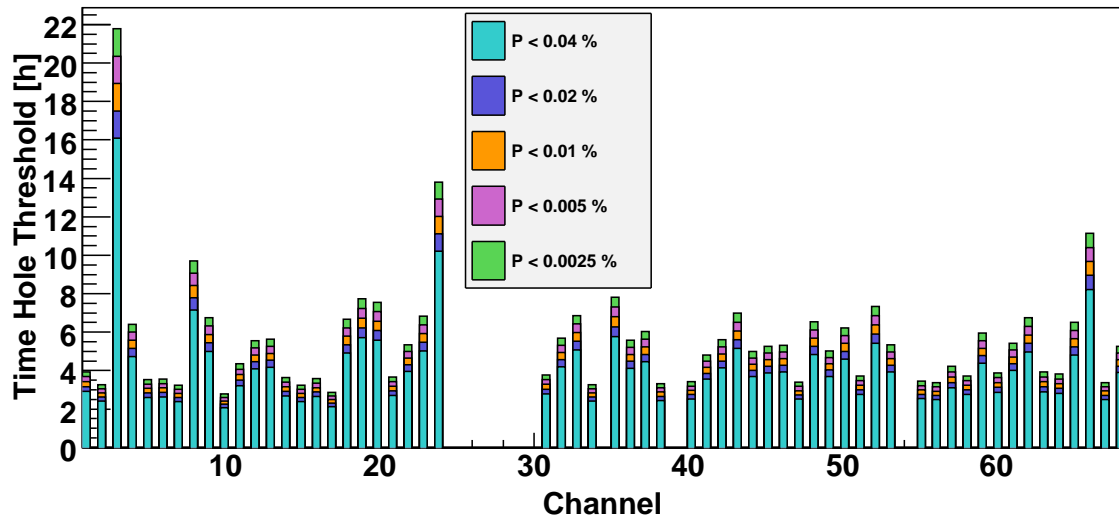


Figure 4.6: Time holes minimum duration on the CUORICINO channels for various values of the threshold probability (see eq. (4.5)).

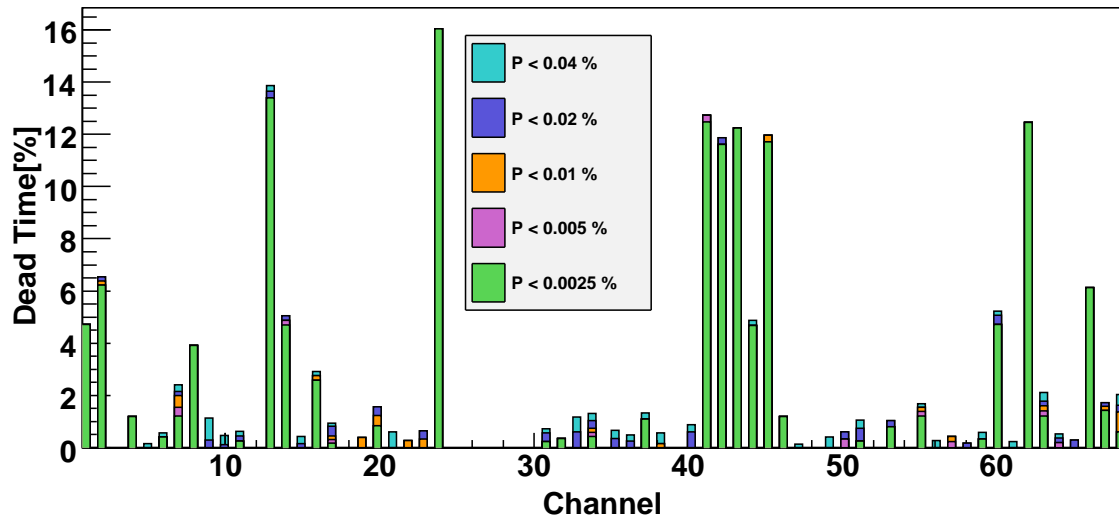


Figure 4.7: Dead time of the CUORICINO detectors for various values of the threshold probability used for the definition of time holes.

$$N \cdot t = T \sum_i N_i \cdot \eta_i, \quad (4.6)$$

where the sum runs over all the crystals in the tower,  $T$  is the total live time in the considered data set and  $N_i$  and  $\eta_i$  are respectively the number of  $^{130}\text{Te}$  nuclei and the relative live time of each detector. The resulting statistics are reported in tab. 4.5 for the various considered values for the threshold probability  $k$ . It can be seen that the presence of inactive detectors produces a sensible reduction of the accumulated statistics. However the systematic error introduced by the choice of different values for the threshold probability  $k$  is rather small.

threshold probability [%]	0	0.0025	0.005	0.01	0.02	0.04
kg · y	2.381	2.318	2.317	2.315	2.312	2.309
N · y [ $10^{25}y$ ]	1.103	1.074	1.073	1.072	1.071	1.070

**Table 4.5:** Accumulated statistics corrected for the time holes obtained with different values of the threshold probability  $k$ .  $k = 0$  corresponds to the case in which time holes were not considered.

Once the time holes were applied to simulated data with the described procedure, several event selection criteria were considered with the aim of maximizing the detection sensitivity (see sec. 4.4). Using the selection algorithms described in sec. 4.5, one or more of the following cuts were applied to the simulated data:

– **Multiplicity:**

Only events in which two crystals were hit were selected; as shown in fig. 4.8 the number of events with multiplicity 2 is quite high in the simulated data, while allowing a sensible reduction in the number of events of the real data.

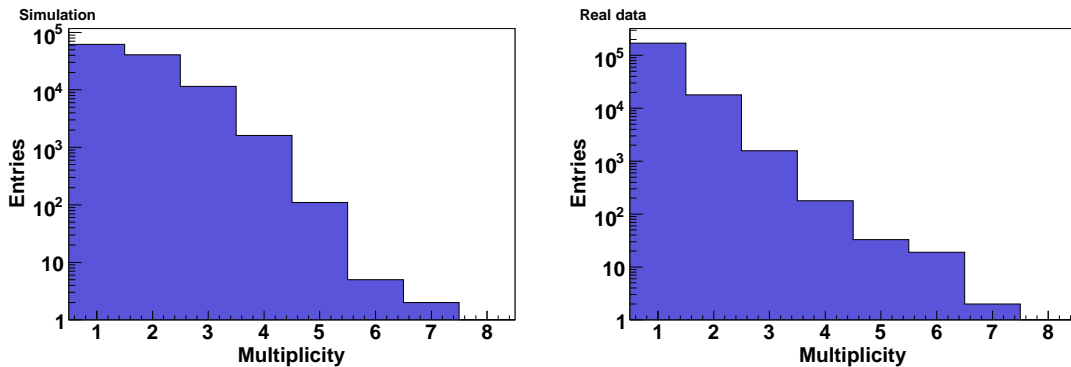


**Figure 4.8:** Multiplicity distribution of the simulated data (left) and real data (right).

– **Total energy:**

Only the events with sum energy between 400 keV and 2540 keV were taken into

account. The lower limit was dictated by the energy threshold chosen for the single detectors (200 keV), while the upper limit corresponds to the  $Q$ -value of the considered process ( $Q_{\beta\beta} = 2530\text{keV}$ ), plus a possible energy resolution spread of 5 keV for each of the two crystals.

– **Energy of single hit:**

Since the signature searched in the present analysis is the 1257 keV peak produced by one of the photons emitted in the deexcitation of  $^{130}\text{Xe}$ , a constraint was imposed on the energy of the single hits in the two crystals. This constraint corresponded to the requirement that one of the two crystals contained the 1257 keV photon, and the other one contained the sum energy of the 536 keV photon and of the two electrons. The chosen energy ranges were  $1230\div 1280$  keV (for the high energy photon) and  $526\div 1283$  keV (for the 536 keV  $\gamma$  and the two electrons, taking into account the spread produced by the finite energy resolution). It is worth noticing however that this selection criterion does not match only the case in which all the energy of the 536 keV  $\gamma$  is released within the crystal: the energy spectrum shown in fig. 4.2 demonstrates that there is a non negligible probability for this photon to escape from the crystal, and even in this case the two electrons could have a sum energy higher than 526 keV.

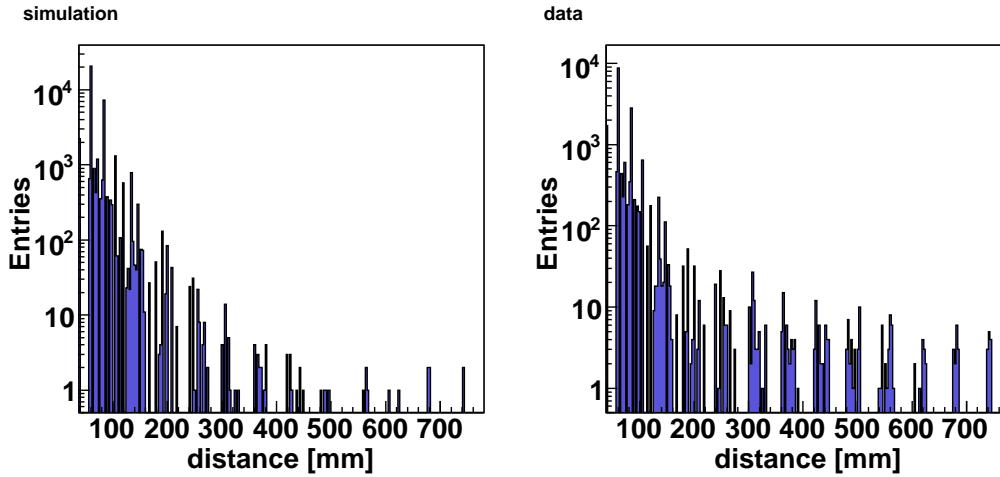
– **Spatial distance:**

Figure 4.9 shows the distribution of the spatial distance between the the center of the crystals in the double hit events. A cut at 107 mm was chosen, since in the simulation more than 90% of the events have a distance lower than this value. Given the size of the crystals (most of them have cubic shape with 50 mm side) and the spacing between them (about 10 mm), the limit case allowed by this cut corresponds to the two most far crystals on two consecutive floors of the CUORICINO tower.

In order to simplify the identification of the cuts, short names were defined, as reported in tab. 4.6.

No matter which cuts were applied, the detection efficiency was evaluated by fitting the simulated spectrum with a Gaussian peak centered at 1257 keV summed to a flat background introduced to account for the continuous spectrum produced by the two electrons. In the fit the peak amplitude, the background level and the peak width were left as free parameters, while the position of the peak was fixed to 1257.41 keV. The fit results were then used to evaluate the number of counts under the Gaussian peak, and the efficiency was evaluated by dividing the obtained number of events by the total number of events generated in the simulation.

An example of the fitting procedure is shown in fig. 4.10, for the case in which the cuts M2, TotE and Dist were applied. The same set of cuts was used to investigate the efficiency dependence on the value of the threshold probability  $k$  used in the definition of time holes. As for the evaluation of the live time, the result of this check, reported



**Figure 4.9:** Distance between the crystals in the multiplicity 2 events for the simulated data (left) and real data (right). When a cut based on the spatial distance was applied, a threshold value of 107 mm was used, corresponding to about 93% of the events.

Cut name	Description
M2	Two and only two crystals were hit
TotE	The sum energy of the two hits was between 400 keV and 2540 keV
Dist	The spatial distance between the two crystals was less than 107 mm
$E_{\gamma_1}$	One of the two hits was between 1230 keV and 1280 keV
$E_{\gamma_2}$	One of the two hits was between 526 keV and 1283 keV

**Table 4.6:** Description of the applied cuts. The M2 cuts corresponds to the selection of events in which two and only two crystals were hit. The TotE cut corresponds to the selection of events whose summed energy was less than 2540 keV (the threshold energy was chosen as  $Q_{\beta\beta}$  plus 5 keV energy resolution for each of the two crystals). The Dist cut corresponds to the selection of events in which the spatial distance between the two crystals is less than 107 mm. The two cuts  $E_{\gamma_1}$  and  $E_{\gamma_2}$  correspond to the selection of those events in which the energy of one of the two crystals was contained in a given range.

in tab. 4.7, shows that the presence of time holes introduces a sensible reduction in the detection efficiency, but the particular choice of the threshold probability does not affect too much the result. After this check the threshold probability  $k = 0.01\%$  was used in the rest of the analysis.

threshold probability [%]	0	0.0025	0.005	0.01	0.02	0.04
efficiency [%]	4.75	4.57	4.57	4.56	4.55	4.55

**Table 4.7:** Detection efficiency for different values of the threshold probability used in the determination of time holes. The quoted efficiency are referred to the case in which the cuts M2, TotE and Dist were applied.

Figure 4.11 shows the energy spectra obtained from simulated data for three different

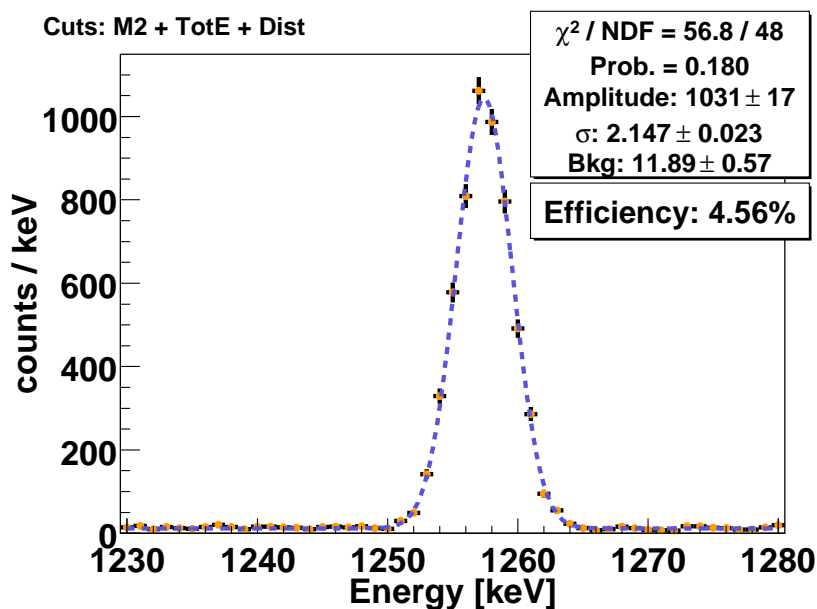


**Figure 4.10:** Example of the fitting procedure used to evaluate the detection efficiency. The plot shown in this figure refers to the case in which the cuts M2, TotE and Dist were applied and the correction for the time holes was applied using a threshold probability  $k=0.01\%$ .

sets of applied cuts. In the green-filled histogram the events with multiplicity 2 were selected (M2); in the blue-filled histogram further cuts were applied requiring that the sum energy of the two events in a coincidence was smaller than 2540 keV (TotE), and that the spatial distance between the two crystals was smaller than 107 mm (Dist). In the orange histogram further constraints were imposed on the energy releases on the two crystals of each event ( $E_{\gamma 1}$  and  $E_{\gamma 2}$ ). The resulting efficiencies, obtained with the already described procedure, are reported in tab. 4.8.

Cuts	Efficiency [%]
M2	4.98
M2 + TotE	4.98
M2 + TotE + Dist	4.56
M2 + TotE + Dist + $E_{\gamma 1}$ + $E_{\gamma 2}$	3.00

**Table 4.8:** Detection efficiency for different sets of applied cuts. The values reported in this table do not include the additional 0.86 factor that should be introduced to account for the relative intensity of the particular decay channel searched in the present analysis (see sec. 4.3).

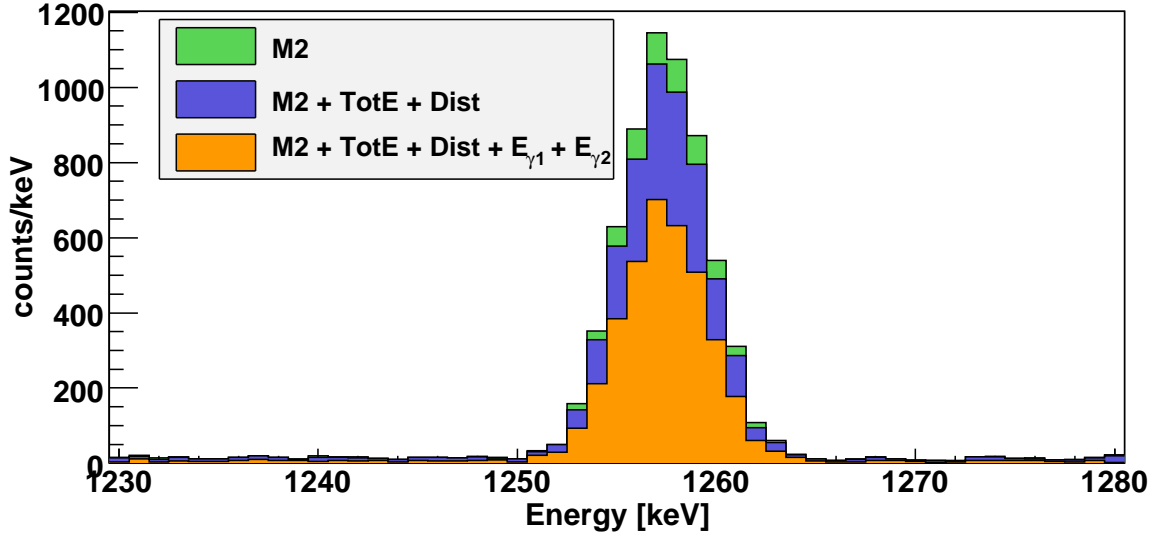


**Figure 4.11:** Example of the effect of the cuts on simulated data. The green-filled histogram shows the energy spectrum for the events with multiplicity 2 (M2). The blue-filled histogram was obtained after applying three concurrent cuts: M2, total energy in the two crystals less than 2540 keV (TotE) and spatial distance between the two crystals less than 107 mm (Dist). The orange-filled histogram was obtained by adding further requirements on the single energy of the two hit crystals: one hit between 1230 and 1280 keV ( $E_{\gamma 1}$ ) and the other between 526 and 1283 keV ( $E_{\gamma 2}$ ).

## 4.7 Analysis of the CUORICINO data

Figure 4.12 shows the single and double hit energy spectrum between 200 keV and 3000 keV measured by CUORICINO in the time period considered in the present analysis. As already discussed, the 1257 keV peak produced by the photon emitted in the deexcitation of  $^{130}\text{Xe}$  was searched in the double hit spectrum, where the background level is suppressed.

The same analysis procedure and the same event selection criteria used in the evaluation of the efficiency were replicated to the real data. The energy spectrum in the range of interest for the search of the 1257 keV peak is shown in fig. 4.13 for three different sets of cuts. It can be seen that, even if some reduction in the number of counts is obtained by adding the cuts based on the total energy and on the spatial distance between two crystals, the strongest background suppression is achieved by constraining the energy of the single hits. However, while the other cuts are based on general assumptions on the decay under investigation, the cuts based on the single energy releases could be satisfied not only in the case in which the 536 keV photon is completely absorbed in the crystal where the decay occurs, while the 1257 keV photon is completely absorbed by a neighbor crystal. The same constraint could be satisfied even in the case in which one of the two photons is not completely absorbed by the sensitive parts of the detector.

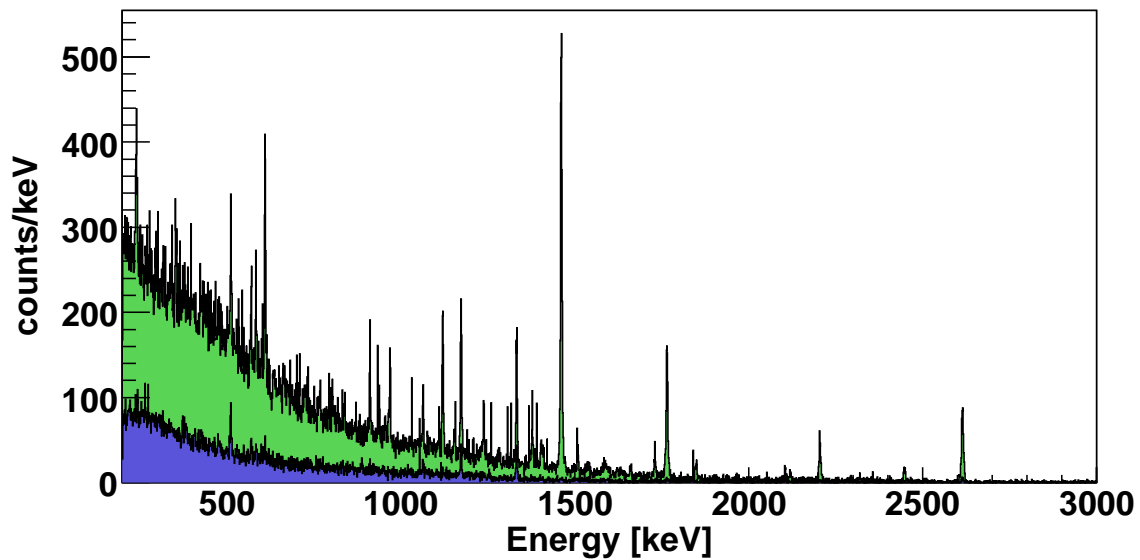


Figure 4.12: Comparison of the single and double hit spectra measured by CUORICINO during the data taking period used in the present analysis.

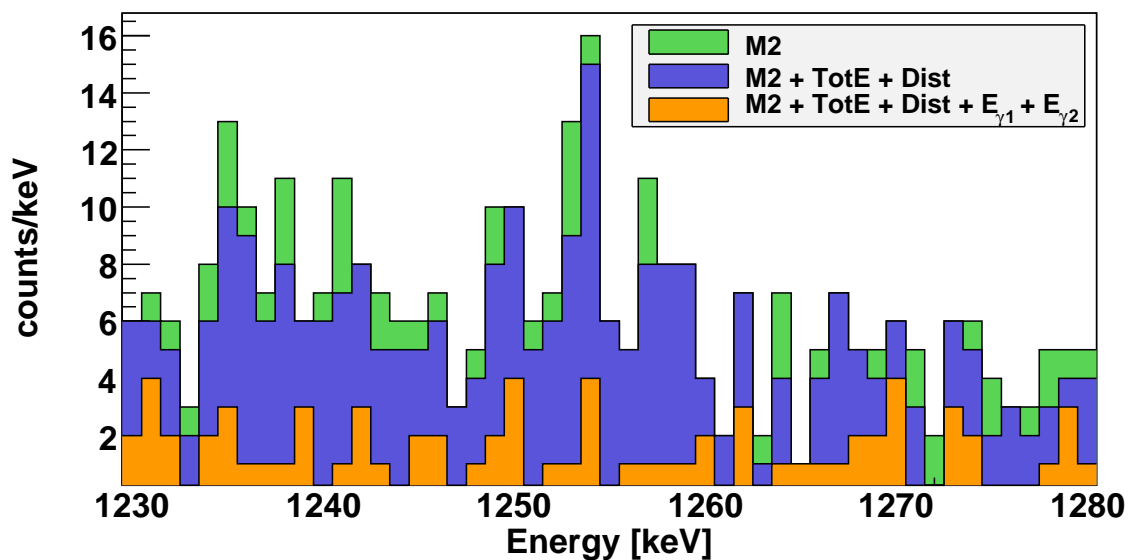
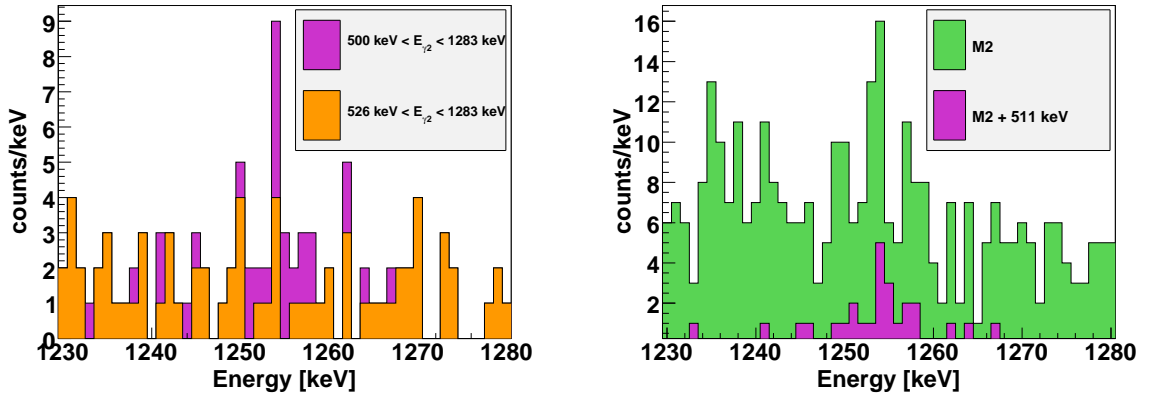


Figure 4.13: Energy spectrum obtained from the real data in the region of the 1257 keV peak after the application of several selection cuts.

In fig. 4.13 a structure is present at about 1253 keV: it is visible in the spectra obtained with the cuts M2 and M2+ TotE+ Dist, while it disappears in the case in which also the cuts  $E_{\gamma_1}$  and  $E_{\gamma_2}$  are applied. This structure cannot be interpreted as

the searched peak: its position is about 4 keV away from 1257.41 keV, while it will be shown later that the energy calibration is accurate within less than 1 keV. In fact this structure is likely to be caused by the single escape peak produced by the 1764.5 keV photon emitted in the  $\beta$  decay of  $^{214}\text{Bi}$ : it can make a  $e^+ - e^-$  pair, and one of the two 511 keV  $\gamma$ s emitted in the subsequent positron annihilation can escape from the detector. Under this assumption the hits under the peak at 1253.5 keV should be associated with hits around 511 keV in the other crystal. This would explain why the peak disappears when the cuts  $E_{\gamma 1}$  and  $E_{\gamma 2}$  are applied: the 511 keV peak is excluded in this case, as the  $E_{\gamma 2}$  cut only accepts events with energy greater than 526 keV (cfr. tab. 4.6). This hypothesis is confirmed by the two following observations:

- 1) even in the spectrum obtained from the cuts M2+ TotE+ Dist+  $E_{\gamma 1}$ +  $E_{\gamma 2}$  an excess of events appears around 1253 keV if the lower bound of the  $E_{\gamma 2}$  cut is set to 500 keV instead of 526 keV (see fig. 4.14(a)); in contrast, the number of events remains almost unchanged in the other regions of the energy spectrum;
- 2) considering the spectrum obtained from the cut M2, it can be seen from fig. 4.14(b) that part of the events around 1253 keV occurs in coincidence with events on another crystal whose energy is between 500 keV and 520 keV.



(a) Energy spectrum obtained from the cuts M2+ TotE+ Dist+  $E_{\gamma 1}$ +  $E_{\gamma 2}$ , for different values of the lower bound for the cut  $E_{\gamma 2}$ : 500 keV (purple-filled) and 526 keV (orange-filled). (b) Energy spectrum obtained from the cut M2 (green-filled) and from the further requirement that one of the two events had energy between 500 keV and 520 keV (purple-filled).

**Figure 4.14:** Explanation of the excess of events around 1253 keV: it is due to the single escape peak produced by the 1764 keV photon emitted in the  $\beta$  decay of  $^{214}\text{Bi}$ .

It was shown that, depending on the considered event selection criteria, the energy spectrum around 1257 keV presents different features. For this reason two different background models were considered to perform the fit on the data:

- 1) for the spectra obtained from the cuts M2 and M2+ TotE+ Dist the data was fit with a flat background summed to a Gaussian peak at 1253.5 keV (the single escape peak discussed above) and a Gaussian peak centered at 1257.41 keV (the searched signal);
- 2) for the spectrum obtained from the cuts M2+ TotE+ Dist+ E<sub>γ1</sub>+ E<sub>γ2</sub> the data was fit with a flat background summed to a Gaussian peak centered at 1257.41 keV, since in this case the single escape peak is not present.

The fit was performed using a maximum likelihood method in the assumption of Poisson statistics for the binned data, in which only the level of the flat background and the amplitude of the two peaks were left as free. The likelihood function was defined as

$$\mathcal{L} = \prod_i P(n_i | \lambda_i), \quad (4.7)$$

where the product runs over all the bins considered in the fit,  $n_i$  is the content of the  $i^{th}$  bin and  $\lambda_i$  is the expected number of counts in the  $i^{th}$  bin. For the cuts M2 and M2+ TotE+ Dist the *signal + background* model,  $\lambda_i$ , was parameterized as

$$\lambda_i = b + a \cdot e^{-\frac{(E_i - E_{1257})^2}{2\sigma^2}} + c \cdot e^{-\frac{(E_i - E_{1253})^2}{2\sigma^2}}. \quad (4.8)$$

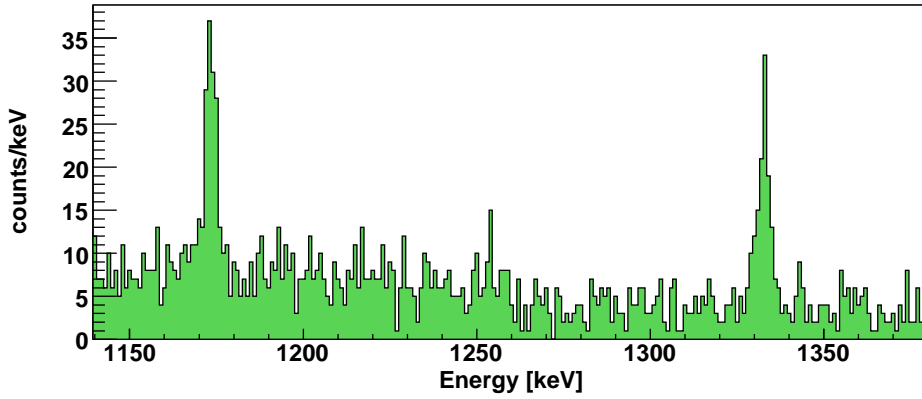
Similarly, for the case in which the 1253 keV peak was not considered (cuts M2+ TotE+ Dist+ E<sub>γ1</sub>+ E<sub>γ2</sub>), it was parameterized as

$$\lambda_i = b + a \cdot e^{-\frac{(E_i - E_{1257})^2}{2\sigma^2}}. \quad (4.9)$$

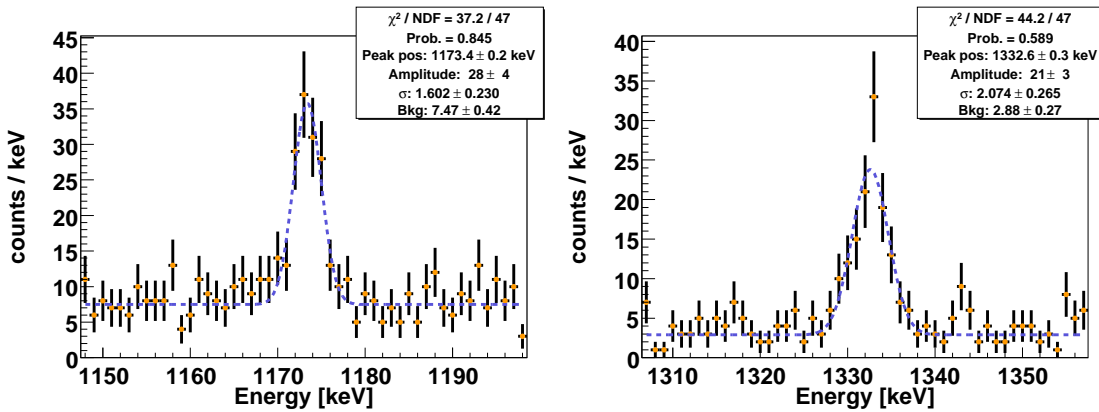
In eq. (4.8)  $b$  is the background level,  $a$  and  $c$  are respectively the 1257 keV and 1253 keV peak amplitudes and  $E_i$  is the center of the  $i^{th}$  bin in the energy spectrum. The same definitions hold for eq. (4.9), apart for the fact that the 1253 keV peak was not included in that case. The position of the two peaks were fixed to  $E_{1257}=1257.41$  keV and  $E_{1253}=1253.5$  keV.

The energy resolution was evaluated from the two  $\gamma$  peaks that are visible in the double hit spectrum at 1173.2 keV and 1332.5 keV (see fig. 4.15). As already discussed in chapter 3, these two peaks are produced by <sup>60</sup>Co contaminations in the cryostat radiation shields. Since the two  $\gamma$ s are produced simultaneously in <sup>60</sup>Co  $\beta$ -decay, they are present also in the double hit spectrum. Both these peaks were fitted with a Gaussian summed to a flat background. The position of the peak, its amplitude, as well as the peak width and the background level were left as free parameters in the fit.

Figure 4.16 shows the result of the fit on the two <sup>60</sup>Co peaks. They have the expected position within 0.2 keV: this validates the quality of the energy calibration procedure and excludes the possibility that the peak at 1253 keV is produced by the process that is being searched. Since the energy resolution is different in the two peaks ( $\sim 1.6$  keV for the 1173 keV peak and  $\sim 2.1$  keV for the 1332 keV peak), several different values were considered when performing the fit in the 1257 keV region.



**Figure 4.15:** Enlarged view of the double hit spectrum around 1257 keV. The two visible peaks at 1173 keV and 1332 keV are produced by  $^{60}\text{Co}$  contaminations in the cryostat radiation shields (see chapter 3).



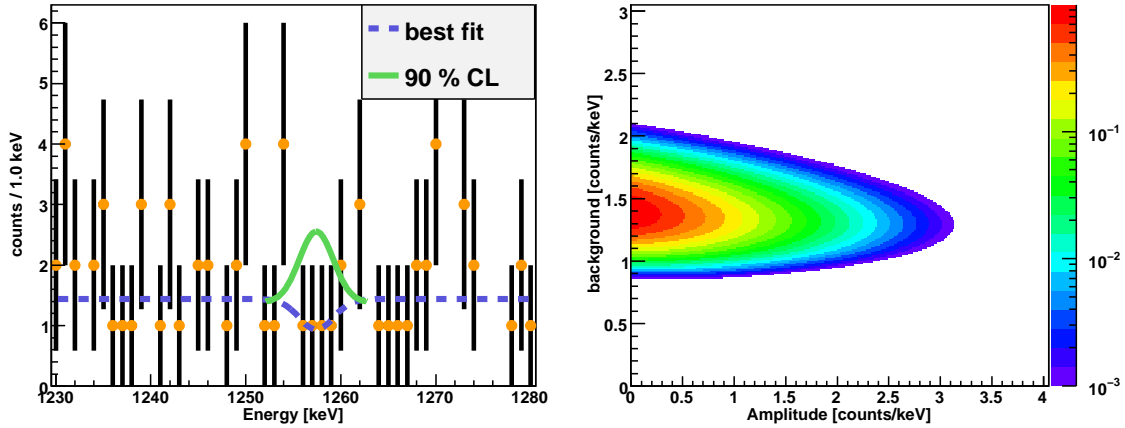
**Figure 4.16:** Fit on the 1173.2 keV (left) and 1332.5 keV (right)  $\gamma$  lines from  $^{60}\text{Co}$ , used to evaluate the energy resolution. The fit was performed on the data after applying the M2, TotE and Dist cuts (cfr. tab. 4.6).

Figure 4.17 shows an example of the fit in the case in which the 1253 keV peak was not considered in the background model. It was obtained from the energy spectrum in which the cuts M2+ TotE+ Dist+  $E_{\gamma 1}$ +  $E_{\gamma 2}$  were applied, and a value of  $\sigma = 1.8$  keV was used for the energy resolution. The best fit yielded a background level of  $1.44 \pm 0.18$  counts/keV and a negative amplitude for the 1257 keV peak:  $-0.50 \pm 0.61$  counts/keV. Since no evidence for a peak was found, a 90% C.L. upper limit was evaluated for the number of counts under the peak. After constraining the two free parameters in the physical region (amplitude and background greater than zero), the likelihood function was integrated over all the possible values of the background level and the upper limit for the peak amplitude was found by integrating over this parameter up to the 90% of the total volume of the function. Denoting by  $a$  the peak amplitude, and by  $b$  the background level (see eq. (4.9)) the 90% C.L. limit was

found as

$$\frac{\int_0^\infty db \int_0^{a(90\%C.L.)} da \mathcal{L}}{\int_0^\infty db \int_0^\infty da \mathcal{L}} = 0.9 \quad (4.10)$$

The limit on the number of counts under the peak was then found by integrating a Gaussian function with the same energy resolution used in the fit and with the amplitude obtained with the procedure described in eq. (4.10).



**Figure 4.17:** Example of fit for the case in which the 1253 keV peak was not included in the background model. The fit shown in this figure was performed on the energy spectrum in which the cuts M2+ TotE+ Dist+  $E_{\gamma 1} + E_{\gamma 2}$  were applied. An energy resolution of  $\sigma=1.8$  keV was used in the fit. The left plot shows the data, the best fit and the 90% C.L. limit. The right plot shows the likelihood function.

Figure 4.18 shows an example of the performed fit in the case in which the 1253 keV peak was considered in the background model. It was obtained from the energy spectrum in which only the M2 cut was applied, and a value of  $\sigma = 1.8$  keV was used for the energy resolution. For the example shown in fig. 4.18 the best fit yielded a background level of  $5.94 \pm 0.38$  counts/keV while the amplitude of the two peaks were  $5.3 \pm 1.9$  counts/keV (1253 keV peak) and  $1.1 \pm 1.6$  counts/keV (1257 keV peak). The 90% C.L. limit on the number of counts under the 1257 keV peak was obtained in the same way of the case in which the background was assumed to be flat (see eq. (4.10)), apart for the fact that the likelihood function was also integrated over all possible values of the amplitude of the 1253 keV peak.

The procedure described so far was repeated using different sets of selection cuts and for different values of the energy resolution and of the energy window used in the fit. The corresponding 90% C.L. upper limits for the number of counts under the peak were evaluated for various values of  $\sigma$  (tab. 4.9) and for various values of the fit range (tab. 4.10). Also the the position of the two peaks was moved to investigate the effects on the upper limits (tab. 4.11 and tab. 4.12 for the 1257 keV and 1253 keV peak respectively).

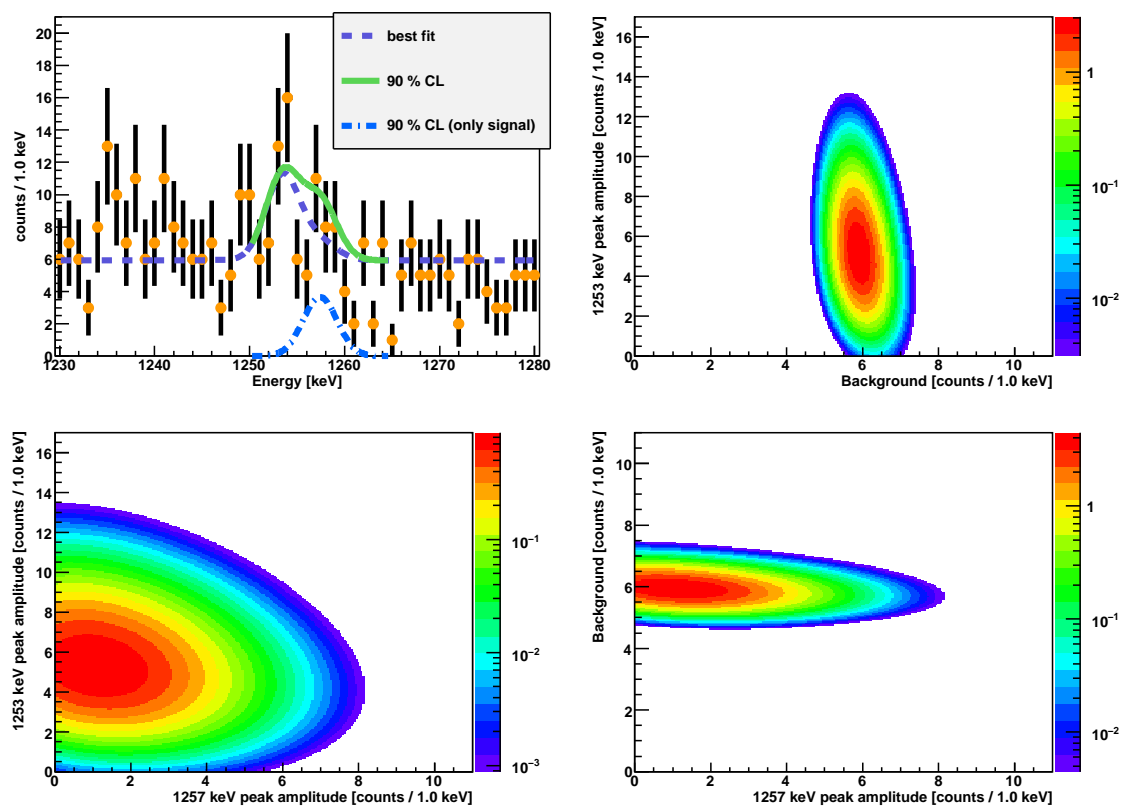


**Figure 4.18:** Example of fit for the case in which the 1253 keV peak was included in the background model. The fit shown in this figure was performed on the energy spectrum in which only the M2 cut was applied. An energy resolution of  $\sigma=1.8$  keV was used in the fit. The top left plot shows the data, the best fit (violet dashed line), the 90% C.L. limit (green continuous line) and the peak amplitude corresponding to the 90% C.L. limit (dashed-dotted blue line). The other three plots show the likelihood function in which one of the three variables was integrated over all the possible values.

Energy resolution	$\sigma = 1.6$ keV	$\sigma = 1.8$ keV	$\sigma = 2$ keV
M2	16.8	16.5	16.2
M2 + TotE	18.1	18.2	18.2
M2 + TotE + Dist	18.3	18.4	18.6
M2 + TotE + Dist + $E_{\gamma 1}$ + $E_{\gamma 2}$	4.9	5.3	5.6

**Table 4.9:** Limit on the number of counts (90% C.L.) under the 1257 keV peak for various sets of cuts and for various values of energy resolution. For all the combinations the fit was performed in the range 1230÷1280 keV.

Fit range	1240÷1280 keV	1230÷1280 keV	1230÷1270 keV
M2	18.7	16.5	14.9
M2 + TotE	20.6	18.2	16.3
M2 + TotE + Dist	20.7	18.4	16.3
M2 + TotE + Dist + $E_{\gamma 1}$ + $E_{\gamma 2}$	5.7	5.3	5.0

**Table 4.10:** Limit on the number of counts (90% C.L.) under the 1257 keV peak for various sets of cuts and for various ranges used in the fit. For all the combinations the standard deviation in the fit was fixed to  $\sigma=1.8$  keV.

1257 keV peak position	1257.0 keV	1257.41 keV	1258.0 keV
M2	17.0	16.5	15.5
M2 + TotE	18.8	18.2	17.1
M2 + TotE + Dist	18.8	18.4	17.7
M2 + TotE + Dist + $E_{\gamma 1}$ + $E_{\gamma 2}$	5.3	5.3	5.2

**Table 4.11:** Limit on the number of counts (90% C.L.) under the 1257 keV peak for various sets of cuts and for various values of the peak position. For all the combinations the standard deviation in the fit was fixed to  $\sigma=1.8$  keV and the fit was performed in the range 1230÷1280 keV.

1253 keV peak position	1253.0 keV	1253.5 keV	1254.0 keV
M2	17.8	16.5	15.2
M2 + TotE	19.4	18.2	16.9
M2 + TotE + Dist	19.7	18.4	17.1

**Table 4.12:** Limit on the number of counts (90% C.L.) under the 1257 keV peak for various sets of cuts and for various values of the 1253 keV peak position. For all the combinations the standard deviation in the fit was fixed to  $\sigma=1.8$  keV, the position of the other peak was fixed to 1257.41 keV and the fit was performed in the range 1230÷1280 keV.

## 4.8 Results

The analysis presented in this chapter allows to set a lower limit for the half life of  $2\nu\beta\beta$  decay mode of  $^{130}\text{Te}$  to the excited state  $0_1^+$  of  $^{130}\text{Xe}$ . The accumulated statistics is reported in tab. 4.5, while the detection efficiency for different event selection criteria is reported in tab. 4.8. The best limit is obtained using the selection cuts that impose separate constraints on the energy release of the two hits of an event. Using eq. (4.2), with a statistics of  $1.07 \times 10^{25} \text{ N}(^{130}\text{Te}) \cdot \text{y}$ , a 3% detection efficiency and an upper limit of 5.7 counts under the 1257 keV peak (tab. 4.10), the resulting limit on the half life is

$$T_{1/2} > 3.4 \times 10^{22} \text{ y (90\% C.L.)}. \quad (4.11)$$

In eq. (4.11) the efficiency has been multiplied by a factor 0.86 to take into account the relative intensity of the particular decay channel searched in the present analysis (see sec. 4.3).

A more conservative limit is obtained if the event selection criteria are used where no separate constraints are set on the two energy releases in each event. The most conservative case is the one in which the cuts **M2**, **TotE** and **Dist** are used: the efficiency for this pattern is 4.56% and the 90% C.L. limit on the number of counts under the 1257 keV peak is 20.7 (see tab. 4.10). The corresponding half life limit is

$$T_{1/2} > 1.4 \times 10^{22} \text{ y (90\% C.L.)}. \quad (4.12)$$



# Chapter 5

## The CUORE experiment

### 5.1 Introduction

Next generation double beta decay experiments aim at exploring the range of the effective neutrino Majorana mass corresponding to the inverted mass-hierarchy pattern. This will require a sensitivity on  $m_{\beta\beta}$  of few tens of meV, which is about one order of magnitude better compared to best present experiments. This ambitious goal will be achieved mainly by an increase of the  $0\nu\beta\beta$  isotope mass and by a strong reduction of the background level in the region of the energy spectrum where the signal is expected.

The CUORE experiment [46] will search for neutrinoless double beta decay in  $^{130}\text{Te}$  using an array of 988  $\text{TeO}_2$  bolometers, with a total mass of  $\sim 740$  kg. The feasibility of a ton scale bolometric detector has been widely demonstrated by CUORICINO and by its predecessor experiments. Compared to CUORICINO, the detector mass will be increased by a factor of twenty and the background will be reduced by about the same amount. The data taking of CUORE is foreseen to start in 2012: after five years an half life sensitivity of the order of  $10^{26}$  y is expected. Even if the mass increase will require much effort, mainly due to technological issues concerning the cryogenic apparatus, the biggest challenge will be the achievement of an adequately low background level. The goal of the CUORE collaboration is to reach a background of  $\sim 10^{-2}$  counts/(keV · kg · y) in the  $0\nu\beta\beta$  region: this corresponds to observing less than 1 count per crystal over 10 years in an energy window of 10 keV centered at the  $Q$ -value of the decay.

The working principles of bolometric detectors have been discussed in chapter 2 and the CUORICINO experiment has been presented in chapter 3. In this chapter the major changes that will be introduced in CUORE will be presented, with particular attention to the issues concerning the reduction of the background.

## 5.2 Overview

The CUORE experiment will be composed by an array of 988  $\text{TeO}_2$  bolometers with natural concentration of  $^{130}\text{Te}$  (34%). As for CUORICINO, the crystals will have a dimension of  $5 \times 5 \times 5 \text{ cm}^3$ , and mass of  $\sim 0.75 \text{ kg}$  each: the total detector mass will be of  $\sim 741 \text{ kg}$ , corresponding to  $\sim 9.4 \times 10^{26}$   $^{130}\text{Te}$  nuclei. The geometry of the CUORE detector is shown in fig. 5.1. The 988 bolometers will be arranged in a cylindrical structure organized into 19 towers. Each tower, very similar to CUORICINO, will be made 13 floors, each floor being composed by four crystals.

The closely packed structure of the CUORE array will take great advantage from the high background rejection capability that can be obtained by operating the detectors in anti-coincidence. Since there is a small probability for the two  $0\nu\beta\beta$  electrons to escape from the crystal where they are produced, a simultaneous hit in more than one detector is an indication of a background event. In contrast to CUORICINO, most of the crystals will be completely surrounded by other detectors, thus allowing an easier identification of crystal surface contaminations.

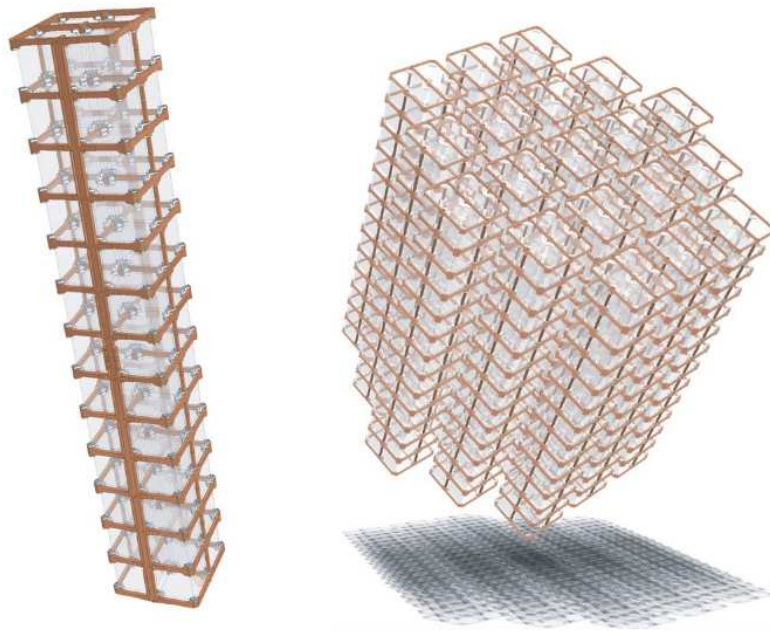


**Figure 5.1:** CUORE detector array.

CUORE will be operated underground, in the Hall A of the Laboratori Nazionali del Gran sasso (see fig. 5.2), where the 3400 m w.e. rock shield reduces the muon flux to  $\sim 3 \times 10^{-8} \mu\text{cm}^{-2}\text{s}^{-1}$  [61] and the neutron flux to  $\sim 10^{-6} \text{ n cm}^{-2} \text{ s}^{-1}$  [62].

As for CUORICINO, the thermal signals will be read by NTD Germanium thermistors developed at the Lawrence Berkeley National Laboratories (LNBL) and UC Berkeley department of Material Science [119].

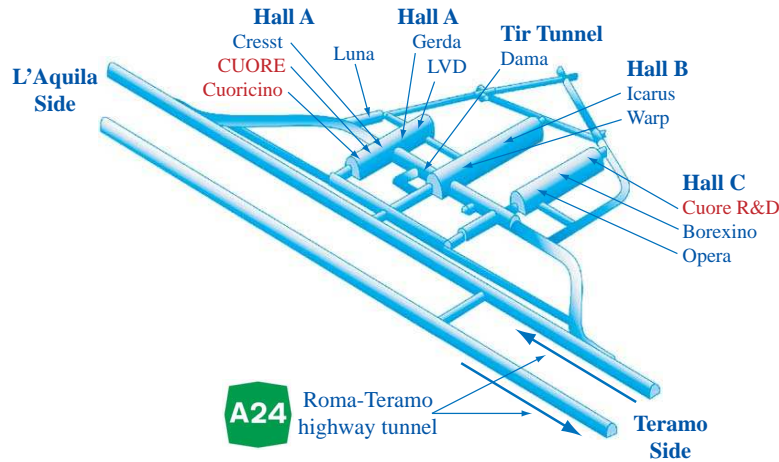


**Figure 5.2:** Map of the Laboratori Nazionali del Gran Sasso.

The entire array, surrounded by a 6 cm thick lead shield, will be operated at about 10 mK in a  $^3\text{He}/^4\text{He}$  dilution refrigerator. A further thickness of 25 cm of low activity lead will be positioned on top of the detector array in order to shield it from the materials in the dilution unit of the refrigerator and from the environmental radioactivity. A borated polyethylene shield will protect the detector from neutrons and an anti Radon air-tight cage will surround externally the cryostat.

Despite the biggest challenges of the CUORE experiment will be the mass increase and the reduction of the background, several other aspects of the detector have been revised in order to cope with the increased number of detectors.

For example the mechanical structure of the towers has been redesigned to allow a simpler assembling procedure and to guarantee better energy resolution and more uniformity in the response of different detectors.

Given the packed structure of CUORE, the energy calibration procedure had to be revised as well. While in CUORICINO the calibration sources could be positioned at room temperature, outside of the cryogenic apparatus, a uniform and fast enough calibration of the CUORE array will require to periodically insert the sources inside the cryostat, and therefore to cool them at 10 mK and warm them up again. The calibration system will have to introduce thermal loads that can be afforded by the cryogenic apparatus, and will have to guarantee a reliable operation during the whole live time of the experiment (about 10 years). Moreover the position of the sources, as well as their intensity will have to be optimized to reduce the loss in detector live time due to the calibration.

The analog part of the readout chain will be almost identical to the CUORICINO one, as it was already designed in the view of a bigger experiment. The main changes will be related to an improved automation, remote control and diagnostic tools.

The data acquisition system, that will be discussed in chapter 6, has undergone a complete redesign both in the hardware and the software. The main motivation for

the upgrade is to obtain a system able to integrate all the subsystems of the detector (cryogenics, electronics, signal digitization): this will simplify the online data quality and detector monitoring, as well as the offline analysis procedures.

### 5.3 Shieldings and cryogenics

Including the detector support copper structure and the radioactivity lead shieldings, the total mass to be cooled in CUORE will be of about 4 tons. Refrigerators with the required characteristics are technically feasible, as was demonstrated for example by the gravitational wave antenna experiments. However, because of the stringent radioactivity constraints, the CUORE refrigerator will have to satisfy several requirements that are rather uncommon in standard cryogenic devices.

The design must satisfy the following set of requirements:

- a base temperature lower than 10 mK must be reached for optimal detector operation;
- given the size of the detector array, an experimental space at least 1 m high and with an equal diameter is necessary;
- the cooling power of the refrigerator will have to account for the thermal load produced by the  $\sim 2600$  wires running from 10 mK to room temperature;
- the vibrations transmitted to the detectors must be minimized, as they would cause noise on the detectors and an increase in the average temperature of the entire array;
- the experience acquired with CUORICINO shows that the experiment must be properly shielded to reduce at a sufficiently low level the background coming from the  $^{232}\text{Th}$  contaminations in the cryostat thermal shields;
- for the same reasons, only selected radio-pure materials can be used inside the lead shielding;
- since CUORE is expected to collect data continuously for several years, further requirements come from the need for a stable, service-free and high duty-cycle apparatus.

The cryogenic apparatus is shown in fig. 5.3. The cryostat will be made of six nested vessels. The Outer Vacuum Chamber (OVC), maintained at room temperature, and the Inner Vacuum Chamber (IVC) maintained at about 4 K, will be separated by an intermediate radiation shield that will operate at a temperature of  $\sim 40$  K. Additional thermal radiation shielding will be provided by 30 layers of Multilayer Insulation (MLI) covering the 40 K shield and by 10 layers on the IVC shield, the amount of MLI being limited by radioactivity constraints.

The cooling of the IVC and of the 40 K radiation shield will be provided by five Pulse Tubes mounted on the room temperature OVC top flange.

The detector will be cooled by a  $^3\text{He}/^4\text{He}$  dilution refrigerator that is being especially designed for CUORE by Leiden Cryogenics. It is a DRS-2000 unit modified to run without cryogenic liquids: a Joule-Thompson heat exchanger will replace the functionalities usually provided by the 1 K pot. The expected cooling powers are  $>1.5$  mW,  $30 \mu\text{W}$  and  $5 \mu\text{W}$  at 120 mK, 20 mK and 12 mK respectively.

Inside the IVC there will be three thermal shields connected respectively to the Still ( $\sim 600$  mK), to the Cold Plate ( $\sim 50$  mK), and to the Mixing Chamber, which is the coldest point of the apparatus ( $\sim 10$  mK).

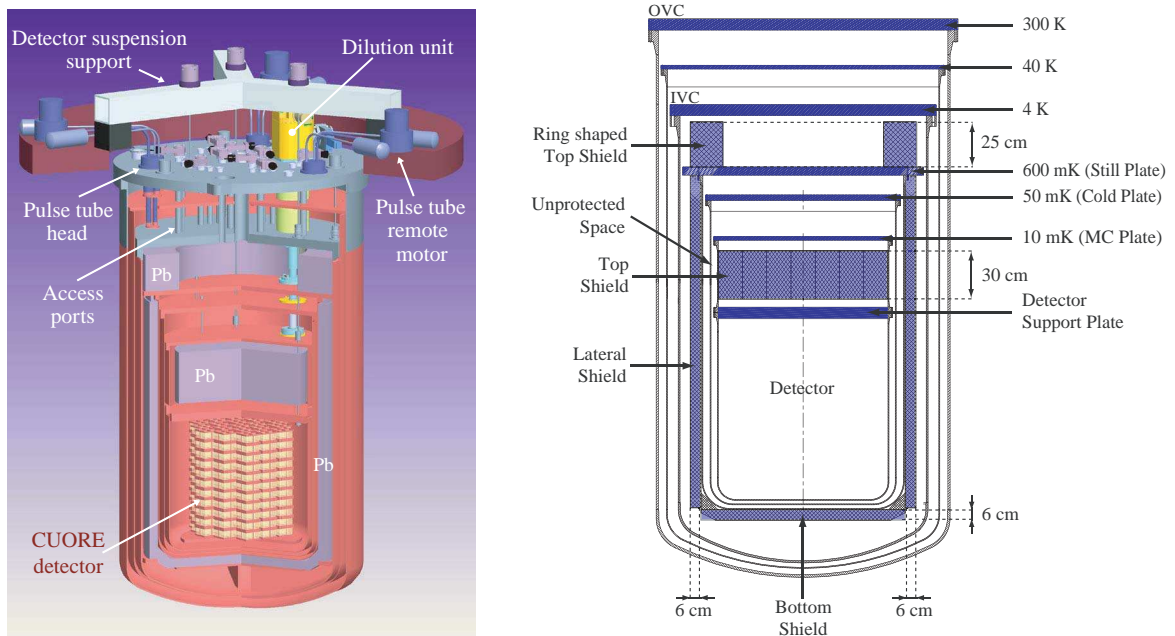


**Figure 5.3:** CUORE cryostat and internal shieldings.

Inside the cryostat there will be three lead shields to protect the experiment from environmental radioactivity and from contaminations in the building materials.

A 25 cm thick lead layer positioned outside the OVC will shield the detector from the bottom and from the sides. An equivalent shielding from the top will be hosted inside the cryostat, just above the detector. It will be placed between the mixing chamber plate and the detector, but it will be thermally linked to the 50 mK radiation shield (Cold Plate). With a thickness and a diameter of 30 cm and 90 cm respectively, this shield will weight about 3300 kg. A lead ring-shaped shield placed on the Still flange will close the gap between the lead disk above the detector and the outer room temperature shields. An additional shielding of detector sides and bottom will be provided by a 6 cm lead layer ( $m \simeq 5400$  kg) just outside the Still shield.

To accomplish the radio-purity requirements, the cryostat radiation shields are made

of selected high purity copper that has been already stored underground to prevent cosmic ray activation and will be brought to surface only for building the cryostat.

The cold lead disk above the detector and the detector itself are supported by two independent mechanical structures. The lead is supported by three rods extending from the OVC top plate. The detector suspension has been designed to minimize the transmission of mechanical vibrations produced by seismic noise and by the operation of cryocoolers and pumps. In the horizontal direction the structure acts as a pendulum with a natural frequency of about 0.4 Hz, while in the vertical direction a two stages frequency isolator serves as a low-pass filter with two poles at about 0.5 and 3.4 Hz.

## 5.4 From the single module to the CUORE array

The 988 bolometers composing the CUORE detector will be grouped into 19 towers very similar to the CUORICINO one. Even if the CUORICINO structure has proved to be reliable both from the mechanical and thermal point of view, several improvements have been introduced in the design of the CUORE towers. These changes will produce a simplification of the tower assembling procedures, as well as a more uniform response of different detectors. Moreover a sensible reduction in the amount of copper used to hold the crystals will be achieved with the new design.

The assembly of the single bolometer will benefit from the introduction of new gluing and wiring procedures. As already discussed in chapter 3, the NTD sensors and the Si heaters are coupled to the crystals by mean of a low radioactivity two components epoxy glue. As shown in fig. 5.4 the glue must be deposited in nine separate spots and a spacing of about 50  $\mu\text{m}$  must be left between the crystal and the sensor to avoid excessive stress caused by differential thermal contractions. In CUORICINO this operation was performed manually: using a dedicated tool composed by an array of 9 pins, the glue spots were deposited on the NTD surfaces and afterwards the sensors were coupled to the crystals using a spacer to obtain the 50  $\mu\text{m}$  gap. However, since this procedure revealed to be time consuming and not appropriate to deal with 1000 crystals, an automatic tool will be employed for the gluing of the CUORE bolometers. Besides being faster and more reliable, the new approach will give the possibility to glue the sensors after the entire tower has been assembled. This feature will allow to easily recover possible broken wiring connections and unsuccessful gluings without dismounting the whole tower.

In CUORICINO the NTDs could be glued on the crystals only after that the bonding of the golden wires used for signal readout was performed. The order of these operations was constrained by the position of the golden-pads that provide electrical contact to the wires, deposited on the opposite faces of each thermistor. In CUORE a possible simplification could be obtained if the gold pads will be deposited on the upper face of the thermistors (see fig. 5.5). In this way, the order of the assembly procedure can be inverted by making wire-bonding the last step. This could lead to a simpler,

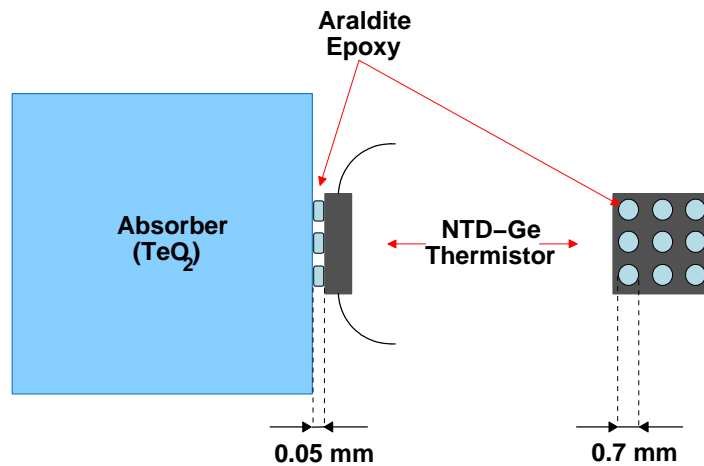


**Figure 5.4:** Sensor gluing on the  $\text{TeO}_2$  crystals. The glue is deposited on the sensor in nine separate spots in order to avoid excessive stress caused by differential thermal contractions between the crystals, the NTD and the glue itself.

faster and more reliable wiring. Such thermistors, called Flat-pack NTDs, are currently undergoing cryogenic performance tests.



**Figure 5.5:** Different position of golden pads in the CUORICINO-like (left) and flat-pack (right) NTD thermistors. In contrast to the CUORICINO case, the flat pack option allows to bond golden wires for detector readout when the thermistors are already glued on the crystals.

In CUORICINO each group of four crystals was held together by a pair of copper frames, and this single module was replicated as many times as the number of floors in the whole tower. As shown in fig. 5.6, in the new design the same copper frame will serve both as a top frame for a given floor and as a bottom frame for the following one. This simple modification not only facilitates the assembling procedure, but also guarantees a reduction of about 50% in the amount of copper needed for the mechanical structure: as discussed in sec. 3.8 copper contaminations are responsible for one of the most important contributions to the CUORICINO background.

Other improvements in the mechanical structure of the tower are related to a modification in the shape of the Teflon supports used to hold the crystals. Compared to CUORICINO, in the new design the vertical dimension of the supports has been increased to compensate the differential thermal contractions between the crystals and the copper structure, and the contact surface with the crystals has been increased to

provide better reproducibility in the thermal contacts and thus a more uniform response of different detectors.

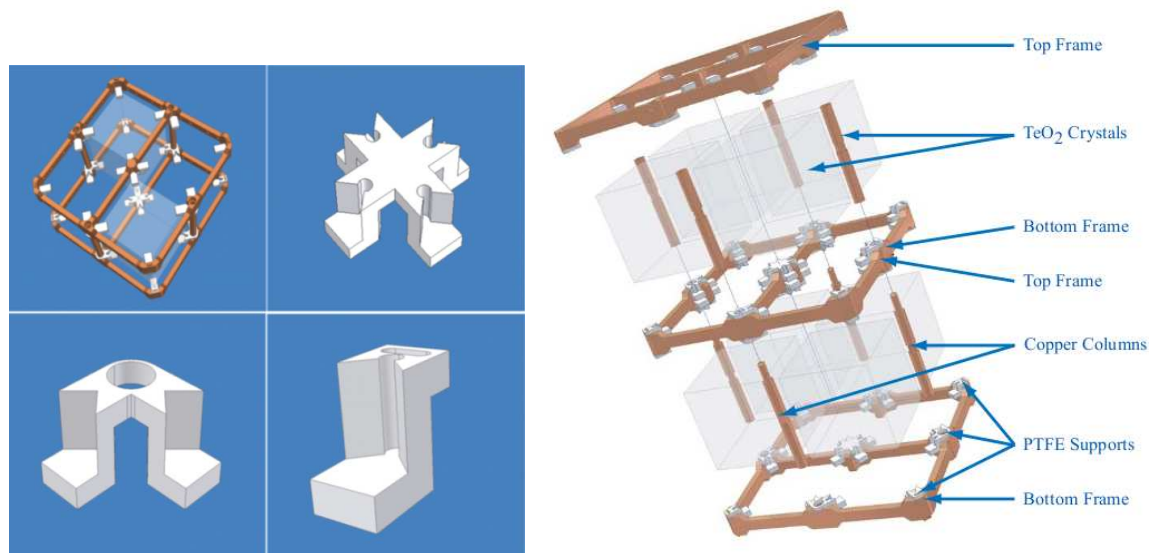


**Figure 5.6:** Mechanical structure of the CUORE tower. On the left picture a single floor is shown together with the different shapes of the Teflon support used to hold the crystals. The right side picture shows how the multiple floors composing one CUORE tower will be assembled together.

In order to avoid material recontaminations, all the assembling procedures will be performed in a nitrogen fluxed environment and using custom designed glove boxes that will allow to avoid any direct contact with the detector materials. For this purpose a dedicated clean room is being built within the CUORE hut, as well as a clean area to store the materials in the time between their arrival at the LNGS and the assembly of the towers. Because of the big number of crystals that will have to be assembled, great care was also taken to define a procedure as much *error-free* as possible. It will involve not only the construction of the single towers but also all the movimentations that will take place from the the beginning of the assembly to the mounting of the completed towers into the cryogenic apparatus.

## 5.5 Background Reduction for Cuore

It was discussed in chapter 3 that the main contributions to the CUORICINO background in the  $0\nu\beta\beta$  region are produced by  $^{232}\text{Th}$  contaminations in the cryostat radiation shields and by surface contaminations in the crystals and in the copper used for the mechanical structure of the tower. While the background coming from  $^{232}\text{Th}$  is rather understood and will be easily reduced by the 6 cm thick lead layer that will be positioned outside the 600 mK radiation shield, the contaminations in crystal and copper surfaces have a less clear signature and represent the main obstacle towards the

achievement of the background level of  $10^{-2}$  counts/(keV · kg · y) foreseen for CUORE. For these reasons much effort was spent within the CUORE collaboration to understand such background sources and to find a way to eliminate them.

Great part of this work was done using the R&D facility in the Hall C of LNGS. The experimental setup is composed by a cryogenic apparatus similar to the CUORICINO one, but with a smaller space for the detectors: two or at most three CUORICINO-like floors can fit into it in each test measurement. Even if proper shieldings are present to reduce the background from environmental  $\gamma$ s and muons, the Hall C apparatus has a quite high  $^{232}\text{Th}$  contamination in the radiation shields. As a consequence the background in the  $0\nu\beta\beta$  region, which is on the left side of the 2615 keV  $^{208}\text{Tl}$  peak from the  $^{232}\text{Th}$  chain, is rather high compared to CUORICINO. Nevertheless the Hall C apparatus is well suited for the investigation of the continuous background in the 3-4 MeV region, above the  $^{208}\text{Tl}$  line, which is the most interesting region to look at.

### 5.5.1 The RAD Measurements

The Radioactivity Array Detector (RAD) is a small array composed by eight  $5 \times 5 \times 5 \text{ cm}^3$   $\text{TeO}_2$  bolometers specifically constructed in 2004 to investigate the features of the background observed in CUORICINO (see fig. 5.7).

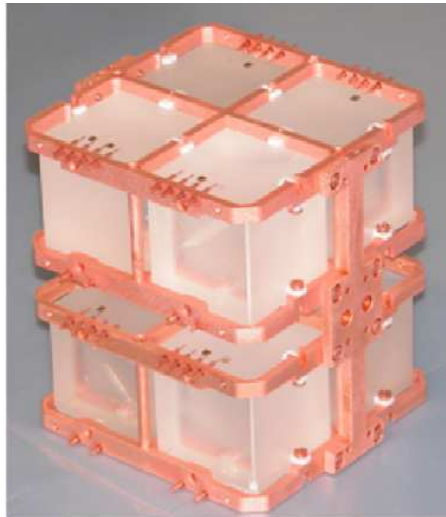


**Figure 5.7:** The RAD detector used for background investigations in the Hall C R&D apparatus.

The first RAD measurement (RAD1) was prepared in 2004: it had the main goal to test a better crystal surface cleaning procedure. The radioactive content of all the materials close to the detectors was previously measured using Inductively Coupled Plasma Mass Spectrometer (ICPMS) and the High Purity Germanium (HPGe) detectors available at LNGS. The crystals were etched with ultra-pure nitric acid to remove

about  $10\ \mu\text{m}$  from the surfaces and were then polished with a  $\text{SiO}_2$  powder. The copper structure was etched and subsequently treated with electro erosion, removing between 10 and  $30\ \mu\text{m}$  from the surfaces.

The RAD1 test was quite successful (see fig. 5.8). The extremely low background allowed to disentangle the bulk and surface contaminations of the crystals: the disappearance of the low energy tail in the  $\alpha$  peaks, a typical feature of surface contaminations (see the discussion in sec. 3.8.2), demonstrated that the crystal surface cleaning procedure was effective. As a consequence the RAD1 measurement allowed to identify the bulk contaminations (the sharp Gaussian peaks) of the crystals much clearly than CUORICINO: there is no evidence of Uranium in secular equilibrium, while there is a contamination in Thorium. However no improvements were obtained in this test for the 3-4 MeV continuous background, which resulted to be comparable to the one observed in CUORICINO.

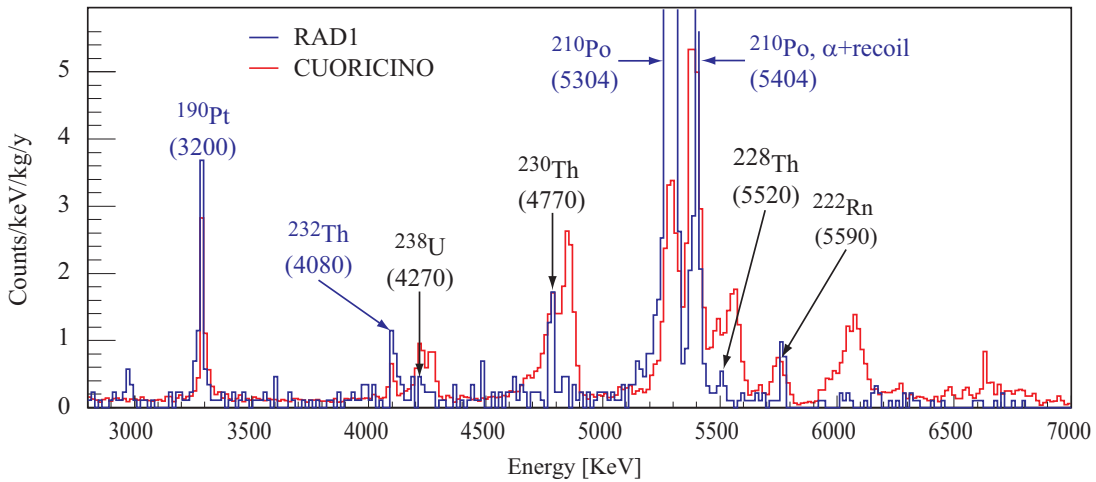


**Figure 5.8:** Background spectrum in the RAD1 Hall C test (blue histogram) compared to CUORICINO (red histogram).

The RAD2 test was dedicated to the investigation of radioactive contaminations of the small parts facing the detectors. Even if the crystals and the copper structure are by far the most important contributions in the total mass, some other materials are present in the vicinity of the detectors: the NTD sensors, the Si heaters, the gold wires used for signal readout and the Teflon supports. Possible contaminations in the NTD sensors were excluded, because an energy release in their internal would produce easily identifiable fast pulses, as a consequence of the fact that the thermalization process does not have to go through the glue spots used to couple the sensors to the crystals. In the RAD2 test an amount these small parts much bigger with respect to CUORICINO was put close to the detectors in order to investigate their contribution to the background. The amount Teflon, Si heaters and gold wires *seen* by RAD2 was increased respectively by 6, 80 and 169 times with respect to CUORICINO. Since the

event rate measured in the RAD2 test between 3 and 4 MeV was compatible with the one measured by RAD1 and CUORICINO, it was possible to evince that the maximum contribution from the small parts is 1% for the Si heaters, 3% the gold wires and 50% for Teflon.

Since a sensitive reduction of the counting rate between 3 and 4 MeV was not achieved in the first two RAD measurements, two possible explanations were taken in consideration to explain the observed background: either it is produced by surface contaminations in the copper structure, or it is not caused by radioactive contaminations in the materials close to the detectors, but it is due to some other process releasing energy in the 3-4 MeV continuum.

The first possibility (copper surface contaminations) was investigated in the RAD3 measurement, in which the copper structure of the RAD detector was covered with a  $60\mu\text{m}$  thick polyethylene layer. Since the polyethylene is so thin, there is no distinction between bulk and surface contaminations. This feature allowed to perform fast and reliable measurement of the contaminations in this material using the standard HPGe detectors available at LNGS. The result of RAD3 was a strong reduction of the 5.3 MeV peak, which became in this run compatible with the CUORICINO one, while the 5.4 MeV peak remained almost unchanged with respect to the previous RAD tests. This proved that the 5.3 MeV peak is produced by contaminations in the copper surfaces while the 5.4 MeV peak is due to  $^{210}\text{Pb}$  contaminations within the crystals.

Another test (RAD4) was performed with the same detector of RAD3, but a neutron shield was introduced outside the cryostat. Since the results of RAD4 were compatible with those of RAD3, it could be concluded that neutrons do not contribute significantly to the background in the 3-4 MeV continuum.

Since the spectra of RAD3 and RAD4 were compatible to each other, they were summed together to improve the statistics (see fig. 5.9). From the overall analysis of these two runs it could be concluded that the polyethylene film yielded a background reduction in the 3-4 MeV continuum by a factor of  $2\pm 0.4$  with respect to CUORICINO and RAD1.

Two radioactivity tests, RAD5 and RAD6, were devoted to the investigation of possible *exotic* events produced by the Teflon supports holding the crystals. These test were based on the hypothesis that, due to thermal contractions, some relaxation process could occur within the structure of the Teflon supports that could produce heat releases able to mimic the thermal pulses produced by particle interactions. For this purpose in the RAD5 and RAD6 runs the Teflon supports were replaced by phosphorus-bronze clamps, as shown in fig. 5.10. The choice of this particular alloy was dictated by its elastic properties, which were needed to guarantee a good mechanical coupling with the crystals. Since the RAD5 measurement showed that the phosphorus-bronze clamps contained an excessive concentration of  $^{210}\text{Pb}$ , another measurement (RAD6) was carried out in which a thin copper layer was deposited on the clamps surfaces. In order to check for possible contaminations in the copper layer itself, two of the RAD6 crystals were faced to a copper foil as thick as the deposition on the clamps

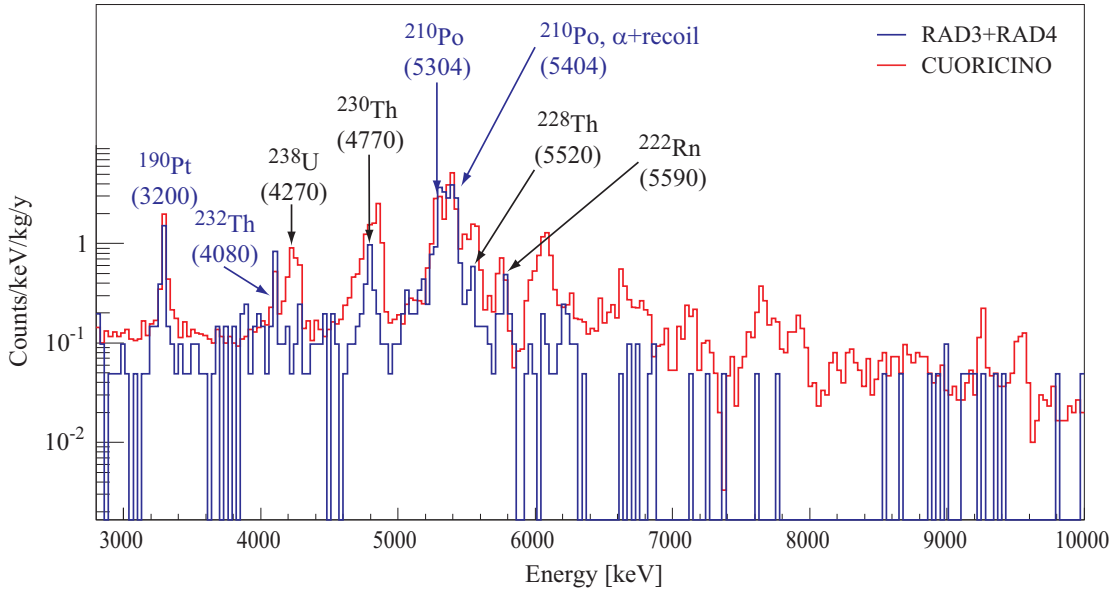


**Figure 5.9:** Background spectrum in the RAD3+RAD4 Hall C tests.

(about  $50 \mu\text{m}$ ). The RAD6 measurement showed a lower contamination level with respect to RAD5, but a higher background level if compared to the previous RAD tests. Moreover, a comparison of the spectra of the crystals facing the copper foils with the spectra of the other crystals, showed an excessive surface contamination in the copper layer itself. As a consequence the RAD5 and RAD6 tests could not rule out the possibility that part of the background between 3 and 4 MeV is produced by non radioactive contributions due to thermal relaxations in the Teflon supports.

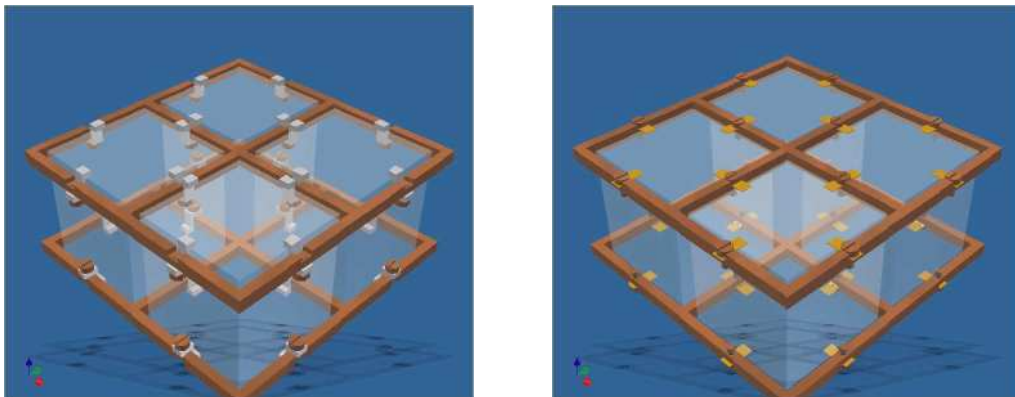


**Figure 5.10:** Comparison between the standard (left) and the Teflon-free (right) RAD detector.

With the RAD tests it was proved that surface contaminations in the copper structure play a relevant role in the background between 3 and 4 MeV. This conclusion arises from the comparison of the RAD1 spectrum with the RAD3+RAD4 spectrum.

In RAD1 the counting rate between 3 and 4 MeV was similar to CUORICINO, while in RAD3+RAD4, where the only difference was the coverage of the copper structure with the polyethylene foils, the background in the same region is reduced by about a factor of two. Moreover an effective and reproducible crystal surface procedure was obtained in these tests. This is proved by the disappearance in RAD1 of the low energy tails in the  $\alpha$  peaks with respect to CUORICINO. The RAD5+RAD6 tests could not rule out possible contributions to the background from non-radioactive sources, but demonstrated the good thermal performance of the detectors even when the Teflon supports are replaced by metallic clamps.

### 5.5.2 Surface sensitive bolometers

Besides the optimization of surface cleaning procedures another complementary approach has been developed in parallel to better understand the CUORE and CUORICINO background. It consists in the introduction of sensitive elements that cover the whole surface of the of the crystals. In the assumption that the observed background has its origin from outside the detectors, these devices should act as active shields, both protecting the core bolometers and producing a measurable signal.

The working principles of Surface Sensitive bolometers [120] (SSB) is shown in fig. 5.11. The thin slabs used as shields are thermally coupled to the main absorber by mean of glue spots and are provided with a sensor for signal readout. Due to the small thermal conductance between the slabs to the main absorber, pulses of different shapes are produced depending on whether an energy release occurred in the main absorber or in the surface elements.

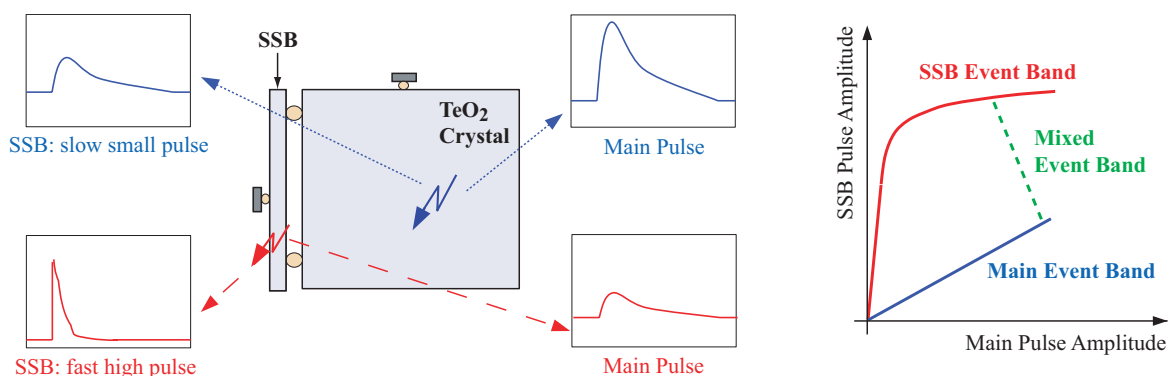


**Figure 5.11:** Principles of operation of surface sensitive bolometers (SSB).

Surface sensitive bolometers were operated in two different runs in the Hall C apparatus. The SSB performance in the two tests is summarized in fig. 5.12. Figure 5.12(a) shows the scatter plot of the signal amplitudes of the events observed in coincidence by the slabs and by the main absorber. There is a clear separation between the internal and external events. The red dots, representing those events in which part of the

energy was released within the slabs, could be easily recognized thanks to the different pulse shape. As shown in fig. 5.12(b), by looking at the decay time of the event in the main absorber it is possible to disentangle between surface and bulk events. This characteristic permits to operate the SSB without the need to read the signals produced in the slabs: besides reducing the complications in the assembling procedure, this feature would allow a reduction in the number of wires and thermistors.

Despite the Hall C tests demonstrated the scientific potential of surface sensitive bolometers, some technical problems arose during the measurements that did not allow to gain further informations on the possible background sources that are responsible for the continuous spectrum between 3 and 4 MeV observed in the previous radioactivity tests. Moreover, it turned out from the Hall C tests that these devices still require some development, therefore it is unlikely that they will be used in CUORE.

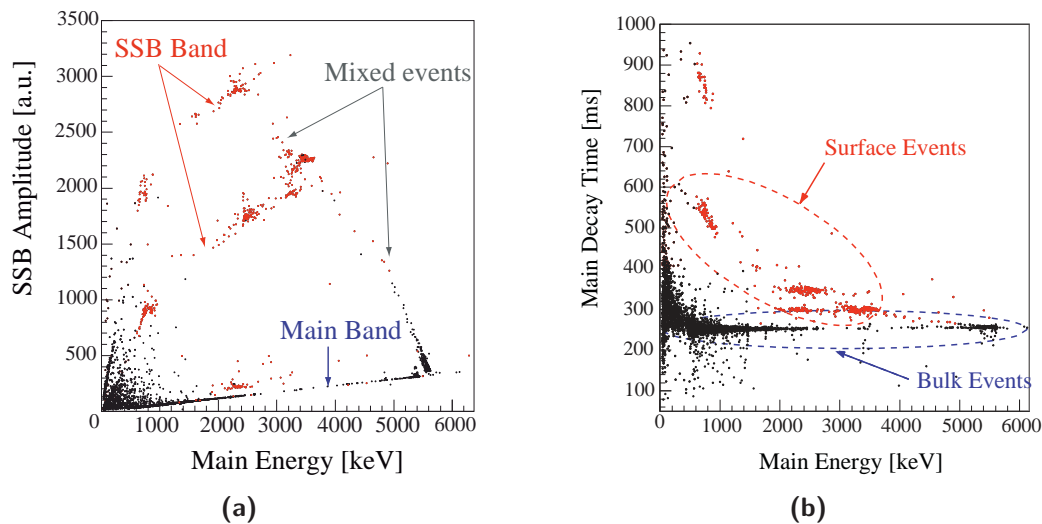


**Figure 5.12:** Scatter plots illustrating the performance of surface sensitive bolometers. The left plot shows the signal amplitude in the main absorber versus the signal amplitude in the surface elements. The red dots represent those events in which part of the energy was directly released within the surface sensitive elements. Such events could be easily distinguished because of the faster rise time of the pulses. The right side plot shows the signal amplitude versus the decay time in the main absorber. Also in this case the red dots represent the events in which part of the energy was directly released in the surface detectors. The presence of separated bands for the decay time allows to distinguish surface events from bulk events by looking at the pulse shape produced in the main absorber only.

# Chapter 6

## CUORE data acquisition system

### 6.1 Introduction

A relevant part of this PhD work was devoted to the development, testing and validation of the data acquisition system for the CUORE experiment. Even if the new system will share several characteristics with the one of CUORICINO, many innovations will be introduced to deal with the bigger number of detectors foreseen for CUORE. These are mainly related to a better integration of the various subsystems of the apparatus, as well as to the automation of the detector start-up procedures, that cannot be carried out manually on about 1000 channels.

In the first part of this chapter the general requirements to be satisfied by the new system will be discussed. After a description of the new DAQ hardware components and of the software developed to operate them, the discussion will be focused on the validation measurements performed on real detectors, and on the upgrade of the DAQ system of CUORICINO and of the Hall C R&D apparatus. In the last part of the chapter the bolometric tests of an automatic procedure for the detectors characterization will be presented.

### 6.2 DAQ system requirements

The core of the CUORE data acquisition system was designed keeping in mind the main features of the signals to be recorded, which will be summarized in the following.

With a frequency bandwidth extending up to about 12 Hz, the typical rise time of bolometric signals is of the order of few tens of ms, while decay time about one order of magnitude bigger (see fig. 6.1). A sampling frequency of few hundreds of Hz is therefore adequate to properly reconstruct the signals from all detectors (in CUORICINO the typical value for this parameter was 125 Hz).

To minimize the common mode noise, mainly affecting the very first part of the readout chain, the thermal pulses are acquired in a differential configuration, with the

two poles of the signal,  $V_+$  and  $V_-$ , symmetric with respect to the ground. Even if the overall signal amplitude ( $V = V_+ - V_-$ ) is in the range  $0 \text{ V} \div 10 \text{ V}$  during standard measurements, the possibility to acquire signals in the symmetric range  $-10 \text{ V} \div 10 \text{ V}$  must be foreseen by the DAQ system, as this feature is necessary during the detector characterization procedure (see sec. 6.7).

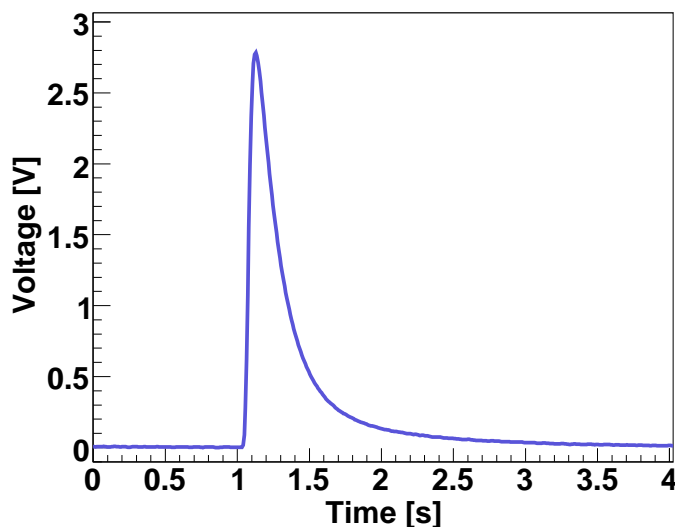


**Figure 6.1:** Example of bolometric pulse at the input of the digitization stage.

The digitizing boards should have an adequate resolution to avoid any kind of deterioration in the acquired signals. The energy resolution of the best CUORICINO detectors in the  $0\nu\beta\beta$  region is of 4 keV (FWHM), and an even better resolution is achieved at low energy, less than 1 keV. In the conservative assumption of 20 MeV full scale energy range, an ADC with at least 16 bit resolution must be used to guarantee an adequate reconstruction of the digitized signals.

Bolometric pulses are subject to a rather wide spread in the shape and amplitude if compared to signals from other detectors. As a consequence the electronics and data acquisition system must foresee the possibility to select independent configuration parameters for each channel. Specifically concerning the last stages of the acquisition chain, this corresponds to the possibility to select independently the sampling frequency, the trigger thresholds and the duration of the saved time window upon the arrival of a pulse. This last parameter must be long enough to allow the detector to recover the base temperature after particle interactions, which is needed for proper reconstruction of the relevant frequency components of the pulses, as required by the application of the optimum filter technique (see chapter 3). The typical duration of the acquired time window is of about five seconds, including one second of pre-trigger, which is used to evaluate the detector temperature at the time when the pulse was detected.

## 6.3 Data acquisition hardware

After investigating the possibility of developing custom data acquisition boards [121], the CUORE collaboration decided to adopt commercial devices provided by National Instruments. This solution allowed to reduce the costs and to avoid all the complications related to the mass production of the custom data acquisition boards.

Several similar boards were taken in consideration, all of them belonging to the family of M-series multifunctional DAQ. Such boards are characterized by a 18-bit resolution analog to digital converter (ADC) and have a programmable sampling frequency up to 500 kSamples/s. They have a calibration circuitry to correct gain and offset errors: an internal reference signal ensures high accuracy and stability over time and temperature changes. A multiplexer is exploited to digitize the signals from many channels in parallel using a single ADC. An analog circuitry is present in the input stage of the boards (see fig. 6.2): it allows to select between differential and single-ended signals, select input ranges from  $-0.1 \text{ V} \div 0.1 \text{ V}$  up to  $-10 \text{ V} \div 10 \text{ V}$ , and toggle the status of the anti-aliasing filter (cutoff frequency at 40 kHz or 750 kHz).

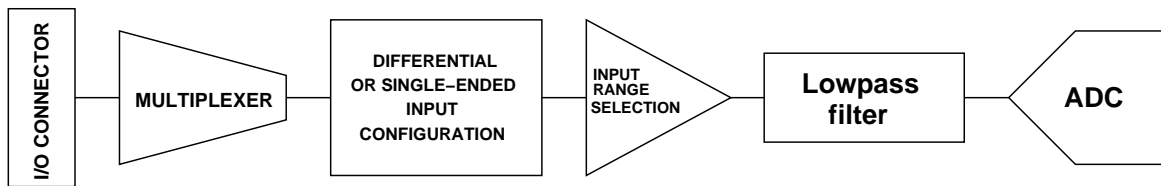


**Figure 6.2:** Analog circuitry at the input stage of the National Instruments M-series DAQ boards.

Several analog output channels, as well as digital I/O lines are available, and a variety of trigger signals can be imported or exported. The boards have an internal clock with a base frequency of 80 MHz, but can also accept an external clock signal. Various boards differ in the number of channels (analog input, analog output, digital I/O). All the requirements discussed in the previous section, concerning the sampling frequency, the resolution and the input range of the ADC are widely satisfied by the National Instruments M-series DAQ boards. In addition the presence of the analog output and digital I/O lines can reveal an useful resource for extending the basic functionalities of the system.

The boards are hosted in a chassis implementing the PXI standard<sup>1</sup>. A back-pane provides the possibility to route signals and to share a common clock source. Several chassis of different sizes are available, able to host up to 14 boards. Different kinds of boards can be mixed in the same chassis, thus providing the possibility to integrate in the core DAQ the various subsystems of the apparatus, such as cryogenic parameters monitoring and control.

The communication between the PXI chassis and the data acquisition computers is provided by a controller interface (NI PXI-PCI8336) implementing a communication

<sup>1</sup>The specifications of the PXI standard can be found on the website <http://www.pxisa.org/>

protocol over an optic fiber, which guarantees high data transfer rate and complete electrical isolation between the experimental apparatus and the acquisition computers.

The exact board and chassis models that will be used in CUORE have not been decided yet. The best devices will be chosen based on the optimal load balancing of the system and on the required number of auxiliary analog output and digital I/O lines. A reasonable guess can be made assuming boards with 16 channels hosted in chassis with 8 free slots: a total amount of 8 chassis and an equal number of data acquisition computers would be necessary to record the signals from 1000 channels.

At present two different boards have been tested, the NI PXI-6281 and the NI PXI-6284, which were hosted in the 6 slots PXI-1036 chassis. The former has 8 differential AI channels (or 16 single-ended), two analog output channels and 24 digital lines, while the latter has 16 differential AI channels (or 32 single-ended) and 48 digital lines.

Preliminary tests were performed on these devices using standard laboratory instruments. The ADC resolution was checked with a 1.5 V battery, used as input for a differential AI channel. Using an input range for the ADC between -10 V and 10 V and a sampling frequency of 1 kHz the distribution shown in fig. 6.3 was obtained for the signal amplitude. The RMS of the distribution corresponds to less than 0.8 LSB, thus validating the resolution of the ADC.

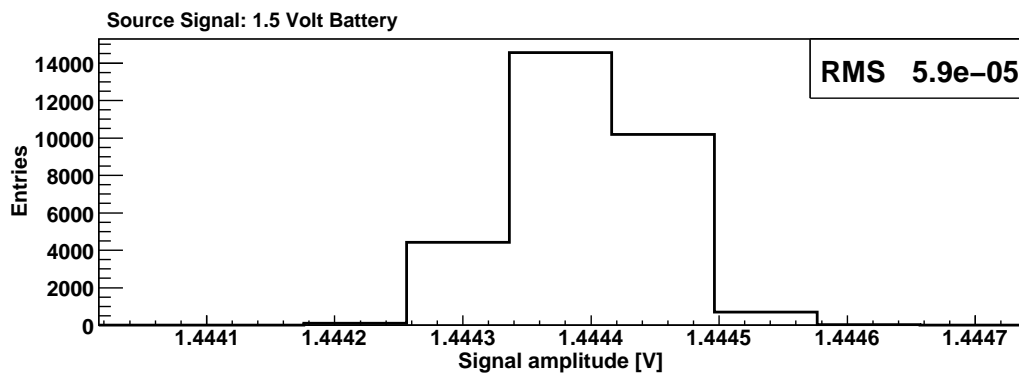


**Figure 6.3:** Check of the ADC resolution using a 1.5 V battery. The ADC input range used in this measurement was  $-10\text{ V} \div 10\text{ V}$ . The RMS value of the distribution corresponds to about 0.8 LSB.

Possible presence of cross talk between adjacent channels was checked by feeding one of the AI channels in the board with a 80 Hz sinusoidal signal produced by an arbitrary function generator. All other channels were closed on a  $50\ \Omega$  resistance, and were acquired with a sampling frequency of 500 Hz. As shown on the left plot in fig. 6.4, an evident presence cross talk was found at a first glance. However this problem was easily solved by a proper optimization of the DAQ boards programmable parameters. The cross talk was caused by the analog signal conditioning circuitry that is present in front of the ADC (see fig. 6.2). In order to perform an accurate measurement, this circuitry requires some settling time when the multiplexer switches from one channel to another. Moreover, the settling time is highly increased when the anti-aliasing lowpass

filter is switched on (i.e. the cutoff frequency is set to 40 kHz). This is clearly visible by comparing the left and right side plot in fig. 6.4: the only difference in the two measurements was the status of the lowpass filter, which was switched on in the left plot, and was switched off in the right plot. When the filter is switched off the settling time is short enough to provide an accurate measurement, and the residual signal from the channel connected to the arbitrary function generator is no more visible on adjacent channels.

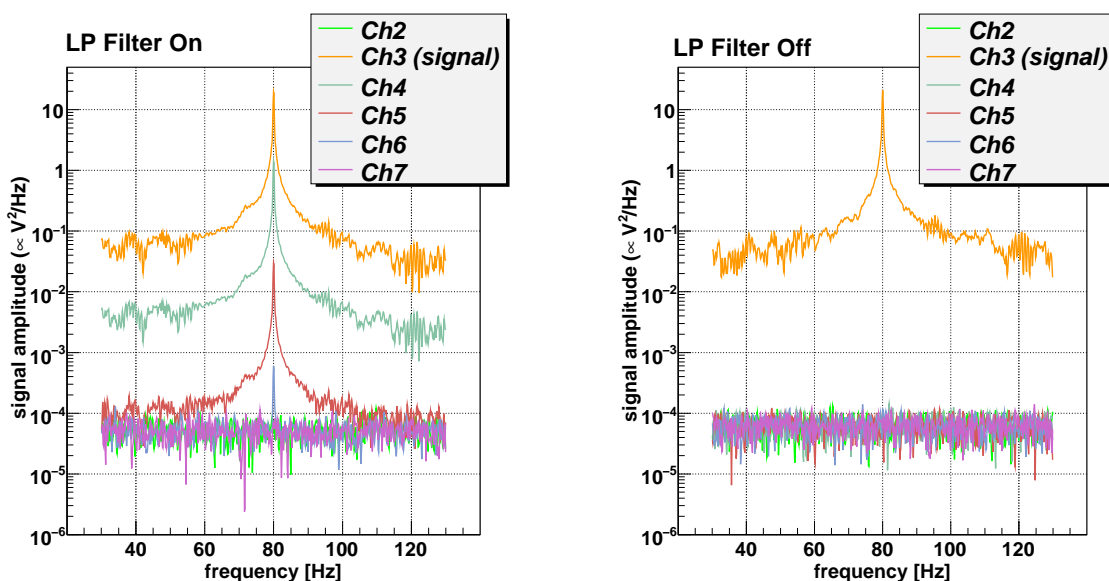


**Figure 6.4:** Effect of the low-pass filter on the crosstalk of adjacent channels. A 80 Hz sinusoidal signal was sent as input on channel 3 when all channels from 2 to 7 were acquired with a sampling frequency of 500 Hz. The two plots show the signal amplitudes in the frequency domain for all the acquired channels when the low-pass filter was active (left) and inactive (right).

The cross talk problem was solved by maximizing the conversion period, namely the time interval between two consecutive samplings on adjacent channels. By default the National Instruments boards use a rather small value for this parameter, about 15  $\mu$ s. However the conversion time can be increased, provided that the total time necessary to scan all acquired channels remains shorter than the sampling period, namely the time interval between two consecutive samplings on the same channel. The maximum allowed conversion period can be obtained by dividing the sampling period by the number of acquired channels. This is shown in fig. 6.5, where the default operation mode of the DAQ boards is compared to the operation mode in which the conversion period is maximized (usually referred as *round robin*).

Figure 6.6 summarizes the cross talk measurements performed after the adoption of the *round robin* operation mode. It shows, for several sampling frequencies between 1 kHz and 15 kHz, the ratio between the frequency domain signal amplitudes of two channels, 3 and 4, when the former was connected to a sinusoidal signal, and the

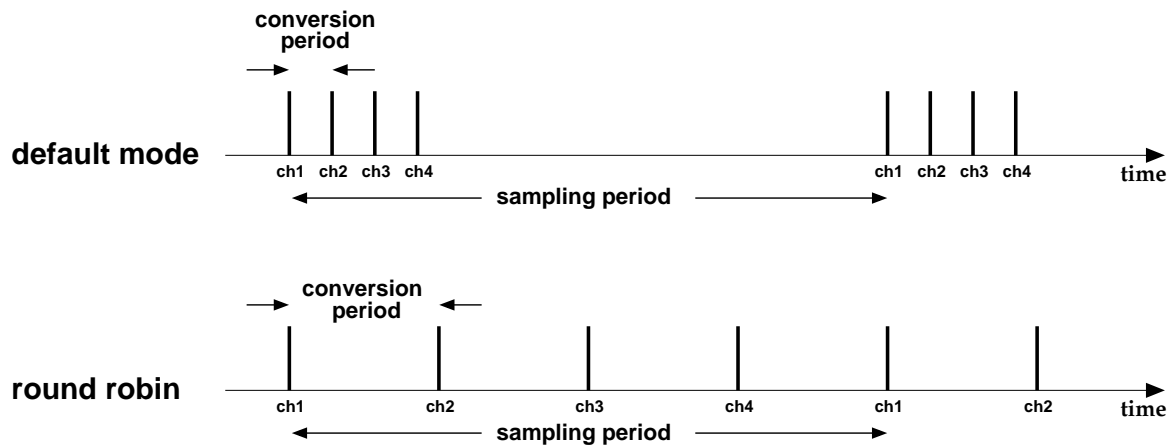


Figure 6.5: Illustration of the round robin sampling mode.

latter was closed on a  $50 \Omega$  resistance. In the case in which the lowpass filter was switched off the cross talk is negligible for sampling frequencies up to 15 kHz, while in the case in which it was switched on, accurate measurements could be performed only with sampling frequencies up to 2 kHz. Since eight channels were acquired in the measurements shown in fig. 6.6, it can be concluded that the minimum conversion period which allows proper settling of the analog input circuitry is of about  $60 \mu\text{s}$  when the lowpass filter is active. Despite a maximum sampling frequency of 2 kHz (actually 1 kHz for the NI PXI-6284 boards, that have 16 channels) is fairly adequate for the CUORE bolometers, higher sampling frequencies could be used as well, provided that a lower number of channels is acquired from each DAQ board.

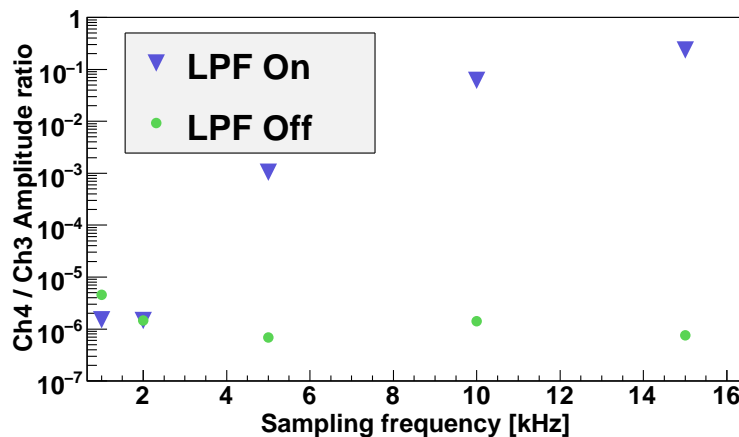


Figure 6.6: The plot shows the ratio between the signal amplitudes of two adjacent channels for various values of the sampling frequency when the low-pass filter was active (triangles) and inactive (dots). In the measurements channel 3 was connected to a 80 Hz sinusoidal signal while all other channels (also channel 4) were closed on a  $50 \Omega$  resistance.

## 6.4 Apollo: the data acquisition software

The CUORE data acquisition and slow control software, called **Apollo**, is designed with an high level of modularity, to provide an easy way to scale the number of acquired channels, and to allow smooth integration with the various subsystems of the experimental apparatus.

Written in the C++ programming language, **Apollo** is almost completely a custom software, the only exceptions being the National Instruments drivers used to interface with the DAQ boards, and the ROOT<sup>2</sup> software package, used for online data quality monitoring and for data storage.

**Apollo** is composed by several processes distributed over different computers running Scientific Linux, an operating system specifically developed at CERN and Fermilab for scientific purposes. Communication and data transfer between different processes occur via standard network connections. Besides providing flexibility and scalability, the choice of using a distributed system was dictated by the possibility to exploit standard and cheap computing resources.

All the **Apollo** processes can access the CUORE database, which is used to store the geometric description of the apparatus, the mappings and the settings of the various readout components, informations concerning the performed measurements, as well as relevant quantities evaluated in the off-line analysis. The purpose of the database is to provide a standard and unified interface where all the informations are stored homogeneously and can be easily correlated to each other.

In the following a description of the processes composing the **Apollo** system will be given. A sketch of its main components is shown in fig. 6.7.

### **DataReader**

this is the basic process in the data acquisition chain. It continuously reads data from the DAQ boards and writes it into shared memories. As shown in fig. 6.8, shared memories can be accessed by other components of the **Apollo** system for different purposes, such as applying trigger algorithms, dumping the continuous data stream into files or looking at the data with a software oscilloscope. One **DataReader** process, running on a separate computer, exists for each data acquisition chassis. The **DataReader** is also responsible for applying triggering and digital filtering. Since it is in charge of acquiring only a subset of the channels in the whole apparatus, it cannot have an overall knowledge of the status of the system. As a consequence, at this level the trigger algorithms only set a flag into the data stream, and the event building is demanded to a separate process, able to handle all the acquired channels in parallel. The **DataReader** also allows to save on file the continuous data streams from each acquired channel. Given the rather low sampling frequency necessary to record the signals from bolometric detectors, the additional required storage space can be easily afforded. This

---

<sup>2</sup>ROOT is a physics data analysis framework developed at CERN: <http://root.cern.ch/>

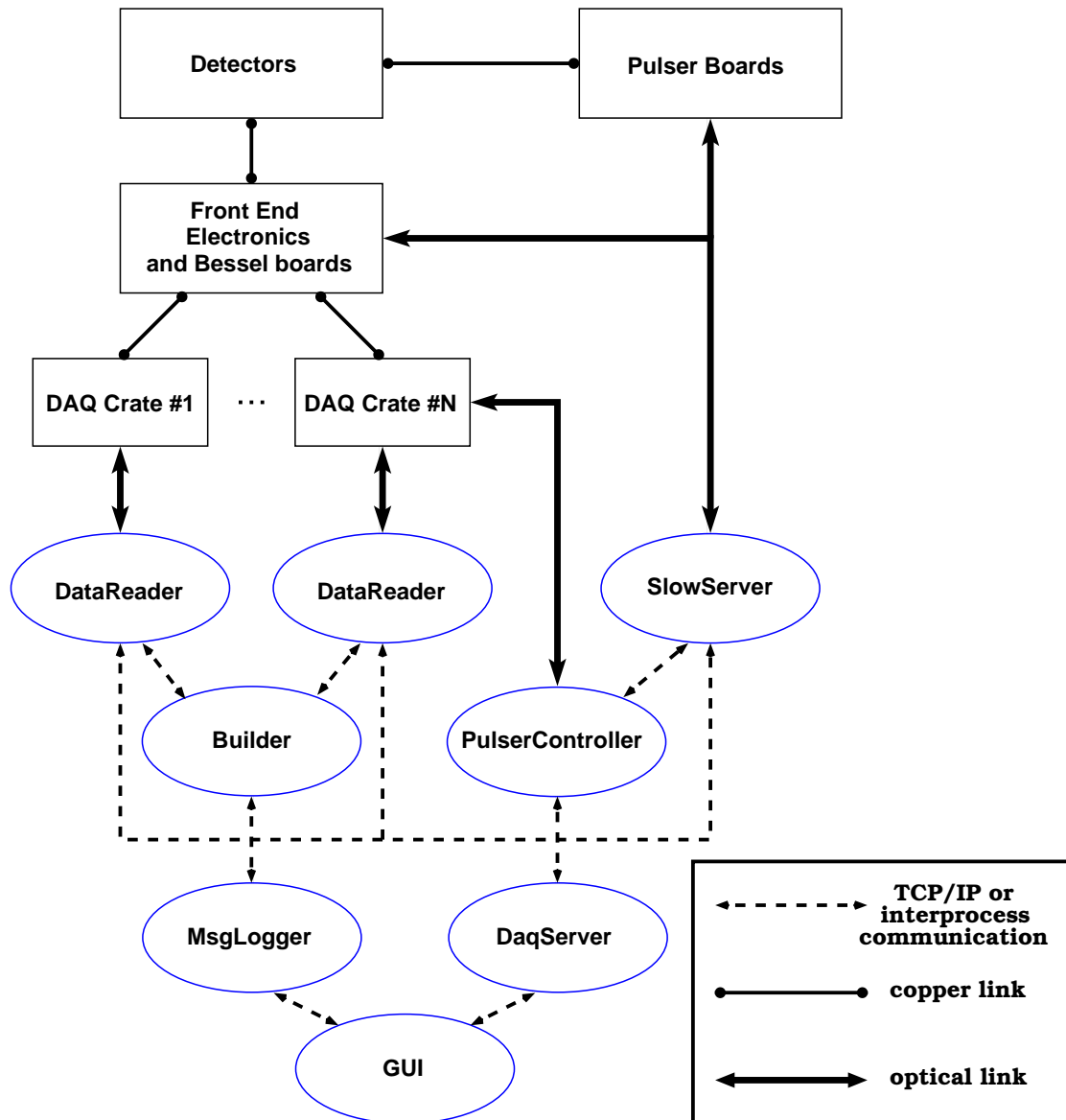


**Figure 6.7:** Schematic representation of the data acquisition system architecture. The fundamental hardware components are depicted as rectangular boxes, while the main software components are represented as blue ellipses.

feature can be used to reprocess the data offline for any kind of purpose, such as investigating possible problems in the detector operation or searching for low energy events with an arbitrarily sophisticated trigger algorithm.

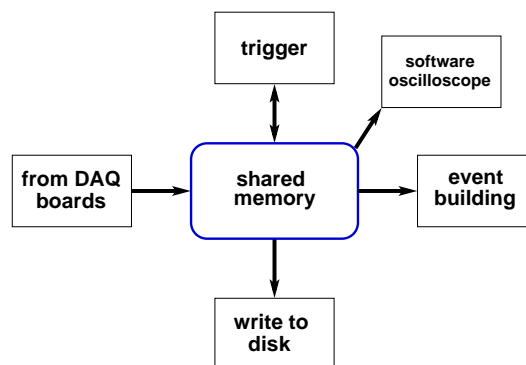


**Figure 6.8:** Sketch of the components accessing the shared memory containing the acquired data. One of such shared memories exists for each acquired channel. In case one of the components resides on a different computer the shared memory is mirrored over the network by mean of a couple of DataSender/DataReceiver processes.

### EventBuilder

this process reads the continuous data written in the shared memories by the DataReader and searches for trigger flags. At this level cross channels informations are available, as signals from all channels are processed in parallel. By accessing the database, the EventBuilder can identify group of channels based on the spatial distance of the crystals they come from, on the particular front-end board they belong to, or any other meaningful criterion. Using these informations, events are built as synchronous groups of waveforms coming from several different detectors. The events are then stored on disk for offline processing using a customized ROOT file format. The EventBuilder process is actually an instance of Diana, the CUORE offline analysis software, running with a particular configuration. Diana has an highly modular structure that allows to plug-in specific analysis packages and event-based filters using a simple configuration file. Therefore, besides the basic event building and data storage operations, the EventBuilder has the possibility to perform a first level online analysis of the acquired data, which allows a prompt monitoring of the detector conditions.

### PulserController

this process is dedicated to the management of the pulser control system. As discussed in chapter 3, the purpose of this subsystem is to send fixed energy calibration pulses on the detectors to monitor their response on short time scales. The PulserController periodically fires heater pulses on the bolometers and also sends a synchronous signal to the DAQ boards that is used for flagging purposes

in the event building phase. The pulser control subsystem will be discussed in sec. 6.6.1.

### **DataSender and DataReceiver**

these two optional processes are present in case the Builder and the DataReader do not reside in the same host. This will happen as soon as more than one DAQ chassis is present in the system. These processes are responsible to perform the mirroring of the shared memories containing the acquired data over the network. Despite their main purpose is to export the shared memories on the host where the EventBuilder resides, they can be used for any other purpose, for example for exporting the data on a remote machine where the detector timelines can be watched almost in real time with a software oscilloscope.

### **MsgLogger**

this process accepts messages from all the components of the **Apollo** system, and writes them to log files. It also handles informations about the status of running processes. A process can inform the message logger about its status or ask for the status of any other running program.

### **DaqServer**

this process has the control over the whole system. It performs all the operations that are needed to start or stop a measurement, and monitors the overall system status during data acquisition.

### **ApolloGUI**

this is the **Apollo** graphical user interface. It communicates with the DaqServer via network to perform standard operations such as starting or stopping a measurement. It includes some basic monitoring tools, such as a software oscilloscope to look at continuous signals on the bolometers, and a display window containing several plots summarizing the status of the measurement.

### **SlowServer**

this process is responsible for hiding the implementation details of the protocols used to communicate with various hardware components of the system, such as the front-end electronics, Bessel filters, power supplies and pulser control boards. It provides a simple network interface that can be used by any other **Apollo** process to query or modify the status of the electronics system. During standard measurements the interaction with this process is limited to the pulser boards, while it is massively involved in the measurements dedicated to the characterization of the detectors (see sec. 6.7).

### 6.4.1 The trigger

Given the low event rate and the slow sampling frequency of bolometric detectors, it was decided to implement a software trigger, which reduces the costs of the system and allows more customizable configurations. Because of the wide spread in the noise and pulse shape of different detectors, an optimal threshold can be achieved at low energy only if the trigger is tuned on the specific features of the signal of each bolometer.

The object-oriented architecture of the Apollo software allowed to build the trigger engine in a modular structure that is transparent to the particular algorithm that is implemented. This permits to easily plug-in different algorithms on different channels. Four independent triggers can search for events at the same time on each channel. They can be based on different algorithms, or even on the same algorithm run with different parameters. This feature could be used for several purposes: for example one trigger could be tuned for high energy  $0\nu\beta\beta$  events, while another one could be optimized for the search of low energy events.

At present two distinct algorithms have been implemented that are usually run in parallel on each channel. The first one is a simple random trigger, which has the purpose of acquiring the baseline samples that are used to produce the noise power spectra required by the optimum filter technique, used for signal amplitude evaluation (see sec. 3.7). The other algorithm has the purpose of triggering physical pulses. It is based on the simple concept sketched in the left plot of fig. 6.9: the difference in the signal amplitude of two samples at a fixed time distance (average) is compared with a reference value (threshold); if this quantity is bigger than the threshold for at least a given number of consecutive samplings, a trigger flag is set in the data stream on the first sample that exceeded the threshold.

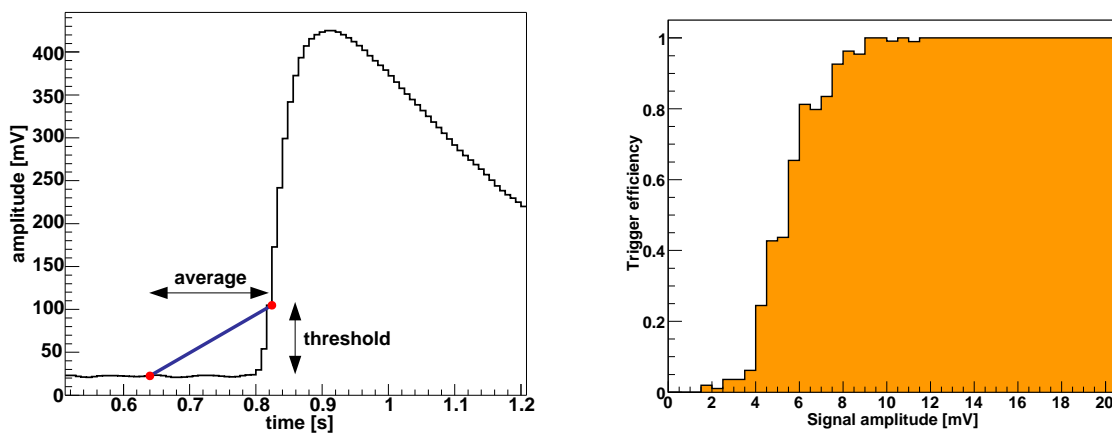


**Figure 6.9:** Simple trigger algorithm implemented in Apollo. The left plot sketches the basic concept of the trigger implementation: the difference in the amplitude of two samples at a fixed distance must be bigger than a certain reference threshold for the trigger to fire. The right plot shows an example of the achieved trigger threshold on a CUORICINO-like pulse obtained from a Monte Carlo simulation.

A Monte Carlo simulation specifically developed by the CUORE collaboration to reproduce the thermal pulses was used to check the performance of the trigger. As shown in the right plot of fig. 6.9, a threshold as low as few mV (corresponding to less than 50 keV) can be achieved with this simple algorithm.

Given the very naive approach of the trigger algorithm implemented so far, it is likely that a more sophisticated one will be developed for CUORE. In fact the main aim of this algorithm was to have the possibility to reproduce the whole data acquisition chain in the validation measurements performed on real detectors that will be discussed in the following sections. As will be shown, the implemented trigger revealed to be fairly adequate for this purpose.

## 6.5 Upgrade of the DAQ system for the Hall C R&D apparatus

A prototype of the Apollo system was installed in 2006 in the CUORE R&D apparatus in the Hall C of LNGS. The installation had the double purpose to test the new data acquisition system on real detectors, and to upgrade the old DAQ system after proper validation of the new one.

The upgrade was motivated by the fact that the old setup, a system based on the VXI standard formerly used for the acquisition of the MiDBD experiment, was provided with insufficient computing resources, which caused frequent crashes when the number of acquired channel or even the event rate were too high. Being an embedded system, it was not possible to simply replace the computer used for the control of the acquisition.

The Apollo prototype installed in Hall C consisted in a single DAQ chassis hosting three NI PXI-6284 boards, for a total amount of 48 channels. As a first step a single computer with the core data acquisition components was installed, missing the control over the heater pulses system and the front-end electronics. The old and new DAQ systems were run in parallel to perform proper cross checks of the overall performance of the new system. This was made possible thanks to the presence of a custom interface (the *patch panel*) used to split the signals from the detectors and send them to the two systems. It was positioned in the last step of the detectors readout chain, between the Bessel filters and the two DAQ systems (see fig. 6.10). The patch panel also included an interface to convert the differential signals from the detectors into unipolar ones. The unipolar signals, exported to standard BNC connectors, could be used to look at the analog signals using a standard oscilloscope.

The first test on real detectors was performed during the RAD5 measurement (see sec. 5.5). It only lasted few days, but allowed to validate the basic functionalities of the system and to identify several hardware configuration problems. These were related mainly to the presence of electro-magnetic interference, and to the contemporary operation of the two DAQ systems. The first problem was easily solved by proper shielding along all the path followed by the signals. The second problem, producing

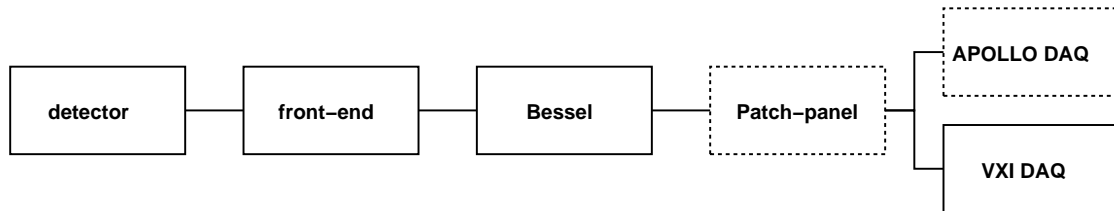


**Figure 6.10:** Schematic representation of the hardware upgrade of the DAQ system in Hall C. The dashed boxes represent the new components introduced in the upgrade.

on the Apollo data the frequent and fast spikes visible in fig. 6.11, was due to the concurrent operation of the two DAQ systems, as demonstrated by the fact that the spikes disappeared when the old system was temporarily switched off. Despite the presence of the spikes could not be completely avoided, it should be stressed that they did not represent a real problem. First, since the high frequency components of the signals have almost no weight when applying the Optimum Filter technique, the spikes would have a negligible impact on the overall quality of the acquired data. Moreover, the contemporary operation of two DAQ systems is only necessary for testing purposes and will be abandoned after a complete validation of Apollo. Finally, it turned out that such spikes could be avoided by decreasing the sampling frequency of the Apollo DAQ boards: in order to check the system under stress conditions, the first measurements were performed with a sampling frequency of 2 kHz. When the detectors were acquired with a sampling frequency of 125 Hz, which is the usual value adopted in the standard measurements, there was no presence of the fast spikes in the data.

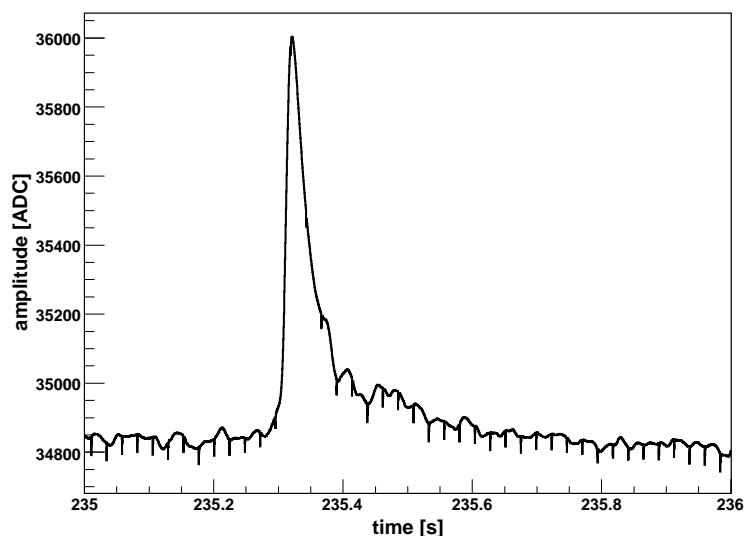


**Figure 6.11:** Example of waveform containing the high frequency spikes produced by the sudden change of impedance of the hardware trigger input stage of the old DAQ system.

Several other tests of increasing duration were performed on the Hall C apparatus, in which *Apollo* proved to be reliable even in conditions of high event rates, when the old DAQ system suffered of crashes due to excessive load. An example of the results obtained from the Hall C tests is shown in fig. 6.12, where the amplitude spectrum measured by *Apollo* and by the old DAQ system are compared for one of the acquired channels. At present the two DAQ systems are regularly run in parallel for standard radioactivity R&D measurements. Two independent analyses are usually performed on the data acquired by *Apollo* and by the old DAQ system, to check for the presence of possible anomalies.

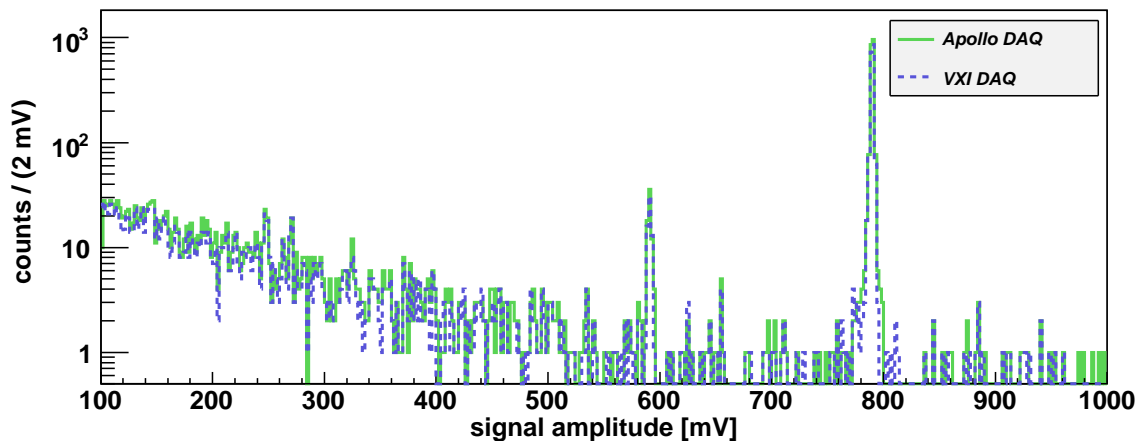


**Figure 6.12:** Comparison of the amplitude spectra between the old (dashed line) and new (continuous line) DAQ system in Hall C. The signal amplitudes shown in this spectrum were evaluated with a simple max-min algorithm.

## 6.6 Upgrade of the CUORICINO DAQ system

After the successful outcome of the Hall C tests, the CUORE collaboration decided to upgrade the DAQ system of CUORICINO. The upgrade took place in the early 2008, during the last few months of data taking of the experiment. It was performed contemporary to a test in which several plastic scintillators were positioned on top of the cryogenic apparatus to study the possible influence of muon-induced events in the background of CUORICINO.

The new system was very similar to the one installed in Hall C. Five NI PXI-6284 data acquisition boards were hosted on a single chassis, for a total amount of 80 channels. Due to the limited experimental space, usually a small number of detectors is operated in the Hall C apparatus. Therefore, even if the new system provided the possibility to acquire up to 48 channels, in all the tests performed in Hall C no more than 16 channels were acquired at the same time. In contrast, in the case of the

CUORICINO upgrade, most of the available channels were exploited, as 62 bolometers were acquired together with two thermometers attached to the mechanical structure of the tower. In order to operate the old and new data acquisition systems in parallel, an interface for signal splitting, identical to the one deployed in the Hall C upgrade was introduced (see fig. 6.10).

The new data acquisition system proved to be stable over the three months of continuous measurements. As in the case of Hall C, the amplitude spectrum measured by **Apollo** was compared to the one obtained by the old system. The results, reported in fig. 6.13, showed a good accordance between the two systems. The only significant differences, visible in the bottom left plot in fig. 6.13, were due to the different performance at low energy of the trigger algorithms implemented by the two systems.

A further confirmation of the good performance of the **Apollo** system was obtained from the study of the noise power spectra (NPS) of several detectors. The spectra shown in fig. 6.14 were obtained for each channel by averaging about 100 NPS obtained from the baseline samplings acquired randomly during the measurements. The top plots show, for two channels, the comparison of the NPS evaluated from the data acquired by **Apollo** and the old system during the same time interval (about one day). The various peaks, with different position and amplitude in the two displayed channels, are produced by microphonic noise in the wires connecting the detectors to the preamplifier stage of the readout chain. Since the wiring of each detector follows an independent path, different features are expected on each channel. The sudden drop in the spectrum at about 12 Hz, common to all channels, is due to the Bessel filters that precede the two data acquisition systems in the readout chain. At high frequency, above 20 Hz, the **Apollo** noise is much lower compared to the one of the old system. This is due to the different resolution of the two digitizers: **Apollo** uses a 18 bit ADC, while a 16 bit ADC is used by the old system. At lower frequency there is a good accordance between the **Apollo** and **VXI** spectra. The small differences can be ascribed to the fact that the detector baselines used for the evaluation of the average NPS were not acquired exactly at the same time by the two systems. This is confirmed by the two bottom plots in fig. 6.14, which show the noise power spectra evaluated from the old DAQ system in different time periods. The discrepancies, even more evident than the ones obtained by the comparison with **Apollo**, prove that the time dependence of the detector noise is the main responsible for the differences at low frequency. In addition, the fact that the two power spectra for the measurements 1051 and 1151 correspond to data acquired before the upgrade of the CUORICINO DAQ system, demonstrates that the modifications in the hardware set-up did not introduce significant noise in the apparatus.

### 6.6.1 The pulser control subsystem

Besides representing the first measurement with a big number of channels, the upgrade of the CUORICINO DAQ also included the integration in **Apollo** of the pulser control

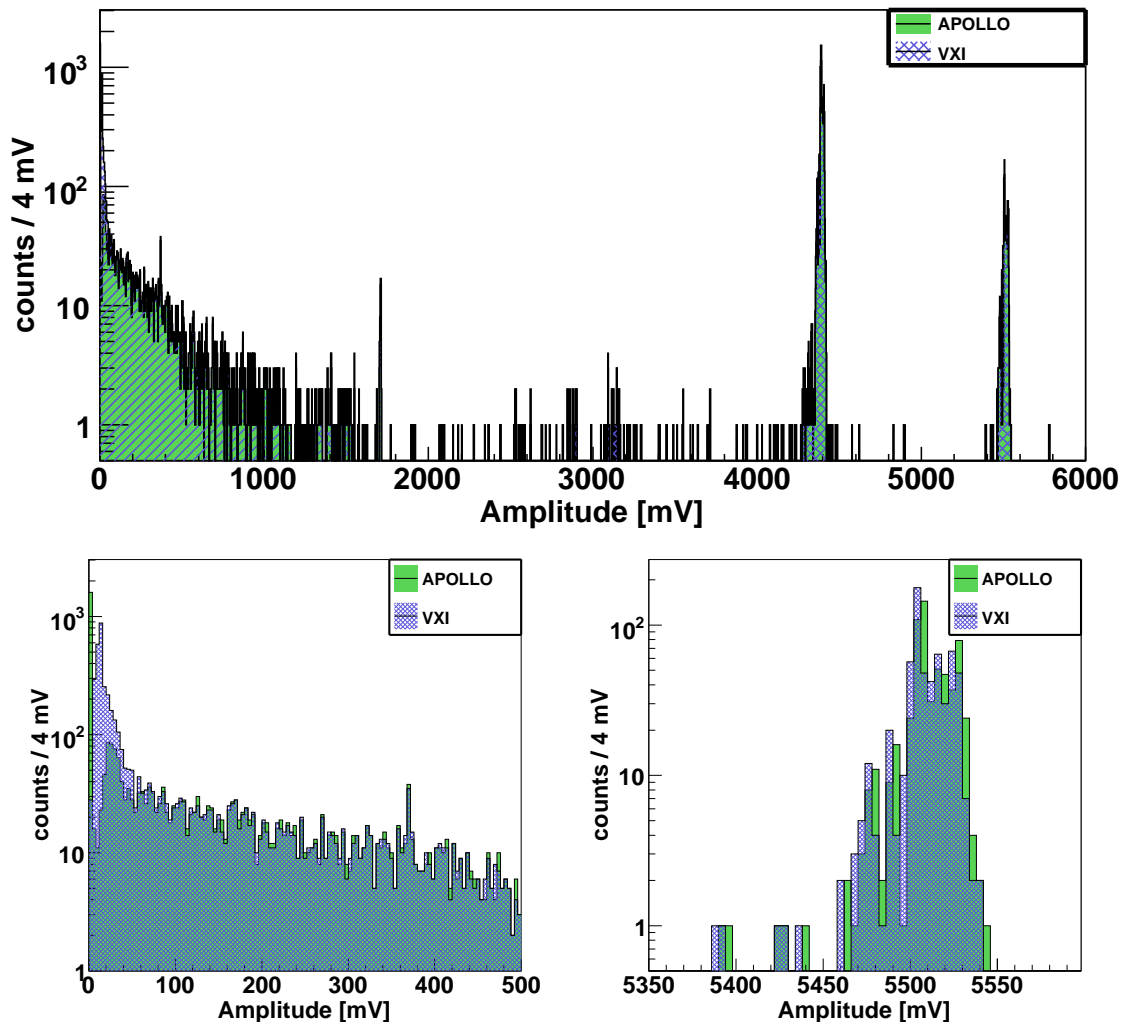


**Figure 6.13:** Comparison of the amplitude spectra between the old and new DAQ system in the Hall A muon run. The top plot shows the whole amplitude spectrum acquired by a detector during about one month of data taking. The bottom plots show an enlarged view of the low (left) and high (right) amplitude range.

system. As widely discussed, the purpose of the pulser is to have a fixed energy reference signal that can be used offline to correct the gain instabilities of the detectors [64]. Such signals are obtained by sending on the Si resistors attached to each bolometer a rectangular shaped pulse whose amplitude and duration can be configured remotely by mean of several registers. Since the duration of the electric signal is short compared to the typical time response of the bolometers, the resulting thermal pulse is almost indistinguishable from the ones produced by particle interactions. The pulser hardware can operate in two modes: either it can fire immediately once the parameters are set into the registers for a given channel (software trigger mode), or it can wait for a trigger

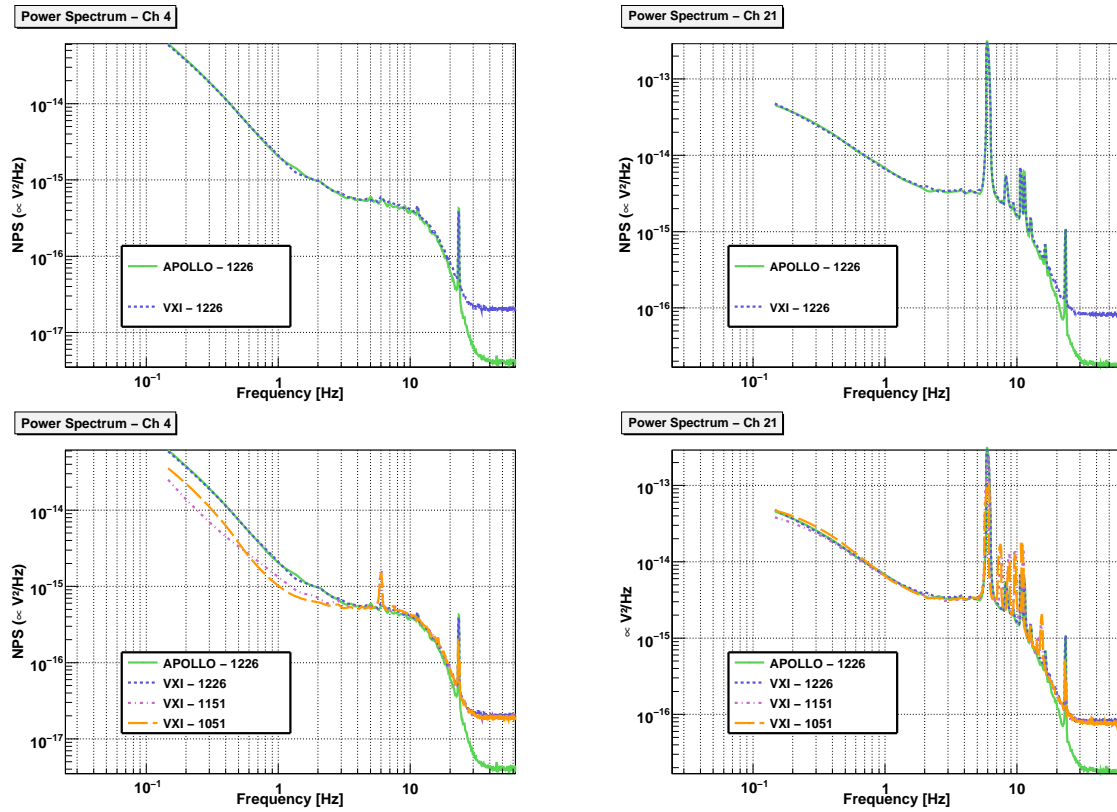


**Figure 6.14:** Noise power spectra for signals acquired with the old and new DAQ systems. The top plots show the noise power spectra comparison between the old DAQ system (VXI) and the new one (Apollo) for two channels. The bottom plots show for the same channels the noise power spectra from other measurements with the old DAQ system. They demonstrate that, at least at low frequency, the differences between the power spectra are produced by varying conditions of the apparatus at different times.

signal to generate the pulse (hardware trigger mode). The preferred behavior can be easily chosen by mean of a switch on the pulser boards.

The software trigger mode, used by the old data acquisition system, had several drawbacks. Given the lack of real time synchronization between the DAQ and the pulser hardware, the adopted approach consisted in flagging as heater pulses all the triggered events that were detected within one second from when the settings were applied to the pulser registers.

Given the low event rate of bolometric detectors, the large time window used to flag heater events was not a major problem by itself: it is unlikely for a particle pulse to occur within such time window, and in any case events containing more than one pulse could be easily identified and discarded offline. However the heater pulses were saved and flagged only in the case in which they were detected by the trigger algorithm. The trigger efficiency is almost 100% for high energy pulses, but it tends to decrease when approaching low energies. As a consequence it was not possible to use the flagging

mechanism to study the performance of the detectors in the energy region close to the trigger threshold.

Finally, a further problem was introduced by the concurrent operation of the two DAQ systems: the software trigger mode did not allow to share the flagging mechanism between **Apollo** and the old system.

Given the previous considerations it was decided to upgrade the pulser control system adopting the hardware trigger operation mode. It allows to export the trigger signal to an arbitrary number of systems and provides a better precision in the arrival time of heater pulses, given by the sampling period of the data acquisition boards. In addition it allows to record the detector waveforms without relying on the efficiency of the trigger algorithm, thus opening the possibility to perform reliable studies of the detector performances at low energy.

The architecture of the **Apollo** pulser control system is sketched in fig. 6.15. Each heater pulse is generated by two consecutive steps:

- 1) the pulse parameters are written in the configuration registers; no pulse is generated in this step, since the boards are still waiting for the hardware trigger signal;
- 2) a synchronous signal is sent in parallel to the pulser boards and the two data acquisition systems; it causes the boards to fire and is used by the two DAQ system to flag the corresponding events.

A dedicated process, the `PulserController` (see sec. 6.4), is responsible for this task. It applies the configuration parameters (step 1) using the slow control interface, while the trigger signal (step 2) is generated by a dedicated 24-bit digital I/O board. One of the bits is used as trigger for the pulser boards, while the remaining ones, sent to the two DAQ systems, are used to code the informations about the parameters of the fired pulse.

An arbitrary sequence of pulses of different amplitudes can be fired independently on each channel. When the `PulserController` is started, the sequences are read from the database, and heater pulses with the corresponding configurations are periodically fired on the detectors.

The **Apollo** pulser control system, introduced for the first time in the **CUORICINO** upgrade, proved to be stable even over long time measurements. An example of its operation is shown in fig. 6.16, where the signal amplitude for particle and heater pulses is plotted versus the arrival time for one of the **CUORICINO** channels. In the measurement shown in the figure heater pulses with three different amplitudes were being fired on the detectors with a time interval of about 300 s. Every eight pulses of standard amplitude (the ones used for offline gain corrections), one high energy pulse and one low energy pulse were generated. A check was performed to ensure that the number of recorded heater pulses corresponded to the expected one, and the result was successful even for the low energy pulses.

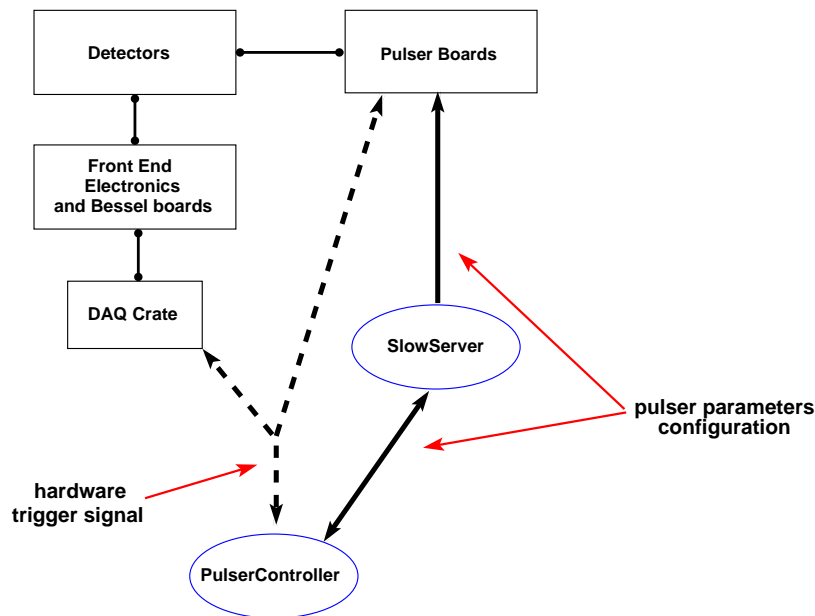


**Figure 6.15:** Sketch of the Apollo pulser control system architecture. Heater pulses are generated in two steps: first the hardware boards are configured with the parameters of the pulse to be fired, and then a synchronous trigger signal is sent in parallel to the pulser boards and to the DAQ system.

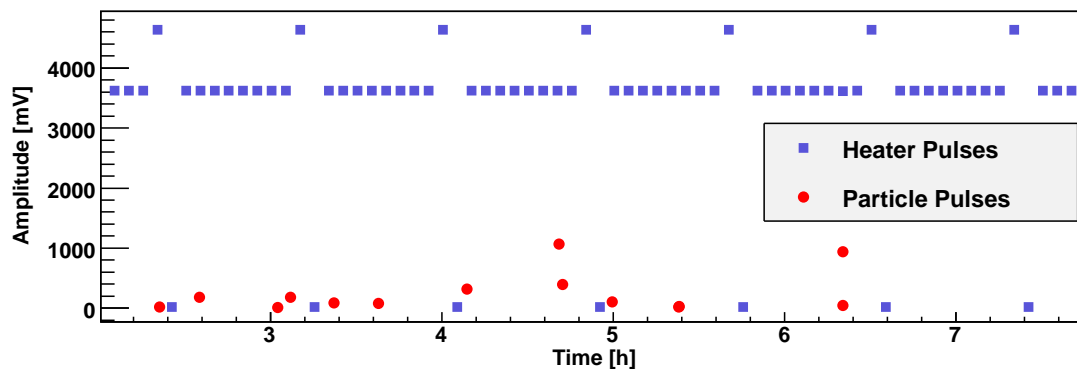


**Figure 6.16:** Demonstration of the heater pulses flagging capability of Apollo. The plot shows the signal amplitude versus time for the pulses acquired on one of the CUORICINO channels. The violet boxes are the events flagged as heater pulses, while the red circular dots are standard particle pulses.

## 6.7 Detector characterization procedure

The upgrade of the Hall C and CUORICINO DAQ systems proved the good performance and stability of the core components of Apollo, and additional improvements were obtained with the introduction of the pulser control system. A further step towards the complete implementation of Apollo was done in the summer of 2008, when the automatic procedure for the characterization of the detectors was tested for the first

time in the Hall C apparatus. Despite the main purpose of the tests was to obtain a proof of concept for the correct functioning of the whole procedure, the characterization of several detectors at two different temperatures could be obtained as well. Moreover in these measurements the SlowServer, the Apollo process used to interface with the electronics components of the apparatus was subject to intensive stress for the first time. In contrast to the past tests, when the use of the slow control software was limited to the interaction with the heater pulse boards, in the detector characterization procedure all the features of this interface were exploited.

### 6.7.1 Overview

The two main goals of the load curves procedure are the measurement of the characteristic I-V curve of the detectors, and the identification along such curves of the working point corresponding the best signal to noise ratio. The I-V curve is obtained by measuring the voltage drop across the bolometer sensors in static conditions (no pulses) for different values of the bias current in the polarization circuit. Similarly, the identification of the optimal working point requires the measurement of the amplitude of fixed energy reference pulses for several values of the bias current.

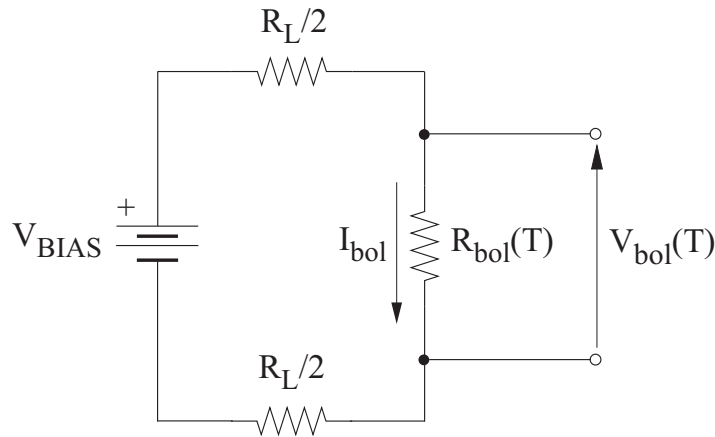


**Figure 6.17:** Sketch of the detector biasing circuit.

The bolometer current can be modified by changing the bias voltage of the polarization circuit shown in fig. 6.17, while the quantity that can be measured to evaluate the bolometer voltage ( $V_{bol}$ ) is the amplitude of the signals at the end of the readout chain ( $V_{OUT}$ ). It is given by

$$V_{OUT} = (V_{OFF} + V_{bol}) \cdot G, \quad (6.1)$$

where  $G$  is the gain introduced in the readout chain and  $V_{OFF}$  is the offset summed to the bolometer voltage before the preamplifier to make the resulting signal fit in the

range of the ADC. Since it can be programmed by mean of dedicated configuration registers, at least in principle its value can be known exactly. There could be however some additional contributions to the offset coming for example from thermocouple effects in the wires connecting the bolometers to the front end electronics [69]. In order to eliminate such unknown contributions, the bolometer voltage is usually evaluated by mean of two measurements performed with opposite values of the bias voltage polarity, so that the offset component can be eliminated (or even estimated):

$$V_{OUT}^{\pm} = (V_{OFF} \pm V_{bol}) \cdot G, \rightarrow V_{bol} = \frac{V_{OUT}^+ - V_{OUT}^-}{2G} \quad (6.2)$$

For a given bias voltage  $V_B$ , the corresponding bolometer current  $I_{bol}$  is given by

$$I_{bol} = \frac{V_B - V_{bol}}{R_L}, \quad (6.3)$$

where  $R_L$  is the load resistance of the circuit shown in fig. 6.17. The whole load curve is therefore drawn by repeating the described measurement procedure for different values of the applied bias voltage, while the fixed energy reference pulses necessary for the identification of the optimal working point can be easily obtained by exploiting the pulser control system described in sec. 6.6.1.

In standard detector operation a static voltage drop of few mV is present across the bolometers, and a much smaller signal variation is produced by particle interactions (typically 100  $\mu$ V per MeV of released energy). During the load curve procedure the bolometer voltage is varied in a much wider range, roughly from zero to few tens of mV. Moreover, in contrast to the case of standard measurements, where the signal is usually maintained in the range between 0 V and 10 V, in the load curves procedure the inversion of the bias voltage polarity makes the signal assume values in a range almost symmetric around zero. For these reasons both the bias voltage and the gain of the readout chain can assume during the detector characterization procedure some values that are unusual in standard measurements.

In the past the load curves procedure was performed by changing manually the parameters of the polarization circuit, and measuring the resulting signals with a standard oscilloscope. This was imposed mainly by the lack of a real integration between the slow control and the data acquisition system, and by the fact that the old DAQ boards could only accept signals in the positive range 0÷10 V. However the manual approach, rather annoying even in the case of the small number of detectors used in the Hall C measurements, cannot be extended to the case of CUORE, when the characterization of about 1000 bolometers will have to be performed. Besides requiring a much smaller effort compared to the manual approach, the presence of an automatic procedure permits to obtain faster and more precise measurements, resulting in a better control over the performance of the detectors.

### 6.7.2 Implementation

It follows from the discussion presented in the previous section that several requirements must be satisfied by the implementation of the automatic load curves procedure:

- possibility to modify the electronics parameters at runtime;
- possibility to identify in the acquired data the time periods corresponding to different configuration of the electronics parameters;
- possibility to perform measurements in parallel on several channels, with the purpose of speeding up the whole procedure;
- possibility to perform an online analysis of the results, in order to optimize the density of points in different zones of the load curve;
- possibility to reprocess all the data offline for cross check and fine optimization.

The front-end electronics of CUORICINO and of the Hall C apparatus was designed keeping in mind the possibility to perform the detector characterization procedure. For this reason almost no change was needed in the hardware configuration of the system. The only exception was the introduction of an external power supply used to apply the bias voltage to the detectors. The internal power supply of the front-end electronics allows to apply 32 different values equally distributed in the range  $0\text{ V} \div 10\text{ V}$ . While this provides good versatility in standard measurements, it is not well suited for the load curves procedure, because both the low granularity and the maximum value of applicable bias voltage could be insufficient to accommodate the response of all the detectors. The communication with the external power supply was completely demanded to the slow control server, therefore its presence was completely transparent to the other components of the system.

From the software point of view, the load curves procedure was implemented using the same components involved in standard data acquisition. The detector baselines samples required the evaluation of the I-V curve were obtained by mean of a random trigger, while the pulses used for the evaluation of the optimal working point were obtained with the pulser system described in sec. 6.6.1. For both the I-V and the pulse amplitude curves, each point was obtained as an average of several measurements. The software tools specifically developed for the load curves procedure were limited to the process responsible for event building. As discussed in sec. 6.4, the EventBuilder is actually a particular instance of Diana, the CUORE offline data analysis software. Since the changes in the electronics configuration can be applied only after that all the necessary measurements for a given point of the load curve have been performed, the process responsible for the overall control on the flow of the procedure must be capable of performing some basic analysis on the acquired data: the EventBuilder was the natural choice for this purpose. Given its plug-in based structure, it was possible

to divide the overall analysis and control procedure in several simple subtasks. The following modules were implemented for this purpose:

- a filter to skip the events acquired in the transients in which modifications were being applied to front end electronics;
- a filter to skip the events in which the detector baseline was not sufficiently stable: this can happen during the recovery after changes in the electronics settings, but also on the tail of particle or heater pulses;
- a filter to skip the events in which one or more physical pulse were present; such events are not interesting during the load curves procedure, since the DC characterization of the detectors requires samples without pulses, while the measurement of the pulse amplitude curve requires pulses of fixed energy that are obtained by the heater pulses system;
- a module that is responsible for load curves analysis: it is a simple handler of load curves objects, one for each channel; every time a valid event is detected, it is stored in the load curve for that particular channel; each load curve object is a collection of measurements containing all the relevant informations for the evaluation of the parameters needed to draw the I-V curve.
- a module responsible for the communication with the slow control server; using a network interface, this module can apply changes to the electronics configuration every time that all the measurements for all the channels are completed for a given configuration.

Instead of performing consecutively the two measurements of opposite polarity in each point of the curve, a different approach was preferred in which the measurements with negative bias polarity for all the points were performed, followed by an equal number of measurements with positive bias polarity. This choice was dictated by the reduced number of interactions with the front-end electronics, which produce non negligible transient noise on the detectors. In contrast, changes in the absolute value of the bias polarity, obtained using the external power supply, do not produce such noise. While in the first approach the bias polarity must be inverted as many times as the number of points in the load curves, in the second one a single polarity inversion is required.

A sketch of the load curves procedure is depicted in fig. 6.18. The left plot shows the continuous timeline of one of the acquired detectors during the characterization procedure for a simple case in which only five points of the load curve were drawn. The steps visible in the plot correspond to the change in the bias voltage of the detector polarization circuit. The first half part of the measurement is performed with a given bias polarity, while the remaining part is performed with the opposite polarity. At the end of the procedure the measurements with opposite polarity and with the same bias

voltage are correlated and the corresponding values for the I-V curve are evaluated using eq. (6.2) and eq. (6.3), as shown in the left plot of fig. 6.18.

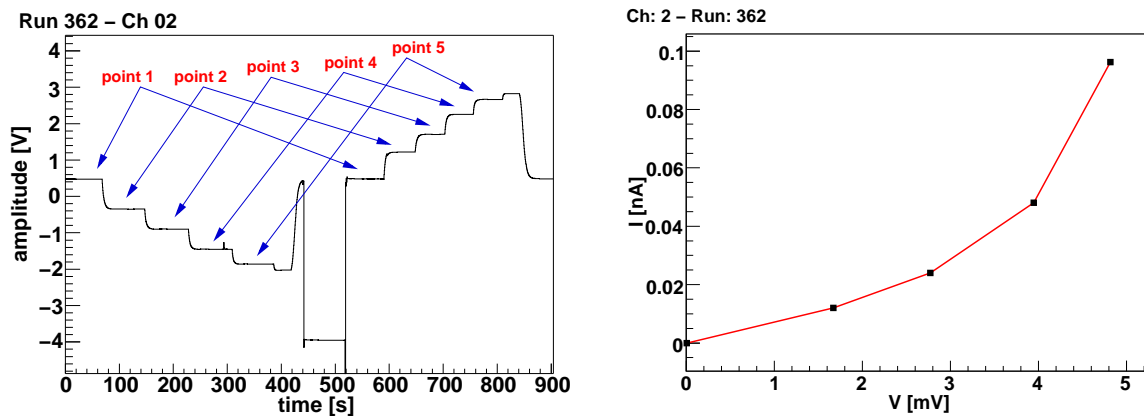


**Figure 6.18:** Example of measurement for the determination of the load curve. The left plot shows the continuous timeline of a detector during the measurement. The changes in the thermistor biasing voltage are clearly visible, as well as the polarity inversion at about 500 s. The I-V curve points depicted in the right plot are evaluated from each couple of measurements with equal bias voltage and opposite polarity.

### 6.7.3 Tests in Hall C

The detector characterization procedure was tested in Hall C in the summer of 2008, at the end of a run dedicated to the study of the flat-pack thermistors (see chapter 5). In this run eight detectors were operated, each of them being provided with a flat-pack thermistor and a standard one. The load curves were measured manually before the beginning of the run, and the measurements were repeated with the automatic procedure at the end of the run. Even if the main purpose of this test was to obtain a proof of concept of the automatic control over the system and the validation of proper synchronization between the different components of the slow control and DAQ system, a satisfactory measurement of the load curves for several channels was obtained at two different temperatures. Figure 6.19 shows for two channels the load curves obtained in two runs performed at different temperature, compared to the manual curve measured (at an even different temperature) at the beginning of the run. The curves are shown either in the I-V plane and in the R-P plane (sensor resistance versus dissipated power).

The curves are in the correct position, as expected from the different temperature in the three measurements. Also the curves from the same detector present a similar shape, and in particular there is a good agreement between the manual curve and the automatic one that was measured at a slightly different temperature. The manual load curves extend up to higher values of the bolometer current, since a wider range was used in that measurement for the bias voltage. However mainly from the R-P plots, where there is a better separation between the curves measured at different temperature, it

can be seen that the automatic measurements were performed with a much higher granularity.

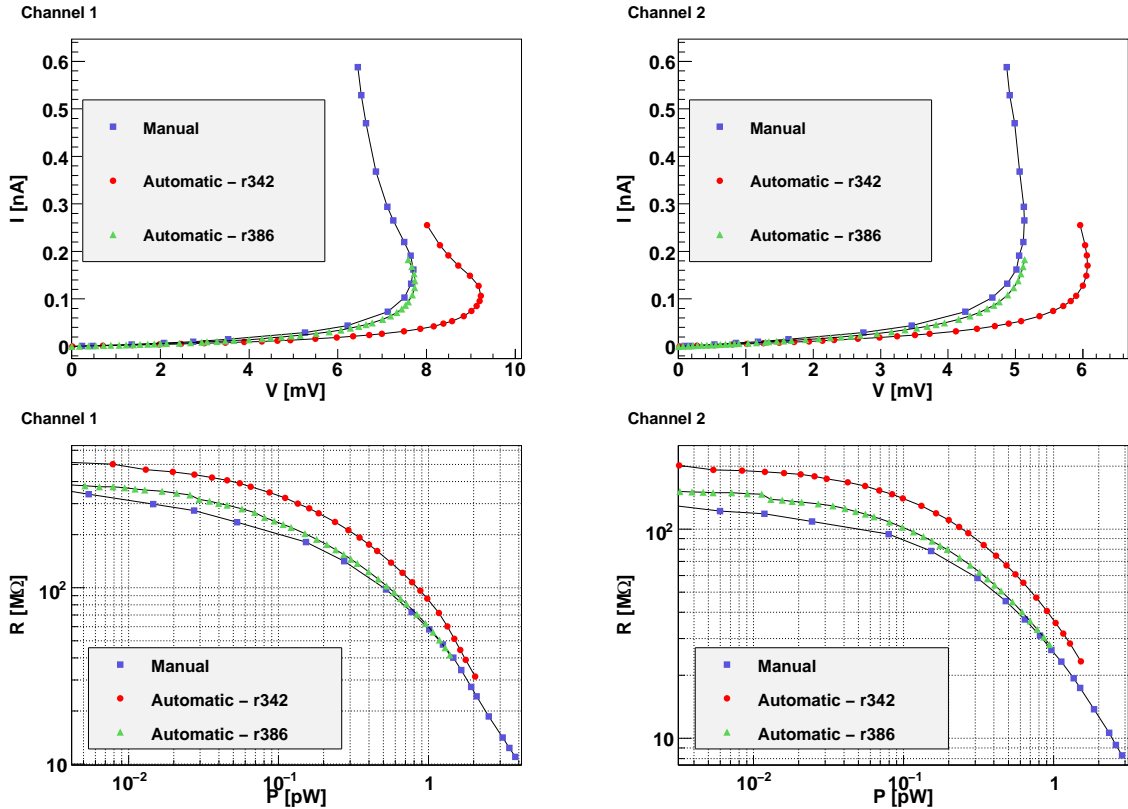


**Figure 6.19:** Comparison of the load curves from two channels measured with the manual (violet squares) and automatic procedure (red circles and green triangles). The curves are drawn in the I-V plane (the two top plots) as well as in the R-P plane (the two bottom plots). The curves correspond to three different values of the detector base temperature.

In one of the runs the heater pulse control system was switched on and the pulse amplitude curve was measured together with the load curve (see fig. 6.20). The curves present the expected shape, apart for the presence of the discontinuity visible on both the detectors slightly below the position of the maximum pulse amplitude. This problem was not realized during the measurements, therefore it was not possible to investigate it in detail. However the most probable reason for such discontinuities was an interference between the detector stabilization circuit and the external power supply used to apply the bias voltage to the detectors. As discussed in chapter 3 a feedback circuit, controlled by a thermometer attached on the mechanical structure of the tower, is used to maintain the detectors at a constant temperature. If some unknown offset is added to the stabilization signal, a variation in the temperature of the apparatus is produced, leading to inconsistent results in the detector characterization measurements. The signal from the stabilization circuit, as well as the bias voltage produced by

the power supply were continuously monitored during the measurements, and a strong correlation was found between these two signals (see fig. 6.21).

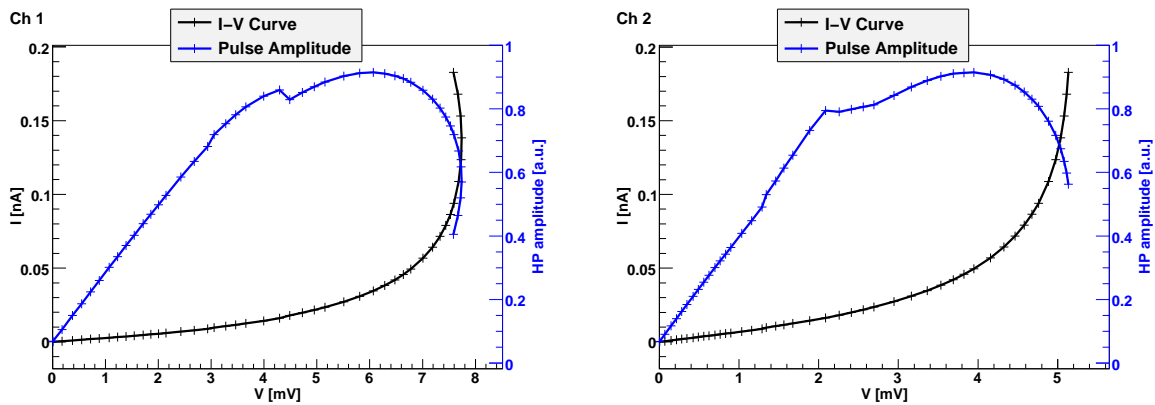


**Figure 6.20:** Pulse amplitude (blue) and load curves (black) measured on two detectors. The pulse amplitude was evaluated with a simple max-min algorithm, it does not represent the signal to noise ratio.

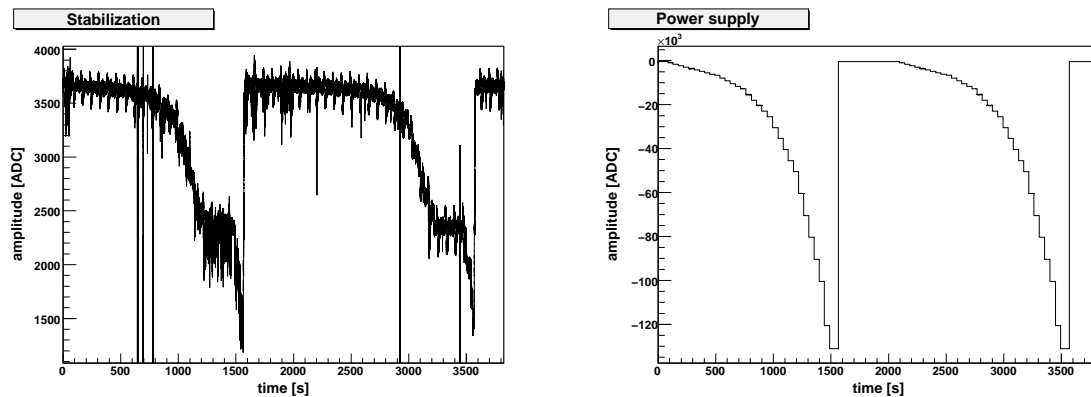


**Figure 6.21:** Explanation of the discontinuities observed in the heater pulse curves. For some reason which was not clearly understood the signal from the temperature stabilization feedback circuit (left) suffered from a strong correlation with the amplitude of the bias voltage produced by the power supply (right). The rectangular steps visible in the monitor signal from the power supply are the changes in the bias voltage corresponding to different points in the load curve.

Apart for the problem with the stabilization circuit, which was probably due to wrong shieldings or cable connections, the first tests of the automatic detector characterization procedure can be considered rather successful. The I-V curves, as well as the pulse amplitude curves, were measured for several detectors, presenting the expected behavior even at different temperatures. Also the duration of the characterization procedure was quite reasonable: in the measurements performed without heater pulses about 32 points were acquired in parallel on eight channels in about one hour. Even if several optimizations can be introduced to speed-up the procedure and to improve the

quality of the measurements, the basic functionalities of the automatic characterization system obtained a substantial validation in the Hall C test.



# Conclusion

The two central topics of this PhD thesis were the development and validation of the data acquisition system for the CUORE experiment, and an analysis of double beta decay to excited states carried out on the data acquired by CUORICINO.

A completely new data acquisition and slow control system is foreseen for the CUORE experiment. Besides providing the core functionalities required to acquire the signals from about 1000 bolometers, the new system will guarantee a strong integration with all the components of the experimental apparatus. Apart for possible minor modifications, the hardware configuration is now defined, and most of the software has been written. Two prototypes were installed in CUORICINO and in the Hall C R&D apparatus, with the double purpose of testing the new system and upgrading the pre-existing ones. Apart for the reduced number of channels, these two systems are very similar to the final one that will be used in CUORE. After the successful overcome of numerous tests, performed both in the Hall C apparatus and in CUORICINO, the CUORE collaboration decided to regularly use the new data acquisition systems for standard physics measurements.

The other argument of this PhD thesis was an analysis of the CUORICINO data focused on the search of two neutrino double beta decay of  $^{130}\text{Te}$  to the excited state  $0^+$  of the daughter nucleus  $^{130}\text{Xe}$ . This decay mode is accompanied by the emission of two photons from the deexcitation of  $^{130}\text{Xe}$ . This clear signature allows to search for events in which two detectors are hit at the same time, thus producing a strong reduction of the background. The basic approach adopted in the analysis was to search in the double hit energy spectrum for the photoelectric peak produced by one of the two deexcitation photons. Several event selection criteria were considered, leading to different values for the detection efficiency and the background level in the region of the peak. No presence of such peak was found in the data and the most conservative limit obtained for the half life of the searched process is  $T_{1/2} > 1.4 \times 10^{22}$  y (90% C.L.).



# List of Figures

1.1	Solar neutrino flux measured by the SNO experiment . . . . .	8
1.2	KamLAND $\bar{\nu}_e$ survival probability as a function of $L_0/E$ . . . . .	8
1.3	The three possible neutrino mass hierarchy schemes. . . . .	14
1.4	Effective Majorana mass as a function of the mass of the lightest neutrino. . . . .	16
1.5	Atomic mass as a function of the atomic number $Z$ . . . . .	17
1.6	Double beta decay diagrams. . . . .	17
1.7	Majorana propagator resulting from $0\nu\beta\beta$ . . . . .	18
1.8	Nuclear matrix elements for several $0\nu\beta\beta$ isotopes. . . . .	20
2.1	Double beta decay energy spectrum . . . . .	23
2.2	Energy spectrum measured by the Heidelberg-Moscow experiment . . . . .	26
2.3	Two neutrino double beta decay energy spectra measured by NEMO 3. . . . .	27
2.4	Basic representation of a bolometric detector. . . . .	30
2.5	Phonon thermalization process in the energy absorber. . . . .	33
2.6	Representation of the hopping conduction mechanism . . . . .	34
2.7	Polarization circuit and R-P curve for a semiconductor thermistor. . . . .	36
2.8	Load Curves for semiconductor thermistors . . . . .	36
2.9	Bolometric pulse shape. . . . .	37
3.1	CUORICINO tower. . . . .	40
3.2	CUORICINO calibration spectra. . . . .	41
3.3	CUORICINO cryostat and shieldings. . . . .	42
3.4	Q-values and natural abundances for several $0\nu\beta\beta$ candidates . . . . .	43
3.5	Detail of the CUORICINO single module. . . . .	45
3.6	Schematic of the thermistor biasing system. . . . .	47
3.7	Heater pulse amplitude as a function of the detector baseline. . . . .	49
3.8	Energy spectra before and after gain instability corrections. . . . .	50
3.9	Background spectrum measured by CUORICINO. . . . .	52
3.10	CUORICINO background in the $0\nu\beta\beta$ region. . . . .	53
3.11	CUORICINO background in the $\alpha$ region. . . . .	54
3.12	Alpha contaminations in CUORICINO. . . . .	55
3.13	Single hit background spectrum in the $0\nu\beta\beta$ region. . . . .	56
3.14	CUORICINO half life limit compared with the claim of observation in $^{76}\text{Ge}$ . . . . .	59

4.1	Nuclear levels of the $^{130}\text{Te}$ triplet. . . . .	64
4.2	Monte Carlo simulation of the $2\nu\beta\beta$ decay to the excited state $0_1^+$ . . . .	66
4.3	Evaluation of the optimal coincidence time window. . . . .	68
4.4	Evaluation of the detection inefficiency due to inactive detectors. . . . .	69
4.5	Average event rate. . . . .	69
4.6	Time holes duration for various values of the threshold probability. . . .	70
4.7	Dead time of the CUORICINO detectors. . . . .	70
4.8	Multiplicity distribution for the simulated and real data. . . . .	71
4.9	Distance between the crystals in the multiplicity 2 events. . . . .	73
4.10	Example of fitting procedure used to evaluate the detection efficiency. . .	74
4.11	Example of the effect of the cuts on simulated data. . . . .	75
4.12	Single and double hit energy spectra measured by CUORICINO. . . . .	76
4.13	Energy spectrum after the application of several selection cuts. . . . .	76
4.14	Explanation of the excess of events around 1253 keV. . . . .	77
4.15	Enlarged view of the double hit spectrum around 1257 keV. . . . .	79
4.16	Fit on the two $^{60}\text{Co}$ peaks to evaluate the energy resolution. . . . .	79
4.17	Example of fit for the case of flat background model. . . . .	80
4.18	Example of fit including the 1253 keV peak. . . . .	81
5.1	CUORE detector array. . . . .	86
5.2	Map of the Laboratori Nazionali del Gran Sasso. . . . .	87
5.3	CUORE cryostat and internal shieldings. . . . .	89
5.4	Sensor gluing on $\text{TeO}_2$ crystals. . . . .	91
5.5	Comparison of CUORICINO-like and flat-pack NTD thermistors. . . . .	91
5.6	Mechanical structure of the CUORE tower. . . . .	92
5.7	The RAD detector. . . . .	93
5.8	Background spectrum in the RAD1 Hall C test. . . . .	94
5.9	Background spectrum in the RAD3+RAD4 Hall C tests. . . . .	96
5.10	Comparison between the standard and the Teflon-free RAD detector. . .	96
5.11	Principles of operation of surface sensitive bolometers (SSB). . . . .	97
5.12	Scatter plots displaying the performance of surface sensitive bolometers	98
6.1	Example of bolometric pulse at the input of the digitization stage. . . .	100
6.2	Analog circuitry at the input of M-series DAQ boards. . . . .	101
6.3	Check of ADC resolution using a 1.5 V battery. . . . .	102
6.4	Effect of the low-pass filter on the crosstalk of adjacent channels. . . . .	103
6.5	Illustration of the round robin sampling mode. . . . .	104
6.6	Relative cross talk versus sampling frequency. . . . .	104
6.7	Schematic representation of the DAQ system architecture. . . . .	106
6.8	Sketch of the components accessing the shared memory containing data.	107
6.9	Simple trigger algorithm implemented in Apollo . . . . .	109
6.10	Sketch of the hardware upgrade of the DAQ system in Hall C. . . . .	111
6.11	Presence of fast spikes in the Hall C signals. . . . .	111

---

6.12	Amplitude spectra of the old and new DAQ systems in Hall C. . . . .	112
6.13	Amplitude spectra of the old and new DAQ systems in Hall A. . . . .	114
6.14	Noise power spectra measured with the old and new DAQ systems. . .	115
6.15	Sketch of the <b>Apollo</b> pulser control system architecture . . . . .	117
6.16	Demonstration of the heater pulses flagging capability of <b>Apollo</b> . . . .	117
6.17	Detector biasing circuit. . . . .	118
6.18	Example of measurement for the determination of the load curve. . . .	122
6.19	Load curves measured with the manual and automatic procedure . . . .	123
6.20	Pulse amplitude curves measured on two detectors . . . . .	124
6.21	Explanation of the discontinuities observed in the heater pulse curves .	124



# References

- [1] L.-L. Chau and W.-Y. Keung, “Comments on the Parametrization of the Kobayashi-Maskawa Matrix,” *Phys. Rev. Lett.*, vol. 53, p. 1802, 1984. [4](#)
- [2] Y. Fukuda *et al.*, “Evidence for oscillation of atmospheric neutrinos,” *Phys. Rev. Lett.*, vol. 81, pp. 1562–1567, 1998, hep-ex/9807003. [6](#)
- [3] D. G. Michael *et al.*, “Observation of muon neutrino disappearance with the MINOS detectors and the NuMI neutrino beam,” *Phys. Rev. Lett.*, vol. 97, p. 191801, 2006, hep-ex/0607088. [6](#)
- [4] M. H. Ahn *et al.*, “Measurement of Neutrino Oscillation by the K2K Experiment,” *Phys. Rev.*, vol. D74, p. 072003, 2006, hep-ex/0606032. [6](#)
- [5] J. Davis, Raymond, D. S. Harmer, and K. C. Hoffman, “Search for neutrinos from the sun,” *Phys. Rev. Lett.*, vol. 20, pp. 1205–1209, 1968. [7](#)
- [6] J. N. Abdurashitov *et al.*, “Measurement of the solar neutrino capture rate with gallium metal,” *Phys. Rev.*, vol. C60, p. 055801, 1999, astro-ph/9907113. [7](#)
- [7] M. Altmann *et al.*, “Complete results for five years of GNO solar neutrino observations,” *Phys. Lett.*, vol. B616, pp. 174–190, 2005, hep-ex/0504037. [7](#)
- [8] S. Fukuda *et al.*, “Solar 8B and hep Neutrino Measurements from 1258 Days of Super-Kamiokande Data,” *Phys. Rev. Lett.*, vol. 86, pp. 5651–5655, 2001, hep-ex/0103032. [7](#)
- [9] J. N. Bahcall, M. H. Pinsonneault, and S. Basu, “Solar models: Current epoch and time dependences, neutrinos, and helioseismological properties,” *Astrophys. J.*, vol. 555, pp. 990–1012, 2001, astro-ph/0010346. [7](#)
- [10] Q. R. Ahmad *et al.*, “Direct evidence for neutrino flavor transformation from neutral-current interactions in the Sudbury Neutrino Observatory,” *Phys. Rev. Lett.*, vol. 89, p. 011301, 2002, nucl-ex/0204008. [7](#)
- [11] B. Aharmim *et al.*, “Measurement of the  $\nu/e$  and total B-8 solar neutrino fluxes with the Sudbury Neutrino Observatory phase I data set,” *Phys. Rev.*, vol. C75, p. 045502, 2007, nucl-ex/0610020. [8](#)

- [12] K. Eguchi *et al.*, “First results from KamLAND: Evidence for reactor anti-neutrino disappearance,” *Phys. Rev. Lett.*, vol. 90, p. 021802, 2003, hep-ex/0212021. [7](#)
- [13] S. Abe *et al.*, “Precision Measurement of Neutrino Oscillation Parameters with KamLAND,” *Phys. Rev. Lett.*, vol. 100, p. 221803, 2008, 0801.4589. [8](#)
- [14] T. Schwetz, M. Tortola, and J. W. F. Valle, “Three-flavour neutrino oscillation update,” 2008, 0808.2016. [9](#)
- [15] C. Kraus *et al.*, “Final Results from phase II of the Mainz Neutrino Mass Search in Tritium  $\beta$  Decay,” *Eur. Phys. J.*, vol. C40, pp. 447–468, 2005, hep-ex/0412056. [14](#)
- [16] V. M. Lobashev *et al.*, “Direct search for neutrino mass and anomaly in the tritium beta-spectrum: Status of ‘Troitsk neutrino mass’ experiment,” *Nucl. Phys. Proc. Suppl.*, vol. 91, pp. 280–286, 2001. [14](#)
- [17] G. Drexlin, “KATRIN: Direct measurement of a sub-eV neutrino mass,” *Nucl. Phys. Proc. Suppl.*, vol. 145, pp. 263–267, 2005. [14](#)
- [18] A. Monfardini *et al.*, “The microcalorimeter arrays for a rhenium experiment (MARE): A next-generation calorimetric neutrino mass experiment,” *Prog. Part. Nucl. Phys.*, vol. 57, pp. 68–70, 2006, hep-ex/0509038. [14](#)
- [19] A. Strumia and F. Vissani, “Neutrino masses and mixings and.,” 2006, hep-ph/0606054. [16](#)
- [20] M. Goeppert-Mayer, “Double beta-disintegration,” *Phys. Rev.*, vol. 48, pp. 512–516, Sep 1935. [16](#)
- [21] B. Povh, K. Rith, C. Scholz, and F. Zetsche, *Particles and Nuclei*. Springer, 6th ed., 2008. [16](#)
- [22] S. R. Elliott, A. A. Hahn, and M. K. Moe, “Direct evidence for two-neutrino double-beta decay in Se- 82,” *Phys. Rev. Lett.*, vol. 59, pp. 2020–2023, 1987. [16](#)
- [23] R. N. Mohapatra and P. B. Pal, *Massive Neutrinos in Physics and Astrophysics*. World Scientific, 3rd ed., 2004. ISBN: 98123807101. [17](#), [24](#)
- [24] J. Schechter and J. W. F. Valle, “Neutrinoless double- $\beta$  decay in  $SU(2)\times U(1)$  theories,” *Phys. Rev. D*, vol. 25, pp. 2951–2954, Jun 1982. [17](#)
- [25] I. Avignone, Frank T., S. R. Elliott, and J. Engel, “Double Beta Decay, Majorana Neutrinos, and Neutrino Mass,” *Rev. Mod. Phys.*, vol. 80, pp. 481–516, 2008, 0708.1033. [17](#), [22](#)

- [26] I. Ogawa *et al.*, “Search for neutrino-less double beta decay of Ca-48 by CaF-2 scintillator,” *Nucl. Phys.*, vol. A730, pp. 215–223, 2004. [18](#)
- [27] H. V. Klapdor-Kleingrothaus *et al.*, “Latest Results from the Heidelberg-Moscow Double Beta Decay Experiment,” *Eur. Phys. J.*, vol. A12, pp. 147–154, 2001, hep-ph/0103062. [18](#), [25](#), [39](#)
- [28] H. V. Klapdor-Kleingrothaus, I. V. Krivosheina, A. Dietz, and O. Chkvorets, “Search for neutrinoless double beta decay with enriched  $^{76}\text{Ge}$  in Gran Sasso 1990-2003,” *Phys. Lett.*, vol. B586, pp. 198–212, 2004, hep-ph/0404088. [18](#), [26](#), [58](#)
- [29] R. Arnold *et al.*, “First results of the search of neutrinoless double beta decay with the NEMO 3 detector,” *Phys. Rev. Lett.*, vol. 95, p. 182302, 2005, hep-ex/0507083. [18](#), [27](#)
- [30] R. Arnold *et al.*, “Double beta decay of Zr-96,” *Nucl. Phys.*, vol. A658, pp. 299–312, 1999. [18](#)
- [31] F. A. Danevich *et al.*, “Search for 2 beta decay of cadmium and tungsten isotopes: Final results of the Solotvina experiment,” *Phys. Rev.*, vol. C68, p. 035501, 2003. [18](#), [63](#)
- [32] C. Arnaboldi *et al.*, “Results from a search for the  $0\nu\beta\beta$ -decay of  $^{130}\text{Te}$ ,” *Phys. Rev.*, vol. C78, p. 035502, 2008, 0802.3439. [18](#), [26](#), [39](#)
- [33] R. Bernabei *et al.*, “Investigation of beta beta decay modes in Xe-134 and Xe-136,” *Phys. Lett.*, vol. B546, pp. 23–28, 2002. [18](#)
- [34] . J. Argyriades, “Measurement of the Double Beta Decay Half-life of  $^{150}\text{Nd}$  and Search for Neutrinoless Decay Modes with the NEMO-3 Detector,” 2008, 0810.0248. [18](#)
- [35] J. Menendez, A. Poves, E. Caurier, and F. Nowacki, “Deformation and the Nuclear Matrix Elements of the Neutrinoless Double Beta Decay,” 2008, 0809.2183. [20](#)
- [36] F. T. Avignone, G. S. King, and Y. G. Zdesenko, “Next generation double-beta decay experiments: Metrics for their evaluation,” *New J. Phys.*, vol. 7, p. 6, 2005. [24](#)
- [37] S. R. Elliott and P. Vogel, “Double beta decay,” *Ann. Rev. Nucl. Part. Sci.*, vol. 52, pp. 115–151, 2002, hep-ph/0202264. [24](#)
- [38] C. E. Aalseth *et al.*, “The Igex  $^{76}\text{Ge}$  Neutrinoless Double-Beta Decay Experiment: Prospects for Next Generation Experiments,” *Phys. Rev.*, vol. D65, p. 092007, 2002, hep-ex/0202026. [25](#), [39](#)

- [39] A. Staudt, K. Muto, and H. V. Klapdor-Kleingrothaus, “Calculation of  $2\nu$  and  $0\nu$  double-beta decay rates,” *Europhys. Lett.*, vol. 13, pp. 31–36, 1990. [25](#), [26](#)
- [40] H. V. Klapdor-Kleingrothaus, A. Dietz, H. L. Harney, and I. V. Krivosheina, “Evidence for Neutrinoless Double Beta Decay,” *Mod. Phys. Lett.*, vol. A16, pp. 2409–2420, 2001, hep-ph/0201231. [26](#), [58](#)
- [41] V. A. Rodin, A. Faessler, F. Simkovic, and P. Vogel, “Assessment of uncertainties in QRPA  $0\nu$  beta beta-decay nuclear matrix elements,” *Nucl. Phys.*, vol. A766, pp. 107–131, 2006, 0706.4304. [26](#), [57](#), [58](#), [59](#)
- [42] R. Arnold *et al.*, “Technical design and performance of the NEMO 3 detector,” *Nucl. Instrum. Meth.*, vol. A536, pp. 79–122, 2005, physics/0402115. [26](#)
- [43] I. Abt *et al.*, “A new Ge-76 double beta decay experiment at LNGS,” 2004, hep-ex/0404039. [27](#)
- [44] V. E. Guiseppe *et al.*, “The Majorana Neutrinoless Double-Beta Decay Experiment,” 2008, 0811.2446. [28](#)
- [45] R. Gaitskell *et al.*, “White paper on the Majorana zero-neutrino double-beta decay experiment,” 2003, nucl-ex/0311013. [28](#)
- [46] C. Arnaboldi *et al.*, “CUORE: A cryogenic underground observatory for rare events,” *Nucl. Instrum. Meth.*, vol. A518, pp. 775–798, 2004, hep-ex/0212053. [29](#), [85](#)
- [47] R. Ardito *et al.*, “CUORE: A cryogenic underground observatory for rare events,” 2005, hep-ex/0501010. [29](#)
- [48] F. Piquemal, “The SuperNEMO project,” *Phys. Atom. Nucl.*, vol. 69, pp. 2096–2100, 2006. [29](#)
- [49] M. Danilov *et al.*, “Detection of very small neutrino masses in double-beta decay using laser tagging,” *Phys. Lett.*, vol. B480, pp. 12–18, 2000, hep-ex/0002003. [29](#)
- [50] M. K. Moe, “New approach to the detection of neutrinoless double-beta decay,” *Phys. Rev.*, vol. C44, pp. 931–934, 1991. [29](#)
- [51] S. Simom, “Application of Low Temperature Calorimetry to Radioactive Measurements,” *Nature*, vol. 135, p. 763, 1935. [30](#)
- [52] E. Fiorini and T. O. Niinikoski, “Low temperature calorimetry for rare decays,” *Nucl. Instr. Meth.*, vol. A224, p. 83, 1984. [30](#), [39](#)
- [53] C. Kittel, *Introduction to Solid State Physics*. John Wiley and Sons, seventh ed., December 1996. [31](#)

- [54] Y. B. Levinson, “Nonequilibrium Phonons in Nonmetallic Crystals,” *Modern Problems in Condensed Matter Sciences*, vol. 16, pp. 91–143, 1986. ISBN: 0-444-86989-1. [32](#)
- [55] N. F. Mott and J. H. Davies, “Metalinsulator transition in doped semiconductors,” *Philosophical Magazine B*, vol. 42, pp. 845–858, 1980. [34](#)
- [56] A. Miller and E. Abrahams, “Impurity conduction at low concentrations,” *Physical Review*, vol. 120, pp. 745–755, 1960. [34](#)
- [57] A. Alessandrello *et al.*, “A New search for neutrinoless beta beta decay with a thermal detector,” *Phys. Lett.*, vol. B335, pp. 519–525, 1994. [39](#)
- [58] C. Arnaboldi *et al.*, “A Calorimetric Search on Double Beta Decay of  $^{130}\text{Te}$ ,” *Phys. Lett.*, vol. B557, pp. 167–175, 2003, hep-ex/0211071. [39](#), [63](#)
- [59] C. Arnaboldi *et al.*, “A New Limit on the Neutrinoless DBD of  $^{130}\text{Te}$ ,” *Phys. Rev. Lett.*, vol. 95, p. 142501, 2005, hep-ex/0501034. [39](#)
- [60] C. Arnaboldi *et al.*, “First results on neutrinoless double beta decay of Te-130 with the calorimetric CUORICINO experiment,” *Phys. Lett.*, vol. B584, pp. 260–268, 2004. [39](#)
- [61] S. P. Ahlen *et al.*, “Study of penetrating cosmic ray muons and search for large scale anisotropies at the Gran Sasso Laboratory,” *Phys. Lett.*, vol. B249, pp. 149–156, 1990. [40](#), [86](#)
- [62] P. Belli *et al.*, “Deep underground neutron flux measurement with large bf-3 counters,” *Nuovo Cim.*, vol. A101, pp. 959–966, 1989. [40](#), [86](#)
- [63] C. Arnaboldi *et al.*, “The temperature stabilization system of CUORICINO: An array of macro bolometers,” *IEEE Trans. Nucl. Sci.*, vol. 52, pp. 1630–1637, 2005. [40](#)
- [64] C. Arnaboldi, G. Pessina, and E. Previtali, “A programmable calibrating pulse generator with multi- outputs and very high stability,” *IEEE Trans. Nucl. Sci.*, vol. 50, pp. 979–986, 2003. [40](#), [114](#)
- [65] A. Alessandrello *et al.*, “Measurements of internal radioactive contamination in samples of Roman lead to be used in experiments on rare events,” *Nucl. Instrum. Meth.*, vol. B142, pp. 163–172, 1998. [41](#)
- [66] K. Zuber, “summary of the workshop on ‘Matrix elements for neutrinoless double beta decay’,” 2005, nucl-ex/0511009. [42](#)

- [67] A. Guiliani *et al.*, “Heat capacity of low temperature ge and si calorimeters and optimization of as implanted silicon thermistors,” *Nucl. Instrum. Meth.*, vol. A263, pp. 233–236, 1988. [44](#)
- [68] M. Pedretti. *et al.*, “Measurement of thermal properties for modeling and optimization of large mass bolometers,” *Physica B*, vol. 329, pp. 1614–1615, 2003. [45](#)
- [69] C. Arnaboldi *et al.*, “The programmable front-end system for CUORICINO, an array of large-mass bolometers,” *IEEE Trans. Nucl. Sci.*, vol. 49, pp. 2440–2447, 2002. [47](#), [119](#)
- [70] E. Gatti and P. F. Manfredi, “Processing the signals from solid state detectors in elementary particle physics,” *Riv. Nuovo Cim.*, vol. 9N1, pp. 1–146, 1986. [48](#)
- [71] S. Baker and R. D. Cousins, “Clarification of the use of chi square and likelihood functions in fits to histograms,” *Nucl. Instrum. Meth.*, vol. 221, pp. 437–442, 1984. [56](#)
- [72] R. M. Barnett *et al.*, “Review of particle physics. Particle Data Group,” *Phys. Rev.*, vol. D54, pp. 1–720, 1996. [56](#)
- [73] E. Caurier, F. Nowacki, and A. Poves, “Nuclear Structure Aspects of the Neutrinoless Double Beta Decay,” *Eur. Phys. J.*, vol. A36, pp. 195–200, 2008, 0709.0277. [57](#), [58](#), [59](#)
- [74] T. Tomoda, “Double beta decay,” *Rept. Prog. Phys.*, vol. 54, pp. 53–126, 1991. [57](#)
- [75] S. Stoica and H. V. Klapdor-Kleingrothaus, “Neutrinoless double- beta -decay matrix elements within the second quasirandom phase approximation method,” *Phys. Rev.*, vol. C63, p. 064304, 2001. [57](#)
- [76] A. Staudt, T. T. S. Kuo, and H. V. Klapdor-Kleingrothaus, “beta beta decay of Te-128, Te-130, and Ge-76 with renormalized effective interactions derived from Paris and Bonn potentials,” *Phys. Rev.*, vol. C46, pp. 871–883, 1992. [57](#)
- [77] C. Barbero, F. Krmpotic, A. Mariano, and D. Tadic, “Nuclear moments for the neutrinoless double beta decay. II,” *Nucl. Phys.*, vol. A650, pp. 485–497, 1999, nucl-th/9902040. [57](#)
- [78] A. Faessler and F. Simkovic, “Double beta decay,” *J. Phys.*, vol. G24, pp. 2139–2178, 1998, hep-ph/9901215. [57](#)
- [79] G. Pantis, F. Simkovic, J. D. Vergados, and A. Faessler, “Neutrinoless Double Beta Decay within QRPA with Proton- Neutron Pairing,” *Phys. Rev.*, vol. C53, pp. 695–707, 1996, nucl-th/9612036. [57](#)

- [80] F. Simkovic, G. Pantis, J. D. Vergados, and A. Faessler, “Additional Nucleon Current Contributions to Neutrinoless Double Beta Decay,” *Phys. Rev.*, vol. C60, p. 055502, 1999, hep-ph/9905509. [57](#)
- [81] J. Engel, P. Vogel, X.-D. Ji, and S. Pittel, “Double beta decay in the generalized seniority scheme,” *Phys. Lett.*, vol. B225, pp. 5–9, 1989. [57](#)
- [82] M. Moe and P. Vogel, “Double beta decay,” *Ann. Rev. Nucl. Part. Sci.*, vol. 44, pp. 247–283, 1994. [57](#)
- [83] J. Suhonen, O. Civitarese, and A. Faessler, “Description of the  $0^+ \rightarrow 0^+$  neutrinoless double beta decay transition in Ge-76: Particle number projected quasiparticle random phase approximation,” *Nucl. Phys.*, vol. A543, pp. 645–660, 1992. [57](#)
- [84] M. Aunola and J. Suhonen, “Mean-field effects on neutrinoless double beta decay,” *Nucl. Phys.*, vol. A643, pp. 207–221, 1998. [57](#)
- [85] O. Civitarese and J. Suhonen, “Extracting information on the  $0\nu\beta\beta$  decays from the  $2\nu\beta\beta$  decays,” *Nucl. Phys.*, vol. A761, pp. 313–332, 2005. [57](#), [58](#), [59](#)
- [86] K. Muto, E. Bender, and H. V. Klapdor, “Nuclear structure effects on the neutrinoless double beta decay,” *Z. Phys.*, vol. A334, pp. 187–194, 1989. [57](#)
- [87] J. Suhonen and O. Civitarese, “Weak-interaction and nuclear-structure aspects of nuclear double beta decay,” *Phys. Rept.*, vol. 300, pp. 123–214, 1998. [61](#)
- [88] M. Aunola and J. Suhonen, “Systematic study of beta and double beta decay to excited final states,” *Nucl. Phys.*, vol. A602, pp. 133–166, 1996. [61](#), [62](#), [63](#)
- [89] E. Fiorini *Proc. Int. Conf. NEUTRINO 77*, vol. 2, pp. 315–320, 1978. [61](#)
- [90] E. Bellotti *et al.*, “An experimental investigation on lepton number conservation in double beta processes,” *Lett. Nuovo Cim.*, vol. 33, pp. 273–283, 1982. [62](#)
- [91] A. S. Barabash *et al.*, “Two neutrino double beta decay of Mo-100 to the first excited  $0^+$  state in Ru-100,” *Phys. Lett.*, vol. B345, pp. 408–413, 1995. [62](#)
- [92] A. A. Raduta and C. M. Raduta, “Double beta decay to the first  $2^+$  state within a boson expansion formalism with a projected spherical single particle basis,” *Phys. Lett.*, vol. B647, pp. 265–270, 2007, nucl-th/0612031. [62](#)
- [93] J. Toivanen and J. Suhonen, “Study of several double-beta-decaying nuclei using the renormalized proton neutron quasiparticle random-phase approximation,” *Phys. Rev.*, vol. C55, pp. 2314–2323, 1997. [62](#), [63](#)

- [94] A. Bakalyarov *et al.*, “Improved limits on beta- and beta- beta- decays of Ca-48,” *JETP Lett.*, vol. 76, pp. 545–547, 2002. [62](#), [63](#)
- [95] A. S. Barabash, V. I. Umatov, A. V. Derbin, and L. A. Popeko, “Search for beta-beta decay of Ge-76 to the excited states in Se-76,” *Z. Phys.*, vol. A352, pp. 231–233, 1995. [62](#)
- [96] J. Suhonen *et al.*, “Renormalized proton-neutron QRPA and double beta decay of  $^{82}\text{Se}$  to excited states in  $^{82}\text{Kr}$ ,” *Z. Phys.*, vol. A358, pp. 297–301, 1997. [62](#), [63](#)
- [97] A. S. Barabash *et al.*, “Investigation of the Beta Beta decay of Zr-96 to excited states in Mo-96,” *J. Phys.*, vol. G22, pp. 487–496, 1996. [62](#), [63](#)
- [98] A. Piepke *et al.*, “Investigation of the beta beta decay of Cd-116 into excited states of Sn-116,” *Nucl. Phys.*, vol. A577, pp. 493–510, 1994. [62](#), [63](#)
- [99] E. Bellotti *et al.*, “A search for double beta decay of Te-128 and Te-130 leading to the first excited state of daughter nuclei,” *Europhys. Lett.*, vol. 3, pp. 889–893, 1987. [62](#)
- [100] C. Arpesella, E. Bellotti, N. Ferrari, and L. Zanotti, “Looking for double beta decay of Nd-150 to excited states of Sm-150 by gamma ray spectroscopy,” *Nucl. Phys. Proc. Suppl.*, vol. 70, pp. 249–251, 1999. [62](#), [63](#)
- [101] S. Stoica and I. Mihut, “Nuclear structure calculations of two-neutrino double-beta decay transitions to excited final states,” *Nucl. Phys.*, vol. A602, pp. 197–210, 1996. [63](#)
- [102] A. A. Klimenko, S. B. Osetrov, A. A. Smolnikov, and S. I. Vasilev, “Double-beta decay of Nd-150 and Ge-76 to excited states,” *Czech. J. Phys.*, vol. 52, pp. 589–596, 2002. [63](#)
- [103] L. De Braekeleer, M. Hornish, A. Barabash, and V. Umatov, “Measurement of the  $\beta\beta$ -decay rate of  $^{100}\text{mo}$  to the first excited  $0^+$  state of  $^{100}\text{ru}$ ,” *Phys. Rev. Lett.*, vol. 86, pp. 3510–3513, Apr 2001. [63](#)
- [104] M. J. Hornish, L. De Braekeleer, A. S. Barabash, and V. I. Umatov, “Double beta decay of Mo-100 to excited final states,” *Phys. Rev.*, vol. C74, p. 044314, 2006, nucl-ex/0512030. [63](#)
- [105] A. S. Barabash, V. I. Umatov, F. Hubert, and P. Hubert, “New limits on the beta beta decay of Te-130 to excited states of Xe-130,” *Eur. Phys. J.*, vol. A11, pp. 143–145, 2001. [63](#)

- [106] A. S. Barabash, F. Hubert, P. Hubert, and V. I. Umatov, “Double beta decay of Nd-150 to the first  $0+$  excited state of Sm-150,” *JETP Lett.*, vol. 79, pp. 10–12, 2004. [63](#)
- [107] T. Tomoda, “ $0+ \rightarrow 2+ 0\nu$  beta beta decay triggered directly by the Majorana neutrino mass,” *Phys. Lett.*, vol. B474, pp. 245–250, 2000, hep-ph/9909330. [63](#)
- [108] B. Maier, “Status of the Heidelberg-Moscow  $\beta\beta$  experiment with  $^{76}\text{Ge}$ ,” *Nucl. Phys. Proc. Suppl.*, vol. B35, pp. 358–362, 1994. [63](#)
- [109] R. Arnold *et al.*, “Double beta decay of Se-82,” *Nucl. Phys.*, vol. A636, pp. 209–223, 1998. [63](#)
- [110] R. Arnold *et al.*, “Measurement of double beta decay of Mo-100 to excited states in the NEMO 3 experiment,” *Nucl. Phys.*, vol. A781, pp. 209–226, 2007, hep-ex/0609058. [63](#)
- [111] L. Zanotti *et al.*, “The Milano experiment on double beta decay of Xe-136,” *J. Phys.*, vol. G17, pp. S231–S241, 1991. [63](#)
- [112] J. Suhonen, “Sub-eV neutrino masses from  $0$  neutrino beta beta decay to an excited  $0+$  state,” *Phys. Rev.*, vol. C62, p. 042501, 2000. [63](#)
- [113] J. Suhonen, “Neutrinoless double beta decay to excited collective  $0+$  states,” *Phys. Lett.*, vol. B477, pp. 99–106, 2000. [63](#)
- [114] J. Suhonen, “Opening of the  $Z = 40$  subshell gap and the double-beta decay of Mo-100,” *Nucl. Phys.*, vol. A700, pp. 649–665, 2002. [63](#)
- [115] J. Suhonen and M. Aunola, “Systematic study of neutrinoless double beta decay to excited  $0+$  states,” *Nucl. Phys.*, vol. A723, pp. 271–288, 2003. [63](#)
- [116] F. Simkovic, M. Nowak, W. A. Kaminski, A. A. Raduta, and A. Faessler, “Neutrinoless double beta decay of Ge-76, Se-82, Mo-100 and Xe-136 to excited  $0+$  states,” *Phys. Rev.*, vol. C64, p. 035501, 2001, nucl-th/0107016. [63](#)
- [117] A. Morales *et al.*, “Results of a search on the neutrinoless double beta decay of ge-76 to the excited states of se-76,” *Nuovo Cim.*, vol. A100, p. 525, 1988. [63](#)
- [118] G. F. Knoll, *Radiation Detection and Measurement*. Wiley, 3rd ed., January 2000. ISBN: 0-471-07338-5. [68](#)
- [119] E. E. Haller, “Isotopically engineered semiconductors,” *Journal of Applied Physics*, vol. 77, no. 7, pp. 2857–2878, 1995. [86](#)
- [120] M. Pedretti *et al.*, “An active-shield method for the reduction of surface contamination in CUORE,” *AIP Conf. Proc.*, vol. 897, pp. 59–64, 2007. [97](#)

- [121] E. Guardincerri, *Sviluppo del sistema di acquisizione per CUORE e analisi di eventi a bassa energia in Cuoricino*. PhD thesis, Università degli Studi di Genova, 2006. [101](#)